Noninvasive neuroimaging of responses to transcranial magnetic stimulation

A Dissertation
SUBMITTED TO THE FACULTY OF THE
UNIVERSITY OF MINNESOTA
BY

Christopher C. Cline

IN PARTIAL FULFILLMENT OF THE REQUIREMENTS
FOR THE DEGREE OF
DOCTOR OF PHILOSOPHY

Advisor: Bin He, PhD

May 2018

Acknowledgements

I would like to express sincere gratitude to my advisor, Dr. Bin He, for his mentorship and guidance. He has been tremendously supportive throughout my time at the University of Minnesota, giving me the flexibility to pursue research projects of the greatest interest to me, providing opportunities to branch out and gain experience with a diverse range of techniques, and offering invaluable career advice. I would also like to thank the members of my dissertation committee, Dr. Stephen Engel, Dr. Matthew Johnson, Dr. Wei Chen, and Dr. Alexander Opitz, for their time, support, and valuable comments.

I am extremely appreciative of my colleagues in the Biomedical Functional Imaging and Neuroengineering Laboratory. Although I cannot name everyone who was involved in some way or another, special thanks go to Dr. Nessa Johnson for building up the TMS methods and regulatory components that were critical for my work, and for her guidance when I was getting started in the lab. Thanks also to Dr. Bradley Edelman, Dr. Abhrajeet Roy, Dr. Abbas Sohrabpour, Dr. Bryan Baxter, Dr. Jianjun Meng, Christopher Coogan, Daniel Suma, James Stieger, Kai Yu, and all other lab members for their advice, emotional support, and friendship. Thanks also to the undergraduate researchers I worked with during the last few years, especially to Virginia Pohl for her time spent delving into my analysis code, and help with running experiments even during early mornings, evenings, and weekends.

I would also like to thank my friends and family, especially my parents, for their support.

I cannot adequately express my gratitude to my wife, Sara, for joining me on this journey. For giving me the flexibility to pursue this work, for the emotional support, for the different perspective on issues, for putting up with odd hours, and even for being willing to move across the country. I would not have made it here without her.

Dedication

To Sara.

Abstract

Transcranial magnetic stimulation (TMS) and electroencephalography (EEG) provide means to noninvasively measure and modulate activity in the brain. EEG has the potential to infer user intent from measured signals, making it possible to build brain-computer interfaces for augmentative and alternative communication and control of devices that do not rely on intact motor function. TMS offers the ability to transiently perturb neural activity with good temporal and spatial precision, and to modulate longer-term excitability and network function, with various applications in both neuroscientific research and clinical treatment.

However, both EEG and TMS have limitations, due in a large part to their noninvasiveness. EEG-based BCIs face issues with inconsistent inference of intent estimated from low-SNR measurements, which degrades the speed and accuracy of BCI control. Likewise, current TMS approaches face issues with variability in responses to stimulation, based on lack of precise targeting information and knowledge of underlying mechanisms of stimulation effects, resulting in inefficient or inconsistently effective clinical neuromodulation interventions.

In this work, I describe several efforts to address these issues using approaches combining TMS and EEG. To improve our understanding of factors influencing successful motor imagery based BCI control, I applied TMS targeted at perturbing specific neural circuits and measuring resulting changes in BCI control. Conversely, I also explored factors influencing responses to TMS and how EEG can be used to inform stimulation via measurements of stimulation response and estimation of pre-stimulation brain state.

Contents

List of Tables

List of Figures

List of Abbreviations

BCI	Brain-computer interface
CSF	Cerebrospinal fluid
EEG	Electroencephalography
EMG	Electromyography
ERD/ERS	Event-related de/synchronization
ERP	Event-related potential
FDI	First dorsal interosseous
GM	Gray matter
ICA	Independent component analysis
M1	Primary motor cortex
ME	Motor execution
MEP	Motor evoked potential
MI	Motor imagery
MRI	Magnetic resonance imaging
PMd	Dorsal premotor cortex
RMT	Resting motor threshold
rTMS	Repetitive transcranial magnetic stimulation
SMG	Supramarginal gyrus
SVM	Support vector machine
TEP	TMS-evoked potential
TMS	Transcranial magnetic stimulation
WM	White matter

1 Introduction

1.1 Transcranial magnetic stimulation

Parts of this section were adapted from my contributions to: Mo Chen, Christopher C. Cline,…, and Bin He. "Advances and challenges in TMS research on motor systems." In Engineering in Medicine: Advances and Opportunities*, edited by Paul A. Iaizzo. Elsevier. In press.*

Transcranial magnetic stimulation (TMS) is a method of noninvasive neuromodulation which uses large transient magnetic fields to induce electric fields in the brain. These induced fields can be of sufficient magnitude to induce neuronal depolarization and directly result in firing of action potentials. When applied in an extended train of pulses, TMS can also have lasting modulatory effects on plasticity in the brain. TMS has potential to be used in a broad range of applications, from brain mapping for neuroscientific purposes to clinical therapies for depression, stroke, and other neurological and psychiatric disorders.

Aside from early experimentation with alternating currents in the late 1800s and early 1900s, the first demonstration of TMS was described by Barker et al. in 1985 (Barker et al., 1985). This initial work used a custom pulse generator and a circular coil placed over the scalp of a human subject to noninvasively stimulate the motor cortex, with individual pulses producing measurable evoked muscle responses in the contralateral hand. Later work improved on this method with additional technical innovations, such as the use of figure-8 coils for improved stimulation focality (Ueno et al., 1988), stimulator circuitry allowing for rapid trains of repetitive pulses (Pascual-Leone et al., 1991), and neuronavigation techniques to coregister TMS coil position with MRI data (Herwig et al., 2001). The first major clinical applications of TMS, as a treatment for depression, was demonstrated in early reports in the late 1990s (George et al., 1995; Pascual-Leone et al., 1996) and in later large scale clinical trials (George et al., 2010;

O'Reardon et al., 2007); this procedure obtained FDA approval in 2008. The establishment of consensus safety guidelines for the application of TMS has also been critical in facilitating responsible development of the field (Rossi et al., 2009; Wassermann, 1998). These and various other methodological innovations have contributed to steady growth in the TMS field in the years since 1985. To understand the various methods and applications of TMS, it is helpful to first review the relevant physics (specifically, electromagnetism), that are fundamental to TMS.

Ampere's circuital law states that the net electrical current through a surface S induces a magnetic field around a contour C enclosing S according to Equation (1).

$$\oint_C \boldsymbol{B} \cdot dl = \int_S \mu_0 \boldsymbol{J} \cdot ds \tag{1}$$

Faraday's law states that a time-varying magnetic field $\boldsymbol{B}$ induces an electric field $\boldsymbol{E}$ according to Equation (2)

$$\oint_C \boldsymbol{E} \cdot d\boldsymbol{l} = -\frac{d}{dt}\int_S \boldsymbol{B} \cdot d\boldsymbol{s} \tag{2}$$

Where S is a surface enclosed by the contour C (Inan and Inan, 1998). To fully describe the electromagnetics underlying TMS, the complete set of Maxwell's equations are needed, of which Equations (1) and (2) are just a subset; we will not discuss these details further here.

Essentially, these equations dictate that driving a time-varying current through a coil will induce a time-varying magnetic field; this time-varying magnetic field will induce an electric field that when imposed on a conductive material (such as brain tissue) will result in an induced current in the material.

Several phenomena related to these equations are particularly relevant for TMS, constraining both the temporal and spatial characteristics of stimulation. Since the induction of electric fields in the brain by TMS require the magnetic field to be time-varying, the current in the brain must itself also be time-varying. Due to energy and thermal constraints, TMS is typically applied in transient pulses each on the order of 100-500 μs in duration.

While purely electrical neuromodulation methods such as transcranial current stimulation (TCS) are limited by the relatively high resistance of the skull, the magnetic field employed by TMS can pass through the skull with negligible attenuation and induce currents in the cortex. TMS is still limited in penetration depth by the stimulation coil's ability to shape the magnetic field it induces; in a simplified homogeneous spherical head model, the induced electric field cannot be higher at any point inside the volume than on the outer surface (Heller and van Hulsteyn, 1992).

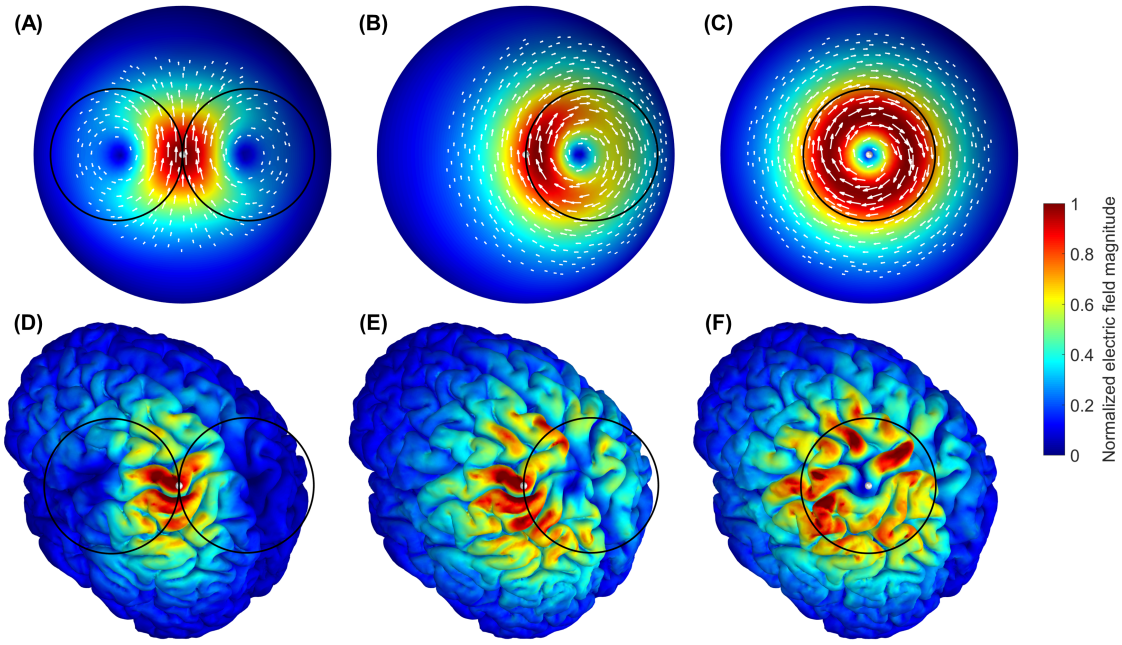

Figure 1.1: Examples of TMS-induced electric fields. *Simulated electric fields induced in a simple spherical head model (A,B,C) and a more realistic head model with detailed cortical surface (D,E,F) by figure-8 (A,D) and circular (B,C,E,F) TMS coils. White arrows in (A,B,C) indicate direction and magnitude of induced current flow.*

This means that efforts to stimulate deeper brain regions noninvasively require even stronger stimulation of more superficial regions. For the most part, this has resulted in primary TMS targets being limited to those located on superficial regions of the cortex, rather than deeper brain structures. While various novel coil geometries have been proposed to optimize the spatial profile of stimulation, these tend to follow a common depth-focality tradeoff (Deng et al., 2013). Due in part to this tradeoff between stimulation depth and focality, the relatively simple figure-8 coil geometry proposed early in the development of TMS (Ueno et al., 1988) has persisted as the most commonly used coil type in modern TMS setups.

Figure 1.1 shows the electric fields induced by simple circular and figure-8 coils in several contexts, as predicted by computational models. It can be seen that a circular coil induces maximum currents in a circle underneath the coil—not at the center of the coil. However, by combining two circular coils with counter-rotating currents, a figure-8 coil obtains maximal induced current underneath the center of the figure-8. Combined with the drop-off in field intensity due to curvature of the head, this geometry obtains relatively focal stimulation extent compared to other coil geometries. As can be seen in Figure 1.1D-F however, this situation becomes more complicated in the presence of the actual gyral geometry of the brain. Here, the varying conductivities and permittivities of the different tissues (especially skull, cerebrospinal fluid, gray matter, and white matter) result in more complex variation in induced electric fields.

In common practice, TMS is applied in a wide variety of experimental and clinical paradigms. Arguably the most common is the stimulation of the primary motor cortex to evoke peripheral muscle responses in muscle groups synaptically connected to neurons in the stimulated cortical region. This muscle response, termed the motor-evoked potential (MEP), is used widely for calibrating stimulation intensity and other parameters in individuals receiving TMS. Additionally,

it has been used for quantifying more subtle changes in cortical excitability, by measuring the average MEP amplitudes evoked by a constant suprathreshold intensity before and after a particular intervention (Touge et al., 2001).

The accessibility of MEP measurements allows a TMS user to be certain where (approximately) and how strongly they are stimulating, *if* they are targeting the primary motor cortex. However, the problem of targeting and measuring stimulation outcomes becomes much more difficult when moving to stimulate almost anywhere outside of the primary motor cortex. Without a clear muscle response, it can be difficult to establish that a desired target is being stimulated, and that other nearby regions are not being stimulated excessively. The complexities of applying TMS outside of the primary motor cortex has contributed to a dominant focus on the motor system in TMS literature.

Despite these challenges, many major established and potential clinical applications of TMS involve stimulation in non-motor regions. For example, the FDA-approved procedure using TMS to treat depression targets the dorsolateral prefrontal cortex (DLPFC). As a result, there is a need for improved methods for targeting and measuring responses to stimulation of non-motor regions. Recent work in this area has included extensive computational modeling to predict fields induced by TMS in subject-specific models (Windhoff et al., 2013) and target selection based on previously collected anatomical and functional MRI data (Cocchi and Zalesky, 2018; Dubin et al., 2017; Esterman et al., 2017; Luber et al., 2017; Opitz et al., 2016; Weigand et al., 2017). While a combination of various techniques will likely be necessary to provide maximally effective stimulation paradigms, a large focus of this work is on the combination of TMS and EEG, described in more detail below.

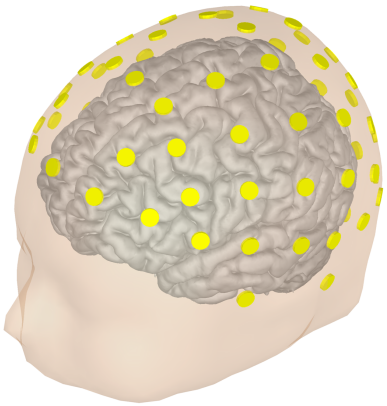

Figure 1.2: Typical 64-channel EEG montage. *Yellow discs indicate individual electrode positions. Montage is shown on a model of an individual's scalp with underlying cortical surface visible.*

1.2 Electroencephalography

Electroencephalography (EEG) is the recording of electrical signals from the brain using noninvasive electrodes on the scalp. First described by Hans Berger in the 1920s (Berger, 1929), EEG has been used in an extremely wide variety of neuroscientific research and clinical applications. EEG measures the gross synchronous activity of large populations of neurons, integrating signals from cortical neurons spread over a surface on the order of 1-10 cm^2 (Buzsáki et al., 2012). The layers of neural tissue, cerebrospinal fluid, skull, and scalp over the underlying sources of activity result in significant mixing of signals through volume conduction before signals can be measured on the scalp. Due to this volume conduction effect and the spatial scale of frequency-specific synchrony in the brain, EEG signal to noise ratios are typically insufficient to resolve neural signals changing faster than approximately 100 Hz. Most EEG signals are thought to be generated by specific classes of cortical neurons oriented perpendicular to the cortical surface; the incoherence in orientations of smaller cortical neurons and distance to deeper brain regions make these other sources of activity practically invisible to direct measurements by EEG. Oscillatory dynamics of EEG are typically described by their peak

frequencies, with different commonly observed frequency bands being the delta (0.2-3 Hz), theta (4-7.5 Hz), alpha/mu (8-13 Hz), beta (14-30 Hz), and gamma (30-90) Hz (Lopes da Silva, 2013).

Despite the limitations imposed by volume conduction, EEG has several key merits compared to other neuroimaging technologies. In particular, a combination of EEG's temporal resolution and relatively economical hardware requirements give it an advantage over existing functional magnetic resonance imaging (fMRI), functional near-infrared spectroscopy (fNIRS), and magnetoencephalography (MEG) approaches for specific applications.

The mixing effects of volume conduction can be mitigated to some degree by estimating a projection of activity from the scalp to the underlying cortical surface. This process, termed source imaging, involves solving a highly underdetermined inverse problem of estimating the activity of thousands or more (depending on the modeled spatial scale) of parcellated cortical sources (represented as current dipoles) from typically just 64-128 electrodes on the scalp (Michel et al., 2004). By incorporating prior information on the anatomical structure of an individual's brain, and the typical orientation of sources measured by EEG, solutions to this inverse problem can be estimated. As part of this inverse estimation process, a computational model of volume conduction is constructed to project activity in the opposite direction (a "forward model"), characterizing the projection from activity of current dipoles on the cortical surface to the resulting electric potentials measured on the scalp.

Source imaging can be particularly critical for multi-subject analysis of EEG data. With considerable variation in cortical anatomy between individuals, active sources in functionally identical regions can be oriented very differently from one subject to the next; these differences

in orientation can drastically alter the projection of the activity measured on the scalp. Figure 1.3 shows an example of this, with simulated results of a synthesized activity topography on an atlas brain, warped to corresponding functional regions in anatomically realistic models of individual subject brains, and projected to the individuals' scalps. This effectively simulates topographies that would be measured by EEG for the underlying "ground truth" activation. We can then use inverse estimation to project these scalp measurements back to the cortical surfaces and warp them back to the atlas brain for averaging. The original ground truth activation is estimated much more accurately in this example when using subject-specific inverse models and averaging in source space.

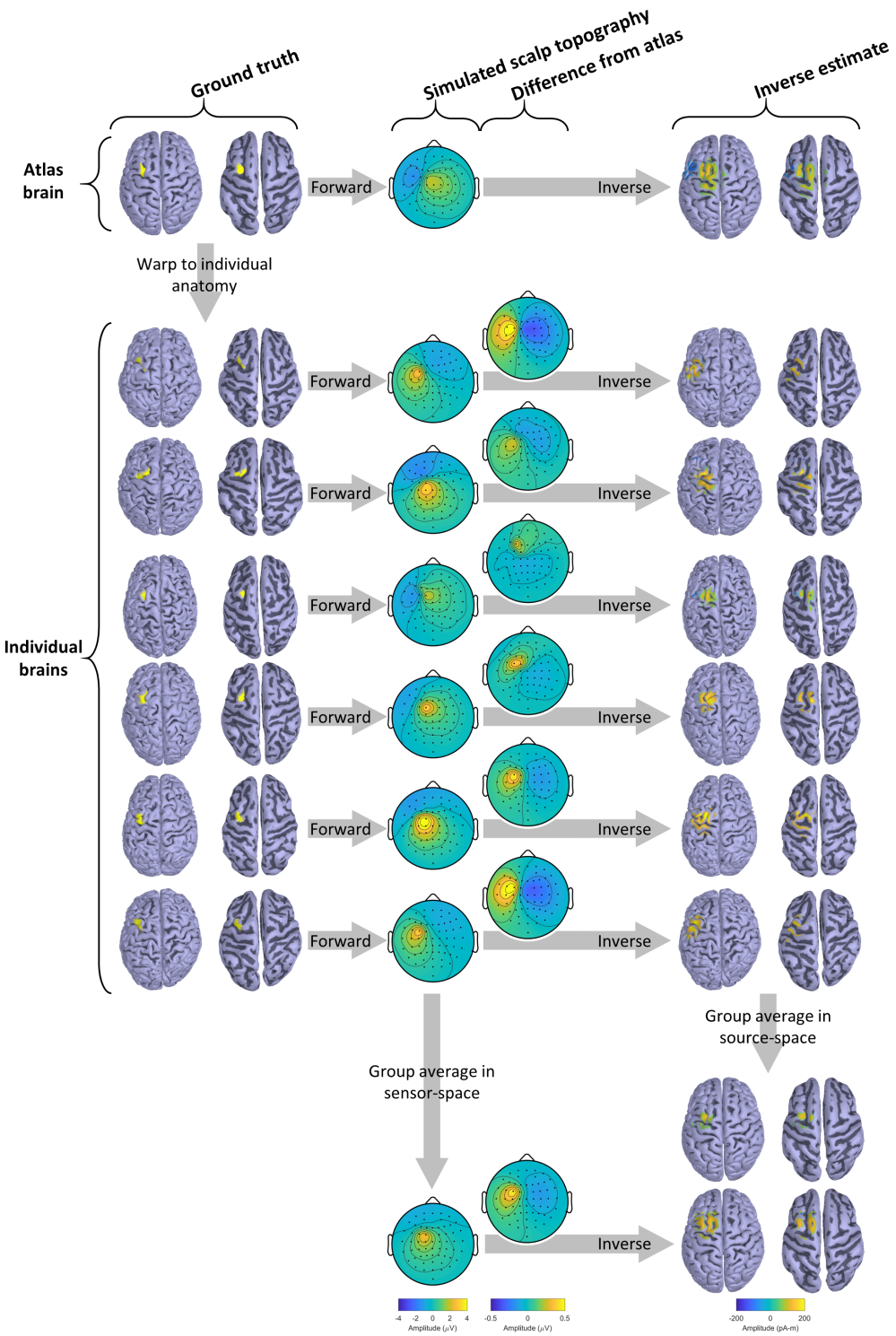

Figure 1.3: Motivation for source imaging. *Simulated activity in an atlas brain is mapped to functionally identical regions in realistic subject brains and projected to each subject's scalp with a forward model of volume conduction to simulate EEG measurements. Then activity is either averaged across subjects in sensor space (lower middle), or first projected back to individual subject brains with inverse models and averaged in source space. The final results show a much better localization of the original ground truth activity when averaging in source space using subject-specific anatomy.*

1.3 Combining TMS and EEG

As discussed above, TMS applied to the primary motor cortex can produce an easily measurable output in the form of MEPs, allowing relatively straightforward titration of stimulation intensities and characterization of stimulation effects. However, comparably simple or immediate output measures are not available when stimulating most other brain regions. Neuroimaging methods that aim to directly or indirectly measure changes in neural activity have the potential to provide valuable information on the effects of TMS. Relevant techniques include EEG, fMRI, fNIRS, and positron emission tomography (PET). These can be utilized in a range of paradigms to reveal immediate changes in activity due to individual TMS pulses, to quantify longer term changes in connectivity due to trains of TMS, to elucidate possible neurophysiological mechanisms of action, and more (Siebner et al., 2009).

EEG, with its high temporal resolution relative to other noninvasive neuroimaging methods, is particularly suited for imaging the fast temporal dynamics of neural activity evoked by TMS. The combination of TMS and EEG will be discussed more extensively in Chapters 3 and 4.

1.4 Brain-computer interfaces and motor imagery

Brain-computer interfaces (BCIs) are systems that provide alternative methods for communication or control not requiring peripheral muscle activation (Collinger et al., 2013; He et al., 2013, 2015; Hochberg et al., 2006; Taylor, 2002; Wolpaw et al., 2002; Yuan and He, 2014). Such systems hold promise to benefit users in a variety of applications; a particularly potentially impactful example is a BCI to provide a communication pathway for individuals in a completely locked-in state, in which loss of peripheral motor control is entirely lost, but brain function remains intact without a conventional means to interact with the outside world (Chaudhary et

al., 2017). In contrast, BCIs can also be used by healthy human individuals for anything from performance monitoring to consumer gaming (Blankertz et al., 2010a). Between these extremes, a range of other applications of BCIs include improving motor rehabilitation after stroke (Ang et al., 2014; Johnson et al., 2017; Ramos-Murguialday et al., 2013; Silvoni and Ramos-Murguialday, 2011; Soekadar et al., 2015), detection of varying levels of responsiveness in disorders of consciousness (Lule et al., 2013; Noirhomme et al., 2017), and neurofeedback-based treatment of ADHD (Lim et al., 2012).

Various BCI modalities exist for extracting information the brain in different ways. Aside from a large body of work on invasive approaches using implanted microelectrodes or electrocorticography arrays (Ajiboye et al., 2017; Hochberg et al., 2006, 2012; Hotson et al., 2016; Jarosiewicz et al., 2015; Vansteensel et al., 2016; Wang et al., 2013), EEG is arguably the most common noninvasive BCI sensing modality. EEG-based BCIs can make use of a range of

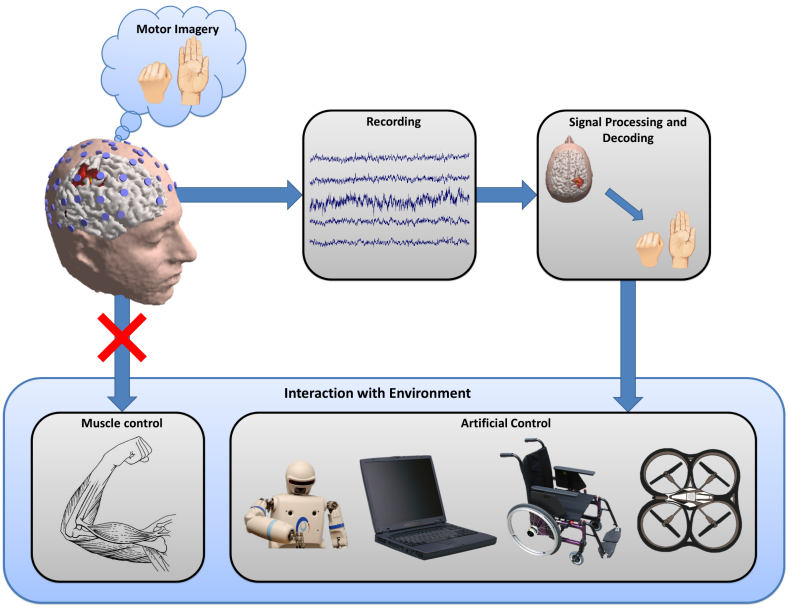

Figure 1.4: Concept diagram of motor-imagery based BCIs. *Reprinted with permission from (He et al., 2015). © 2015, IEEE.*

paradigms, including the P300 oddball response (Donchin et al., 2000; Farwell and Donchin, 1988), steady-state visual-evoked potentials (SSVEPs) (Allison et al., 2010; Gao et al., 2003; Lee et al., 2010; Middendorf et al., 2000; Ono et al., 2013), slow cortical potentials (Birbaumer et al., 2000; Bradberry et al., 2011; Kübler et al., 2001; Xu et al., 2014), and event-related oscillatory changes during motor imagery (Bradberry et al., 2010; He et al., 2015; LaFleur et al., 2013; Pfurtscheller and Neuper, 1997; Wolpaw and McFarland, 2004; Wolpaw et al., 1991; Yuan and He, 2014).

A concept diagram for a typical BCI is shown in Figure 1.4. Generally, components of a BCI system include a volitional change in mental state on the part of the user, measurements of ongoing proxies of neural activity (e.g. EEG), decoding or classification of the user's intent based on the recorded signals, and mapping of a control signal to communicate or manipulate the user's environment.

The focus of this work is on BCIs controlled by intentional modulation of sensorimotor rhythms (SMRs) recorded noninvasively by EEG electrodes near the motor cortex. SMRs consist of intrinsic oscillatory brain activity in the alpha and beta bands in the sensorimotor cortices. SMRs can be modulated by motor intent and by mental simulation of motor activity, also known as motor imagery (MI), resulting in event-related desynchronization (ERD) and synchronization (ERS) of cortical motor regions cortices (Pfurtscheller and Neuper, 1997; Yuan and He, 2014). This is discussed in more detail in Chapter 2.

2 Probing the neurophysiology of motor-imagery-based brain-computer interfaces with transcranial magnetic stimulation

2.1 Introduction

Brain-computer interfaces hold promise for providing communication and control channels for users who have no other means of interacting with the outside world, for improving rehabilitation and treatment of neural disorders, and even enabling new human-machine interfaces for healthy users (Blankertz et al., 2010a; Chaudhary et al., 2017; Lule et al., 2013; Silvoni and Ramos-Murguialday, 2011). One major category of noninvasive BCIs are based on detecting changes in sensorimotor rhythms during imagination of movement (Yuan and He, 2014). These motor imagery based BCIs have been used in a variety of contexts, including control of virtual and physical devices (LaFleur et al., 2013; Meng et al., 2016; Wolpaw and McFarland, 2004), and in rehabilitation after stroke (Buch et al., 2008; Johnson et al., 2017). However, existing BCI approaches are limited by slow bandwidths of information transfer compared to other communication technologies, by potentially long training times, and by inconsistent performance across users (Ahn and Jun, 2015; Blankertz et al., 2010b; Friedrich et al., 2013; Grosse-Wentrup and Schölkopf, 2013; Neuper and Pfurtscheller, 2010).

While a significant research effort has been put towards improving algorithms for classification of neural signals, some recent efforts have begun to examine strategies for improving user performance more directly, including designs for more evidence-based training protocols and task instructions (Lotte et al., 2013a; Neuper et al., 2005), development of more motivating game-like paradigms (Hill et al., 2014; Lécuyer et al., 2008; Leeb et al., 2013; Lotte et al., 2013b), and exploration of correlates and predictors of variations in performance (Allison et al., 2010;

Blankertz et al., 2010b; Halder et al., 2011; Hammer et al., 2012; Kasahara et al., 2015; Vidaurre and Blankertz, 2010).

Understanding the neurophysiological mechanisms of motor imagery is particularly relevant for MI-based BCIs, and for the emerging application of BCIs for motor rehabilitation after stroke. Early behavioral work examining MI provided evidence that the time course of mentally simulated movements approximated the temporal dynamics of actual movement, suggesting common neural frameworks for both real and imagined movement (Decety and Jeannerod, 1995; Decety et al., 1989; Jeannerod, 1995). A large body of neuroimaging literature has explored the role of various motor network components in the brain, including the primary motor cortex (M1), dorsal and ventral premotor cortices (PMd, PMv), supplementary motor area (SMA), supramarginal gyrus (SMG), posterior parietal cortex, anterior cingulate cortex, and the cerebellum (Alkadhi et al., 2005; Gerardin et al., 2000; Guillot et al., 2009; Halder et al., 2011; Hanakawa, 2011; Hétu et al., 2013; Jeannerod and Frak, 1999; Kasess et al., 2008; Lorey et al., 2011; Roth et al., 1996; Sharma and Baron, 2013; Szameitat et al., 2007; Yuan et al., 2010). Meta-analyses of fMRI imaging of MI suggest activation is most consistent in specific premotor, parietal, and deep brain structures; interestingly however, activation of primary motor cortex has not been consistently reported in the fMRI literature (Hétu et al., 2013).

To augment data provided by neuroimaging alone, transcranial magnetic stimulation can provide a method for perturbing specific targeted cortical regions and examining the resulting changes in behavior or imaged activity. Interactions between MI and TMS have been examined in several contexts, with a particular focus on the influence of motor imagery on motor-evoked potentials elicited by suprathreshold TMS targeted at M1 (Abbruzzese et al., 1996; Chong and Stinear, 2017; Facchini et al., 2002; Fadiga et al., 1998; Hashimoto and Rothwell, 1999; Vasilyev

et al., 2017; Williams et al., 2012). These works have in general reported an increase in cortical excitability during motor imagery, specific to the muscle groups relevant to the imagined action. Fewer studies have examined subthreshold stimulation of M1 and stimulation of other motor regions (Cona et al., 2017; Kraeutner et al., 2015; Pelgrims et al., 2009, 2011).

In this work, we applied TMS to several cortical targets proposed to be members of MI-related networks in healthy human subjects immediately before or during performance of a MI-based BCI task. We aimed to explore whether certain regions (e.g. M1 vs. PMd) have preferential roles in sustained MI generation, and whether the contributions of these regions to final BCI performance vary between low- and high-performing users.

2.2 Methods

2.2.1 Common methods

All experimental protocols were approved by the University of Minnesota Institutional Review Board, and subjects gave written informed consent prior to participating in the studies.

2.2.1.1 MRI

T1-weighted anatomical MRI data was collected for all subjects, to use for both TMS neuronavigation and construction of head models for EEG source imaging (described later). Scans were acquired at the Center for Magnetic Resonance Research (CMRR), using a Siemens 3 T Prisma scanner, with 1 mm isotropic resolution (MP-RAGE, 256 mm FOV, 2530 ms TR, 1100 ms TI, 3.65 ms TE, 7° FA) using a 12-channel head coil.

2.2.1.2 EEG/EMG

EEG was recorded with a 64-channel TMS-compatible amplifier (BrainAmp MR, Brain Products), sampled at 5 kHz with a 0.1-1000 Hz bandpass filter. TMS-compatible passive sintered Ag/AgCl

ring electrodes were mounted in a cap (EasyCap) with a standard 10-10 montage, with a reference at electrode position FCz and ground at AFz. EMG was recorded using bipolar amplifier channels connected to the EEG system (BrainAmp EXG), sampled at the same rate. Pairs of EMG electrodes were placed in a belly tendon montage on the first dorsal interosseous (FDI) muscles of the left and right hands, with a ground on the right wrist.

2.2.1.3 TMS

TMS was applied using an air-cooled 70-mm diameter figure-8 coil with biphasic pulses generated by a Magstim Rapid^2. A thin foam pad was placed between the coil and the subject's head to minimize the tactile and auditory bone conducted stimuli produced by the vibration of the coil during stimulation, and subjects wore earplugs throughout experiments to provide hearing protection and attenuate the auditory coil click (Braack et al., 2013).

Coil orientation relative to the subject's head was monitored throughout experiments using a neuronavigation system (Brainsight, Rogue Research). This system uses a stereo infrared camera (Polaris Vicra, NDI) and infrared fiducials attached to the coil and the subject's head (via safety glasses or an elastic strap) to estimate 6 degree-of-freedom (DOF) poses. During each session, this pose information was co-registered to an individual subject's MRI data, based on measurements of anatomical fiducials (left and right preauricular points, nasion, and nose tip). The neuronavigation system was also used to digitize EEG electrode positions at the end of each session.

Stimulation targets were selected based on a combination of functional and anatomical features. The left M1 target was based on the hotspot location derived from MEP measurements (described below), generally over the "hand knob" region of the precentral

gyrus. The posterior PMd target (PMd_p) was selected as a point at the intersection of the superior frontal sulcus and the superior precentral sulcus, while the anterior PMd target (PMd_a) was selected as a point on the middle frontal gyrus sulcus approximately 0.5 cm anterior from this (Amiez et al., 2006; Hardwick et al., 2013; Lu et al., 2012; Parmigiani et al., 2015; Picard and Strick, 2001; Tomassini et al., 2007). The PMd_a target here is similar to previous TMS studies that targeted PMd based on external scalp features (Gerschlager et al., 2001; Mochizuki et al., 2004; Münchau et al., 2002; O'Shea et al., 2007; Rizzo et al., 2004; Suppa et al., 2008; Uithol et al., 2015), except that exact positions in this study were adjusted in individual subjects based on cortical anatomy. The SMG target was selected as a point on the anterior region of the supramarginal gyrus (Hartwigsen et al., 2012; Rushworth et al., 2001).

Coil orientations at these targets were primarily selected so that (1) the center of the figure-8 was located over the target at the closest point between the cortical surface and the scalp (2) the face of the coil was tangential to the head, and (3) the coil handle (i.e. the short axis of the

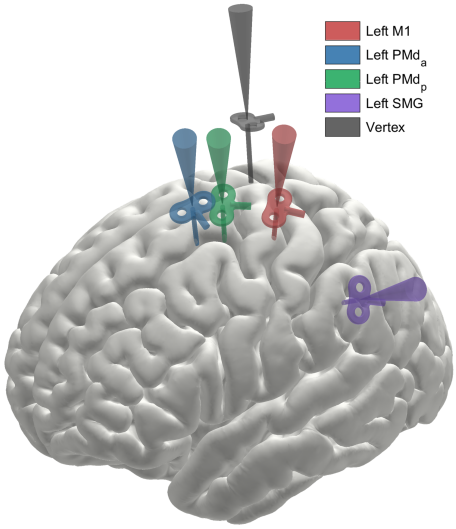

Figure 2.1: Coil orientations for TMS targets. *Aggregated from actual coil orientations in individual subjects after transforming to MNI space, overlaid on an ICBM152 average cortical surface. The coils shown here are for visualization of orientation only—they are not to scale.*

coil) was located perpendicular to the targeted gyrus. This orientation matches the convention for stimulating the hand region of M1 with the coil held at a 45° angle relative to the midline, which typically results in an induced field perpendicular to the precentral gyrus at that location. This is also supported by computational models that generally predict maximal induced fields when the short axis of the figure-8 coil is oriented perpendicular to the underlying gyrus (Janssen et al., 2015; Thielscher et al., 2011).

Average cortical targets and coil orientations across all sessions in the sequential rTMS experiments are shown in Figure 2.1, overlaid on an ICBM152 average surface (Fonov et al., 2009, 2011). Additionally, a vertex target in the concurrent TMS-BCI experiments was selected as the point circumferentially halfway between the nasion and inion on the scalp and centered over the interhemispheric fissure, with the coil handle pointing in the posterior direction.

RMT and motor hotspot location were assessed during each TMS session. RMT was defined as the minimum stimulation intensity necessary to evoke MEPs in the contralateral FDI muscle with peak-to-peak amplitudes exceeding 50 μV in at least five out of ten pulses applied at least 1 s apart; motor hotspot location was defined as the coil orientation resulting in maximal MEP amplitudes for a fixed stimulation intensity near RMT. This was estimated by beginning with the coil centered over the putative hand-knob region of the subject's primary motor cortex and oriented at 45° relative to the midline, and then adjusting stimulation intensity and coil orientation based on ongoing MEPs elicited by intermittent single pulses.

2.2.1.4 BCI paradigms

During the experiment sessions, subjects viewed task cues on a computer screen located approximately 0.5 m away in the center of their field of view. Task cues were presented for 1 s,

followed by a go cue and the task period, followed by an inter-trial interval. Subjects were instructed to perform either movement execution ("move", ME) or motor imagery ("imagine", MI) of rapidly opening and closing their left or right hands. During all ME trials and a subset of MI trials, no feedback was presented. During a majority of MI trials, as described below, feedback was presented (i.e. these were "BCI" trials).

For the BCI paradigm studied here, subjects controlled a bar that moved to the left or right depending on online decoding of their intent. BCI2000 was used for online signal processing and classification (Schalk et al., 2004), combined with a custom user-facing application built in Python with BCPy2000 to handle experiment timing, stimulus cues, and feedback. Online feedback was based on spectral power in the 10-14 Hz band estimated by an autoregressive model over a rolling window of 320 ms of EEG data, specifically focusing on electrodes C3 and C4 located over the left and right sensorimotor cortices, respectively. After additional dynamic normalization and smoothing, the position of the end of the filled bar was proportional to the difference in band power between these channels.

Screen captures of the task cues and BCI feedback are shown in Figure 2.2.

2.2.2 Sequential rTMS-BCI experiments

In study 1, BCI performance was assessed before and after blocks of real or sham rTMS. The order of study procedures for a typical sequential rTMS-BCI session is shown in Figure 2.3. Sessions began with EEG capping and determination of RMT and motor hotspot location.

Each of the three task blocks was divided into three runs; each run began with a 10 s rest period, followed by 36 trials, including 16 BCI trials (i.e. imagine with feedback), 8 MI trials (imagine without feedback), and 8 ME trials, each equally split into left and right trials, and 4 rest trials.

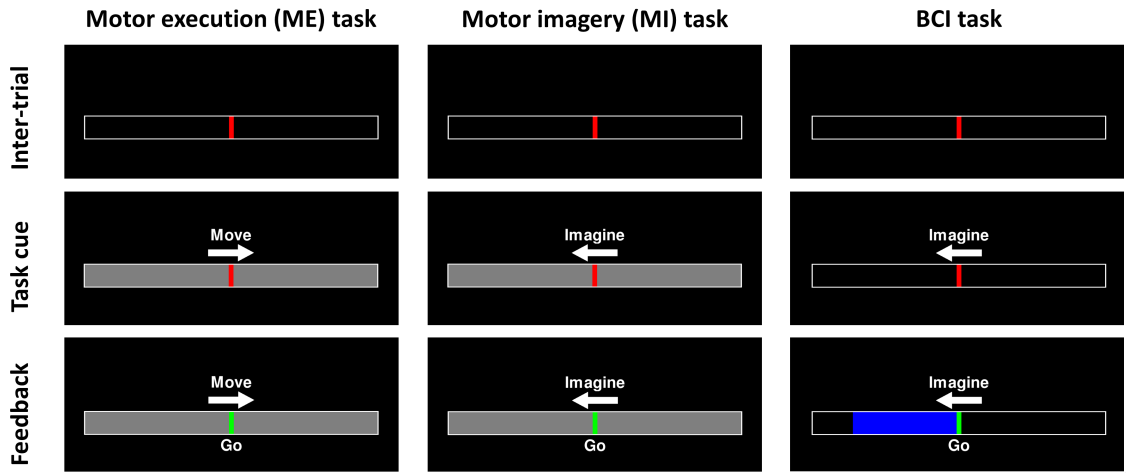

Figure 2.2: Task paradigm cues seen by subjects during sequential rTMS-BCI experiments.

This task frequency was designed to provide more data for the primary task of interest (BCI trials) while still providing data for comparison to other task variants. The inclusion of ME trials also facilitated monitoring of subject task compliance. Task trials were randomly shuffled within each run. Inter-trial intervals had a uniformly jittered duration of 2-3 s, followed by a 1 s task cue, a go cue, and a 4 s task period. Including short pauses between runs, each block lasted approximately 15 min.

The rTMS blocks consisted of 15 min of 1 Hz pulses (i.e. 900 pulses), applied at 90% of the individual subject's RMT. Blocks were split into two 7.5 min segments, with a short (≈30 s) pause in between to check in with the subject and adjust coil position to compensate for any head movement. Real and sham rTMS were applied in separate blocks, with the order of these blocks shuffled across sessions / subjects. A dedicated sham coil was used to provide a control rTMS condition. This sham coil generates a magnetic field with drastically reduced magnitude and focality, while still mimicking the auditory clicking and other sensations of real stimulation. Each session focused on a single rTMS target selected from the left M1, left PMd_a, left PMd_p, and left

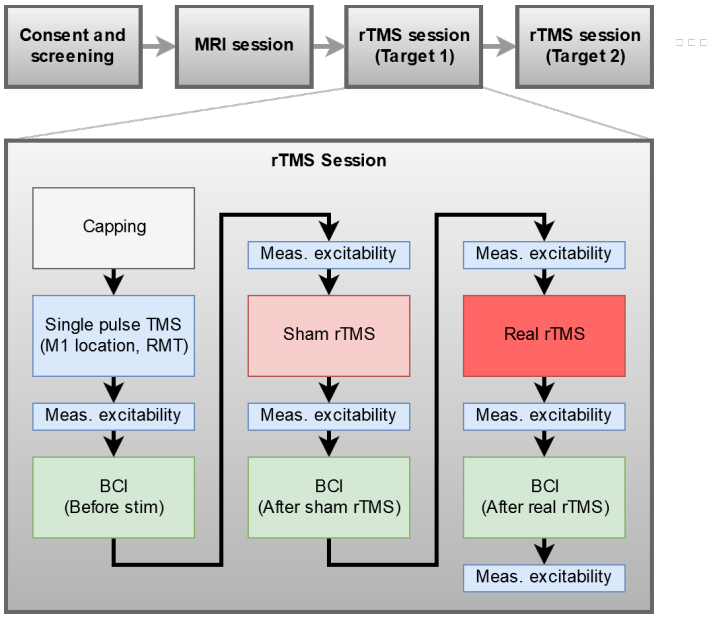

Figure 2.3: Sequence of procedures within an example sequential rTMS-BCI experiment session.

SMG targets shown in Figure 2.1. Subjects returning for multiple rTMS sessions received rTMS to a different target in each session, with the order of these sessions shuffled across subjects. Within each subject, each session was at least seven days apart.

Cortical excitability was assessed before and after each stimulation and task block by applying single intermittent pulses to the subject's motor hotspot (left M1) at 120% RMT and measuring peak-to-peak amplitudes of the resulting MEPs evoked in the contralateral FDI. Within each excitability measurement block, 30 pulses were applied with 2-4 s uniformly jittered inter-pulse intervals.

20 subjects participated in the sequential rTMS-BCI study, with an average of 2.8 rTMS sessions per subject (i.e. 56 total sessions). Ideally, all subjects would have participated in four rTMS sessions to stimulate each target in each subject; however, some subjects did not complete all sessions due to changes in availability or other eligibility (e.g. start of a medication matching

TMS exclusion criteria). All subjects had previous experience with MI-based BCIs from previous studies in the laboratory; this served to minimize the contributions of early learning to variance in BCI performance.

2.2.3 Concurrent TMS-BCI experiments

In study 2, single TMS pulses were applied during individual BCI trials to examine more transient interactions between task performance and stimulation. Sessions began with EEG capping and determination of RMT and motor hotspot location.

During the main part of the experiment, six stimulation variants were applied: stimulation to left M1, left PMd_p, and vertex, each at 90% and 120% of the individual subject's RMT. These stimulation parameters were applied in non-BCI rest blocks, and during BCI blocks with a mix of task trials. In the non-BCI rest blocks, TMS was applied in subblocks of 50 pulses, uniformly jittered 2-4 s apart, while the subject rested with eyes open. At the start of the session was a longer non-BCI rest block containing 6 subblocks in each of which one of the six stimulation variants was applied.

Each BCI block was split into three runs, each employing a different stimulation variant. Each run consisted of 80 total trials, including 48 BCI trials, 24 rest trials, and 8 ME trials; the BCI and ME trials were equally split into left and right trials. Each trial consisted of a uniformly jittered 1-2 s inter-trial interval, a 1 s task cue period, a go cue, and a 2 s task period. During two-thirds of the BCI and rest trials, a single TMS pulse was applied 0.5 s after the go cue. This delay was selected based on previous data (not shown) indicating a peak in alpha ERD/ERS about 0.5 s after the go cue. Compared to the BCI paradigm used in study 1, these trials were shorter, allowing more

data to be collected in the single-trial effects of TMS, at the cost of reduced isolation of oscillatory dynamics between consecutive trials.

The custom BCI interface implemented with BCPy2000 was used for synchronizing the triggering of TMS pulses at specific times relative to task onset. Additionally, the online classification normalizer was set up to disregard data in a timespan of [-100, 500] ms around the TMS pulse, so that the large TMS-induced EEG artifact did not affect online feedback for more than one window length after each pulse.

Subthreshold stimulation was applied in two of the three BCI blocks per session, while suprathreshold stimulation was applied in the third. It was predicted that the effects of subthreshold stimulation (if any) would be weaker, and would therefore justify collecting additional data to improve our ability to detect an effect if present.

Each BCI block was followed by a shorter rest block, in which two more subblocks of 50 pulses at rest were applied. These additional non-BCI rest blocks provided the subject a break from the more cognitively demanding BCI tasks while also providing additional data on TMS-evoked responses at rest.

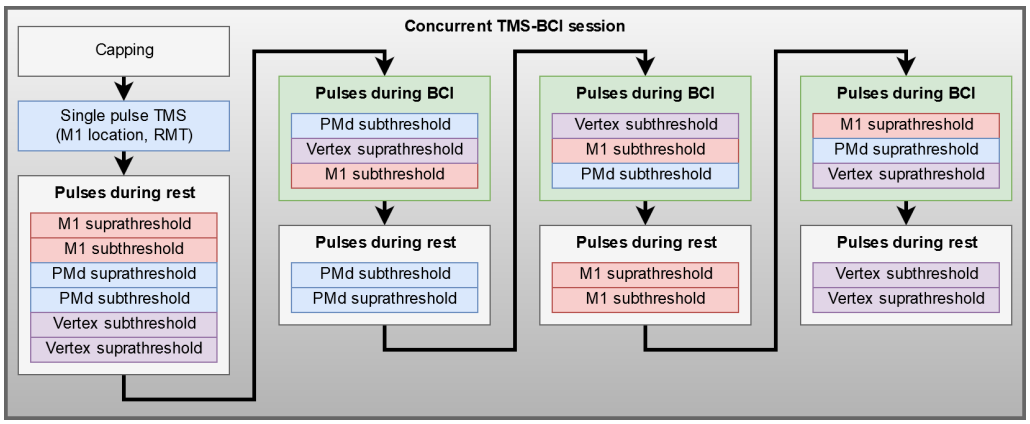

Figure 2.4: Sequence of procedures within an example concurrent TMS-BCI experiment session.

The various task trials with and without TMS were randomly shuffled within each run, the order of stimulation conditions was shuffled within each block, and the order of the blocks was shuffled across sessions. Other than differences in these shuffling orders, procedures in all concurrent TMS-BCI experiment sessions were the same for all subjects. An example sequence of procedures for one session is shown in Figure 2.4.

Eight subjects participated in the concurrent TMS-BCI study, with five of these returning for a second session; the other subjects could not return due to scheduling constraints. The second sessions for these subjects were procedurally identical to the first sessions other than different shuffled orders of blocks and trials; the repeat sessions provided data on reproducibility of effects across multiple days within a given subject.

2.2.4 Analyses

Oscillatory dynamics during the task conditions were assessed as follows. Average power within the alpha band (defined here as 8-12 Hz) was estimated for each trial, during baseline and task periods, for each EEG channel. For estimating BCI performance, task powers for electrodes C3 and C4 were extracted, and a support vector machine (SVM) based classifier was trained on the data pooled within each session, with accuracies obtained from 10-fold cross-validation.

2.3 Results

2.3.1 Sequential rTMS-BCI experiments

An example of data from a single session for a single subject is shown in Figure 2.5. In this subject, alpha power topographies contrasting BCI left vs. right conditions show clear bilateral countermodulation over the sensorimotor cortices, with the signs of power changes matching those predicted by previous work describing motor-intention-related ERD/ERS: imaging

movement of the right hand producing a desynchronization in the contralateral controlling hemisphere (left) and synchronization in the ipsilateral hemisphere (right). Specifically examining electrodes C3 and C4, the boxplots in Figure 2.5B show this left/right countermodulation as well, with some variation across stimulation conditions. Figure 2.5C illustrates the discriminant boundary of the trained SVM classifier with good separation between task classes apparent for this relatively high-performing subject. Finally, it is clear from Figure 2.5D that in this subject, the BCI trials produced more discriminable signals than the ME and MI without feedback trials, although the confidence intervals for these tasks is much larger due to the reduced number of trials.

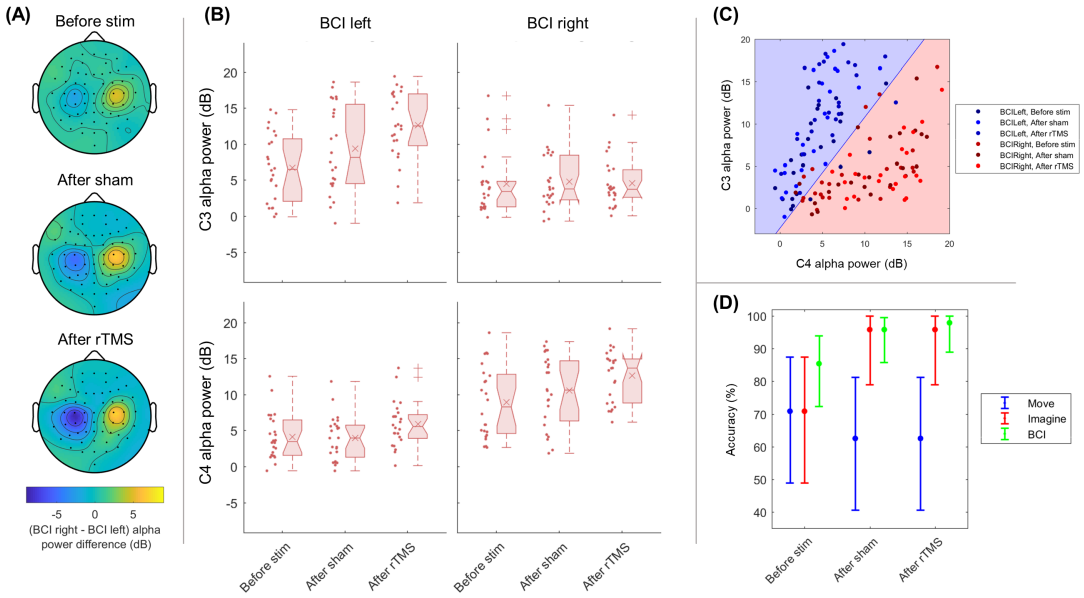

Figure 2.5: Electrophysiology and BCI performance results in a single example rTMS session. *In this session, the subject received rTMS to left M1. (A) shows topographies of alpha power contrast between the left and right BCI task conditions. (B) shows box and scatter plots of average alpha power at electrodes C3 and C4 for individual trials across tasks and stimulation conditions. In each boxplot, the center line indicates the median value, the notches indicate an approximate 95% confidence interval for the median, "+" indicates an outlier, and the "x" indicates the arithmetic mean. Out(C) shows the results of training an SVM classifier on the pooled data, with the blue and red backgrounds indicating discriminant regions for the BCI left and right tasks, respectively. (D) shows overall offline classification accuracy for the 3 pairs of task conditions (move, imagine, and BCI) across stimulation conditions; here, error bars represent 95% binomial confidence intervals.*

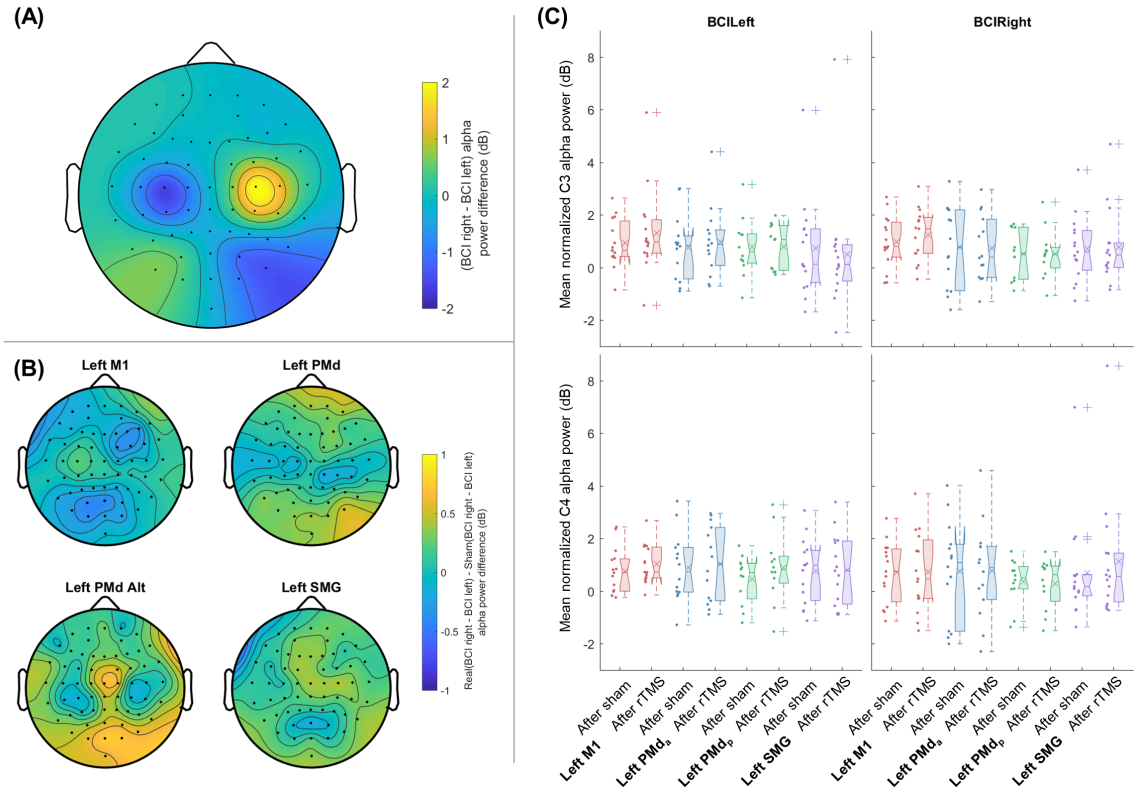

Figure 2.6: Group electrophysiology results across rTMS conditions. *(A) shows the grand average alpha power contrast across all subjects and stimulation conditions. (B) shows the differences in this task contrast between real and sham stimulation to each of the four cortical targets. (C) shows normalized aggregated C3 and C4 alpha powers during the BCI left and BCI right tasks measured after sham vs. after real stimulation.*

Group-level electrophysiology results are shown in Figure 2.6. From the grand average left vs. right alpha power topography difference shown in Figure 2.6A, a clear bilateral countermodulation is apparent, peaking at electrodes C3 and C4. However, as evidenced by the overlapping notches of the boxplots in Figure 2.6C, there were no clearly significant group-level effects on C3 and C4 task-related alpha power by real over sham rTMS for any of the stimulation conditions.

Group-level BCI performance results are shown in Figure 2.7. There were no statistically significant universal effects of stimulation condition on BCI performance across the pooled subjects. However, there was indication of a performance-dependent effect, as indicated in the

scatter plots in Figure 2.7A. Specifically, for rTMS to left M1, the plot of each subjects' individual performance after sham vs. after real rTMS suggests a possible sigmoidal relationship, with high-performing subjects improving after real stimulation, and low-performing subjects degrading in performance. After splitting subjects into high-performing and low-performing groups based on their average performance, this trend is more apparent, as shown in Figure 2.7B and Figure 2.7C. In particular, for rTMS to left M1, there was a marginally significant difference in performance changes between low- and high-performing subjects (two-sample t-test, p=0.089 uncorrected), but not for within-group differences between the after sham and after rTMS conditions (one-sample t-test, p=0.051 and p=0.057 uncorrected for low- and high-performing groups, respectively). Likewise for rTMS to SMG there was a marginally significant increase in performance for real over sham rTMS for the high-performing group (one-sample t-test, p=0.045 uncorrected), but not for the low-performing group or between groups (p>0.1). No significant differences were observed for rTMS to PMd_a and PMd_p. It should be noted that these trends do not survive correction for multiple comparisons and should not therefore be interpreted as conclusive.

2.3.1.1 M1 excitability

Group excitability results are shown in Figure 2.8. MEP amplitudes were log transformed to units of dBmV to reduce skew of distributions (Goetz et al., 2014, 2016; Nielsen, 1996). The median aggregated peak-to-peak MEP amplitude in response to pulses at 120% RMT was 0.105 dBmV (1.01 mV), which matches previous work characterizing stimulation response curves for TMS to M1 (Rossini et al., 2015). To reduce the contribution of inter-subject variations in MEP amplitudes, values were normalized by the MEP amplitude during the "start" condition. As

indicated by the box plots in the bottom row of Figure 2.8, there were no significant differences between consecutive excitability measurements across stimulation conditions.

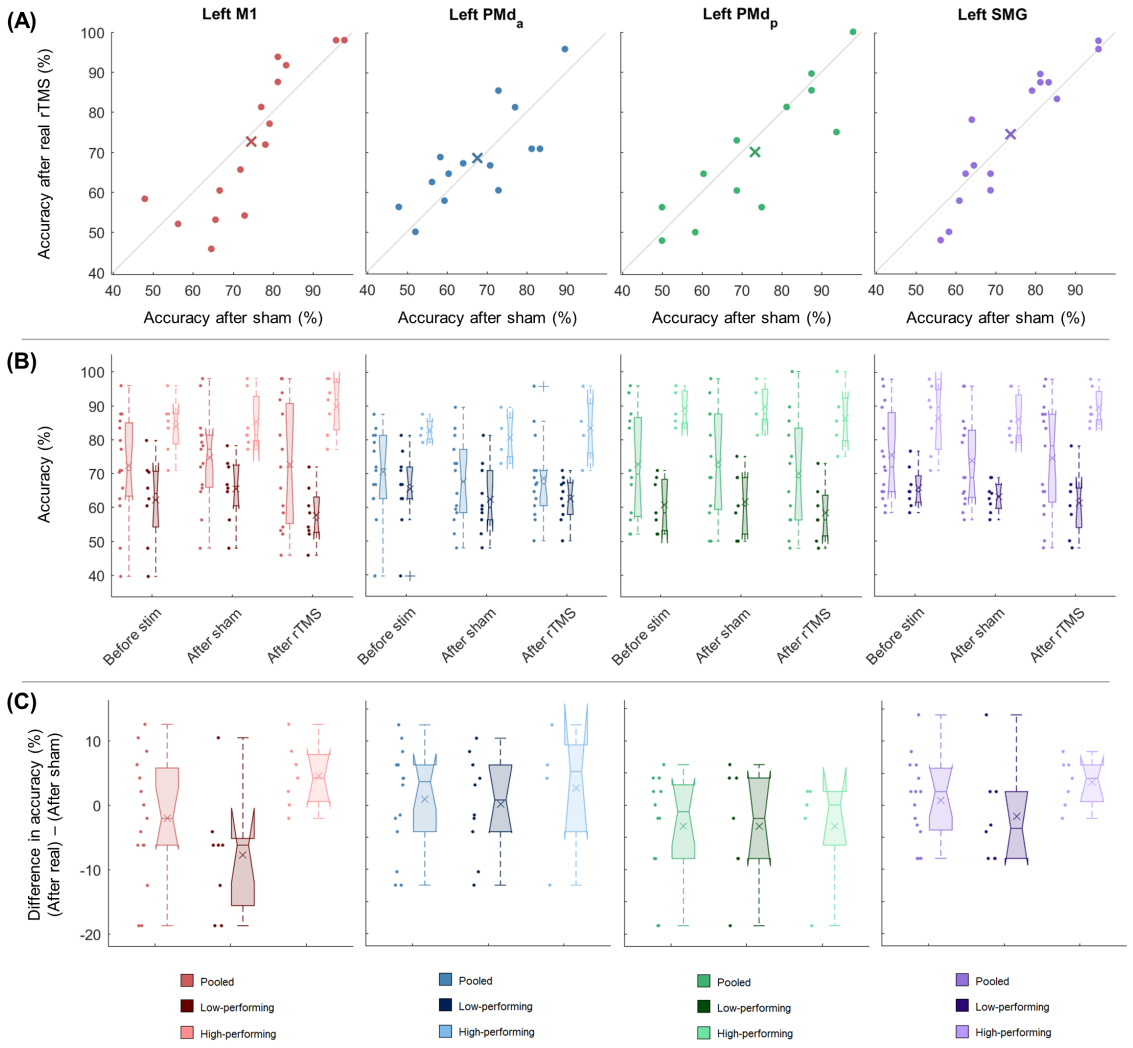

Figure 2.7: BCI performance changes before and after real and sham rTMS. *(A) shows scatterplots of accuracy after sham rTMS vs. after real rTMS, where if there were no measurement variability and no change due to TMS, all points would be expected to lie along the diagonal, indicated by the gray line. The X scatter marker indicates the mean accuracy values within the stimulation condition. (B) shows absolute accuracies as a function of stimulation condition, and illustrates the dividing of subjects into low-performing and high-performing subgroups based on mean performance. (C) shows the per-session difference in performance between BCI conditions.*

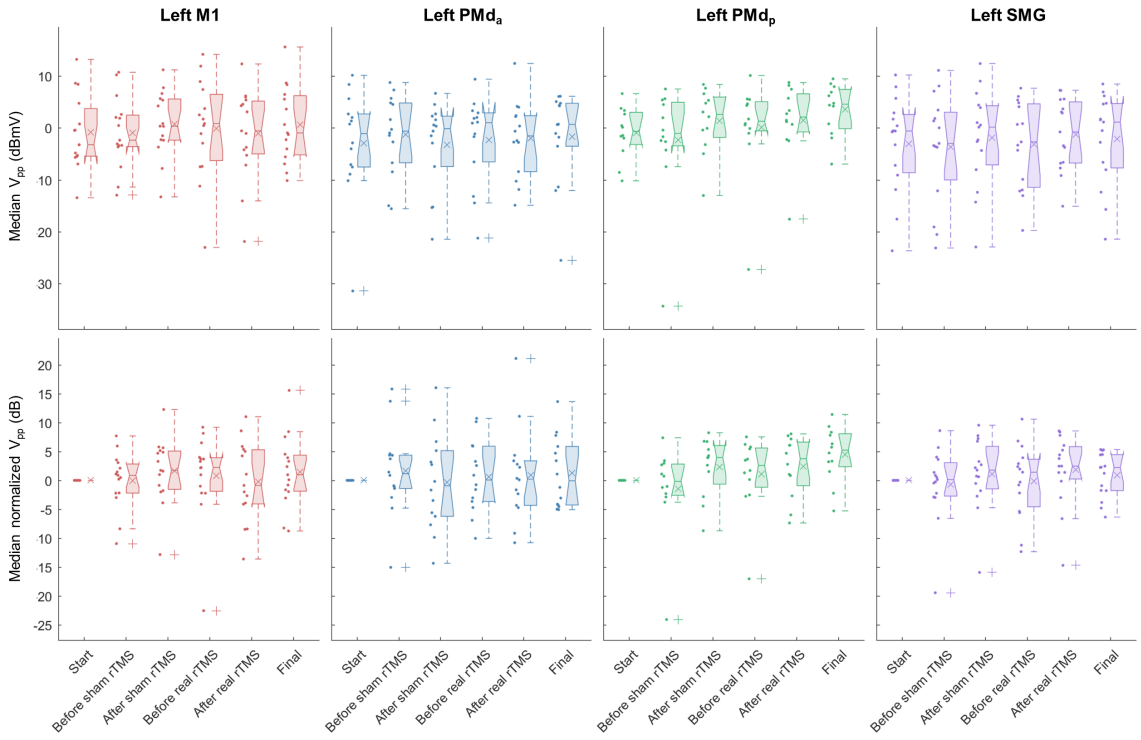

Figure 2.8: Cortical excitability measurements before and after rTMS. *Note that all rTMS sessions applied suprathreshold stimulation to left M1 for the excitability measurements, regardless of rTMS target. The top row shows un-normalized values, while the bottom row shows values normalized within each session to the median MEP amplitude in the first measurement block ("Start"). Individual points represent medians within single conditions within sessions (each aggregated from 30 pulses).*

2.3.2 Concurrent TMS-BCI experiments

Figure 2.9 shows the aggregated BCI performances of subjects receiving intermittent single pulses of TMS during a subset of task trials. No statistically significant differences were observed in TMS vs. no TMS conditions within a run. However, a possible effect is apparent in the suprathreshold M1 stimulation condition, in which BCI classification accuracy decreased in trials with stimulation.

The task-related alpha power for the same BCI blocks is shown in Figure 2.10. Just comparing BCI left to BCI right within conditions, the C3 ERS/ERD left/right contrast used for online BCI

Figure 2.9: BCI performance during concurrent single TMS pulses. *Performance in trials without TMS ("NoTMS") are compared to those with TMS, across stimulation targets and stimulation intensities. Normalized accuracy values here were normalized by the mean accuracy during the NoTMS trials within each session.*

control is apparent. There were no statistically significant differences between TMS and no TMS conditions. However, the possible effect observed for left suprathreshold M1 stimulation on BCI performance was also visible here, with C3 power in BCI left trials dropping to similar levels as in BCI right trials (i.e. degrading the task-dependent contrast used for BCI control) only in BCI left trials in which stimulation was applied.

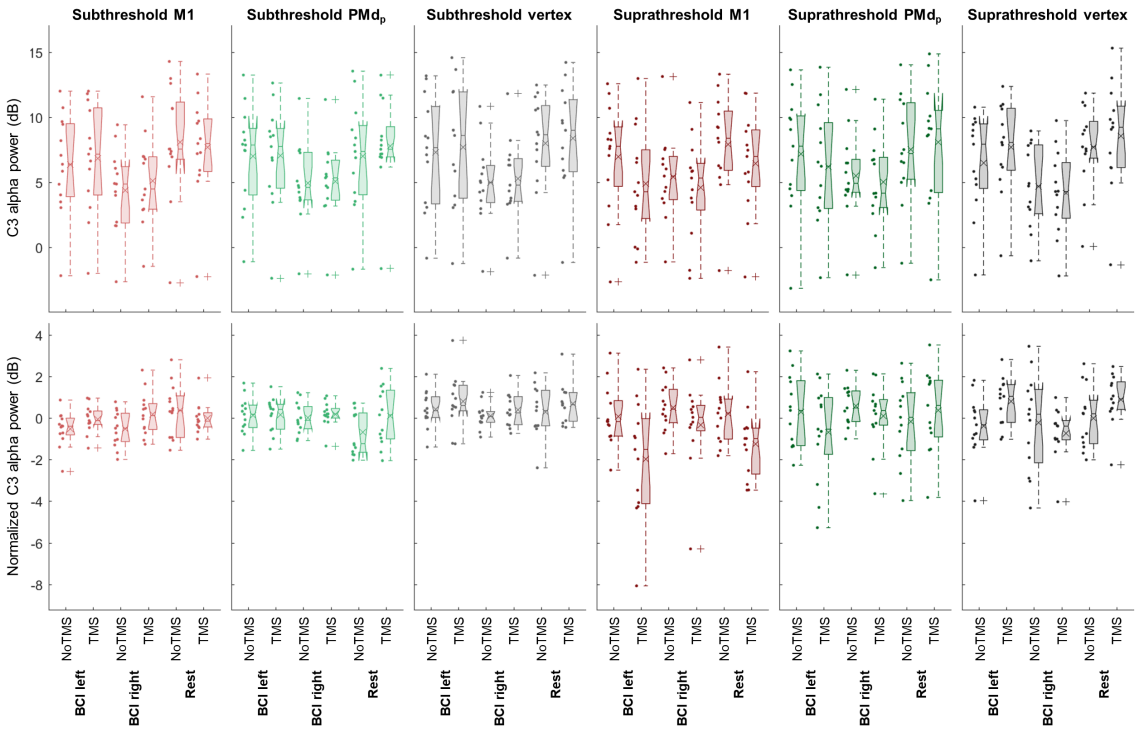

Figure 2.10: Task-related alpha bandpower values during concurrent TMS-BCI blocks. *Alpha bandpower at electrode C3 in trials without TMS ("NoTMS") is compared to those with TMS, across tasks and stimulation conditions. Alpha power was calculated during a window 1-2 s after the start of each trial, corresponding to approximately 500 ms after the TMS pulse in trials with stimulation. Normalized values here were obtained by subtracting the mean alpha power during the NoTMS trials within each session.*

2.4 Discussion

As demonstrated by the aggregated electrophysiology and BCI performance results shown in Figure 2.5 and Figure 2.6, subjects could successfully control the 1-dimensional left/right BCI system, with a range of performance levels. The average topography of alpha desynchronization/synchronization shown in Figure 2.6A matches expectations of contralateral opposite effects centered near electrodes C3 and C4.

The 1 Hz rTMS pulse trains applied here produced much weaker effects than originally hypothesized, with expected changes in cortical excitability not observed (see Figure 2.8). Early work in the TMS field suggested a robust inhibitory effect of 1 Hz rTMS on cortical excitability (Gerschlager et al., 2001; Touge et al., 2001). However, there is considerable variability in responses to stimulation (Gangitano et al., 2002; Goetz et al., 2016; Hinder et al., 2014; Lefaucheur et al., 2014; Maeda et al., 2000; Münchau et al., 2002; Sommer et al., 2002; Suppa et al., 2008), with some differences in stimulation responses possibly attributable to use of different stimulation parameters, including biphasic vs monophasic waveforms and details of coil orientation for targeting. Additionally, the MEP measurements used to characterize excitability have considerable sources of variation themselves, including spinal and peripheral contributions (Burke and Pierrot-Deseilligny, 2010; Cuypers et al., 2014; Goetz et al., 2014; Jung et al., 2010; Ngomo et al., 2012; Sollmann et al., 2013). Variability in responses to TMS is explored in greater detail in Chapters 3 and 4.

The lack of effects of our rTMS intervention on cortical excitability estimated from MEP measurements does not rule out the presence of other effects on cortical dynamics. Indeed, a possible performance-dependent effect of rTMS to M1 on BCI performance was observed (see

Figure 2.7). This performance-dependent trend suggested a decrease in performance after real rTMS for previously low-performing subjects, and an increase in performance for high-performing subjects. This has implications with regards to the mixed reports of M1 activation not being consistently observed during MI in the fMRI literature (Hétu et al., 2013). One possible interpretation of this result is that low-performing subjects rely more completely on M1 for performing MI, and when it is perturbed their relatively low performance is degraded further; in contrast, high performing subjects may rely on other (presumably premotor / supplementary motor / parietal regions) and can actually improve performance when M1 is perturbed by compensating with these other areas. However, this is conjecture based on limited data; further experiments are needed to determine whether this trend holds with additional subjects and to explore more detailed mechanisms of any effect. If the trend does hold, it could have significant implications for designing BCI paradigms, including instructions and training given to users to optimize for imagery strategies that, for example make more use of premotor regions and less on primary motor cortex; this would be analogous to existing established practice of recommending subjects perform kinesthetic instead of visual motor imagery for improved discriminability of MI states (Neuper et al., 2005).

The investigation of single pulses applied during individual BCI trials suggested that the strongest effect (if any) was of suprathreshold stimulation to M1 causing a degradation in single-trial BCI performance (Figure 2.9) and a corresponding drop in C3 alpha power specifically in BCI left trials following stimulation Figure 2.10. However, given that the suprathreshold stimulation of the targeted region of M1 induces MEPs in the contralateral hand, it is possible that this effect on performance could be attributed to indirect effects—either an effect of somatosensory feedback on the volitional control of sensorimotor rhythms in the area, or a higher-level effect

on attention by distraction of the subject from the MI task. A more moderate decrease in synchronous alpha band power was also observed during the rest trials, suggesting that in both BCI left and rest trials the application of TMS resulted in desynchronization of alpha power, bringing the oscillatory power closer to that seen during the already desynchronized state during right MI.

In general, the results of these studies should be considered exploratory, as the experiments were not designed to be sufficiently powered to provide definitive statistical conclusions on effect sizes or to test highly specific a priori defined hypotheses. Further work will be needed to follow up on the trends observed here in more narrowly focused experiments with additional subjects.

3 Neuroimaging of responses to transcranial magnetic stimulation: accounting for inter-subject variation

3.1 Introduction

Transcranial magnetic stimulation is used clinically for the treatment of depression (O'Reardon et al., 2007), and is being actively explored for treatment of various other neurological and psychiatric disorders (for review, see (Lefaucheur et al., 2014)). However, significant inter-individual variability in responses to stimulation is a major issue in the field, resulting in reduced treatment efficacy and issues with developing new treatments for other disorders (Hinder et al., 2014; Lefaucheur et al., 2014; Lepping et al., 2014; López-Alonso et al., 2014; Maeda et al., 2000; Müller-Dahlhaus et al., 2008; Nettekoven et al., 2015; Nicolo et al., 2015; Schilberg et al., 2017; Sommer et al., 2002; Vallence et al., 2015; Vernet et al., 2014).

Given the huge ranges of variation in anatomy, disease etiology, and treatment responses, it seems critical to incorporate as much information as is feasible to tailor stimulation interventions for the individual. Neuroimaging-informed stimulation offers a promising set of approaches for addressing these issues, providing information on where, when, and how to stimulate in an individualized manner. Recent efforts have demonstrated promise for fMRI-informed stimulation, in which functional and anatomic data collected prior to an intervention is used to choose subject-specific targets (Cocchi and Zalesky, 2018; Dubin et al., 2017; Esterman et al., 2017; Luber et al., 2017; Opitz et al., 2016; Weigand et al., 2017). EEG represents a promising imaging modality for online neuroimaging-informed stimulation, due to its noninvasiveness, high temporal resolution, and relatively economical hardware requirements.

The majority of the TMS literature has focused on stimulation of the motor cortex, largely due to the presence of an easily measurable "readout" of stimulation effect—the motor evoked potential (MEP)—that is elicited by suprathreshold stimulation of M1. This has been crucial for calibrating stimulation intensity to individuals and informing optimal coil orientation; however, such a simple, immediate proxy of stimulation effect is not available when applying TMS almost anywhere else in the brain (with the partial exception of phosphenes evoked by suprathreshold stimulation of visual cortex). As more clinical and neuroscientific applications seek to apply TMS to other brain areas, new methods for quantifying immediate stimulation effect are needed. TMS-EEG offers a variety of possible solutions to these issues. For example, amplitudes of specific latency evoked components (discussed below) may be measured to infer stimulation effect or other diagnostic information (Du et al., 2017; Saari et al., 2017). Additionally, EEG can provide information on longer-term effects of TMS interventions, such as over the course of several minutes of pulses, or an entire intervention session (Casarotto et al., 2010; Chung et al., 2015; Komssi and Kähkönen, 2006; Werf and Paus, 2006). Finally, as discussed in greater detail in Chapter 4, EEG can provide information on the pre-stimulation state of the brain that can potentially be used to tailor stimulation parameters in real time (Zrenner et al., 2016, 2018).

3.1.1 Typical TEP components

Across various TMS-EEG studies with a variety of stimulation paradigms, a common set of typically observed TMS-evoked potentials (TEPs) have been documented. While these components are not the same for every individual, and some vary significantly depending on the stimulation target and other parameters, they provide a useful framework for describing responses to stimulation. These components are named based on their typical latencies and

signs at a particular electrode (e.g. the N100 typically involving a negative deflection at around 100 ms post stimulation at electrode Cz).

Some of the shortest latency components that have been reported are the P5 and N8 (Veniero et al., 2010, 2013). These were originally attributed to at least partially constitute a direct response to stimulation in the primary motor cortex. However, significant muscle artifacts can dominate at these low latencies, and it is therefore difficult to reliably demonstrate that these observed low latency signals are not peripheral in origin (Chung et al., 2015; Mutanen et al., 2013; Rogasch et al., 2013).

A more robustly observed component is the P30, sometimes grouped with the N15 as the N15-P30 complex (Chung et al., 2015; Paus et al., 2001). Some evidence has demonstrated a positive correlation between P30 and evoked MEP amplitude (Mäki and Ilmoniemi, 2010); combined with evidence from paired pulse experiments (Ferreri et al., 2011; Rogasch et al., 2013), it has been suggested that the P30 represents excitatory activity at the site of stimulation. Conversely, other studies have documented a more central distribution of the P30 with spreading to the contralateral hemisphere (Bonato et al., 2006; Vernet et al., 2013).

The N45 component has been consistently localized near the targeted stimulation region during M1 stimulation (Bonato et al., 2006; Komssi and Kähkönen, 2006; Komssi et al., 2004; Paus et al., 2001). It is possible that the N45 could partially represent somatosensory feedback from sensation during evoked movement, based on the conduction delays between M1/S1 and peripheral muscles. However, the N45 has been clearly shown to be evoked by both subthreshold and suprathreshold stimulation, thus providing evidence for at least a partial central contribution to the component (Komssi and Kähkönen, 2006; Paus et al., 2001). More

recently, pharmacological studies have indicated that the N45 component is mediated by activation of GABA-A receptors (Premoli et al., 2014a)

The P55 or P60 component has been attributed to inhibitory processes in the primary motor cortex (Van Doren et al., 2015), but it along with the P30 may also partially represent an auditory-evoked component (Komssi and Kähkönen, 2006)

The N100 is perhaps the most robustly observed component, and has largely been attributed to inhibitory processes (Bender et al., 2005; Bonnard et al., 2009; Chung et al., 2015; Kičić et al., 2008; Nikulin et al., 2003). It has been associated with attention-related processes (Bruckmann et al., 2012; Kaarre et al., 2018; Van Doren et al., 2015). There is evidence that the N100 is mediated by GABA-B receptor activity (Premoli et al., 2014b, 2014a). However, there is also evidence that some contributions to the N100 are artifactual in origin (Braack et al., 2013; Conde et al., 2017; Komssi and Kähkönen, 2006; Tiitinen et al., 1999).

Many of these components have been extensively studied only with stimulation to the primary motor cortex. Some components, especially the N100, seem to be robustly activated by stimulation of other regions as well (Bender et al., 2005; Casula et al., 2014; Chung et al., 2015; Du et al., 2017; Johnson et al., 2012; Kaarre et al., 2018; Rogasch et al., 2015).

The most robustly observed later components are the P180 and N280, often grouped as the P180-N280 complex. These have largely been attributed to be auditory-evoked potentials, with significant attenuation of the P180-N280 complex with auditory masking and other methodological alterations to control for bone-conducted sound (Braack et al., 2013; Casali et al., 2010; Casarotto et al., 2010; Komssi and Kähkönen, 2006). However, various controls still do

not completely abolish the P180-N280 complex, suggesting persistent auditory/somatosensory evoked components or a true more direct central effect of stimulation (Braack et al., 2013).

3.1.2 Variability

While TEPs elicited are fairly consistent between individual pulses and between days for a given subject and stimulation parameters (Casarotto et al., 2010; Kerwin et al., 2017; Lioumis et al., 2009), there is a large amount of variability between individuals. Although components are named according to characteristic latencies, their exact latencies can vary between individuals, and differences in cortical anatomy can cause variations in which scalp electrodes measure maximal deflections for a given component, even for functionally identical active regions.

Typical approaches for TEP analysis often involve extracting amplitudes at a global fixed latency for a given component (e.g. 100 ms across all individuals), or extracting a peak amplitude detected within a time span around the typical latency (e.g. the maximum value between 85 and 115 ms) (Du et al., 2017; Kerwin et al., 2017; Opie et al., 2017; Petrichella et al., 2017; Saari et al., 2017). While a simple single-channel peak detection approach can work well for identifying latencies of robust isolated components, it tends to have issues handling earlier latency components that vary more widely in spatial topography and that overlap temporally with other nearby components. To address these issues with variable temporal and spatial profiles of evoked components, a novel approach of Gaussian component fitting was implemented here. This approach takes as input a set of typical ERP components with limits for parameters (e.g. earliest and latest allowable latency for an N100), and fits Gaussian basis functions with latencies and widths automatically tuned to individual subjects and average or per-epoch amplitudes across channels, as described in detail below.

3.2 Methods

EEG was recorded throughout the TMS blocks in the sequential rTMS-BCI and concurrent TMS-BCI experiments described in the previous chapter. This chapter focuses on this data recorded during TMS, instead of the BCI-specific electrophysiology results previously reported. Specifically, these experiments provided EEG data recorded during (1) intermittent single pulses to left M1 at 120% RMT at rest across 56 sessions (20 subjects), (2) repetitive trains of 1 Hz simulation to four cortical targets at 90% RMT at rest, (3) intermittent single pulses to three cortical targets at both 90% and 120% RMT at rest and during specific motor imagery tasks. See the previous chapter for shared methodological details.

3.2.1 TEP signal processing pipeline

TMS induces large electrical artifacts in concurrently recorded EEG. To reduce these TMS-specific artifacts and other endogenous non-neural signals (eye blink, other muscle activity), an extensive signal processing pipeline was employed, as illustrated in the early stages of Figure 3.1. Within each block of recorded data, line noise was filtered using Slepian tapers and subtraction of an iteratively estimated sinusoidal noise component in sliding windows, adapted from the PREP pipeline (Bigdely-Shamlo et al., 2015). As part of this process, the data was temporarily high-pass filtered for more effective line noise estimation, a time course of the subtracted line noise was obtained, and then subtracted from the un-filtered original data. This process minimizes the effect of any filtering on the sharp transient signals at TMS pulse onset times.

Consistently noisy channels were rejected (typically fewer than 2 out of 64 channels) and replaced with spherically interpolated values. Data was then rereferenced to the global average and epoched relative to the TMS pulse onset.

For the particular TMS stimulator used in these experiments (the Magstim Rapid^2), there is a robust transient artifact ≈5 ms in duration at several tens of milliseconds after each pulse, with the post-pulse delay being a function of stimulation intensity; this has been attributed to recharge circuitry in the stimulator (Veniero et al., 2009). The precise latency of this recharge artifact was dynamically estimated from the average TEP within each block of data, and a 5 ms period centered at this latency was removed and replaced with spline interpolation from adjacent samples in individual channel time courses. Data were then downsampled from 5 kHz

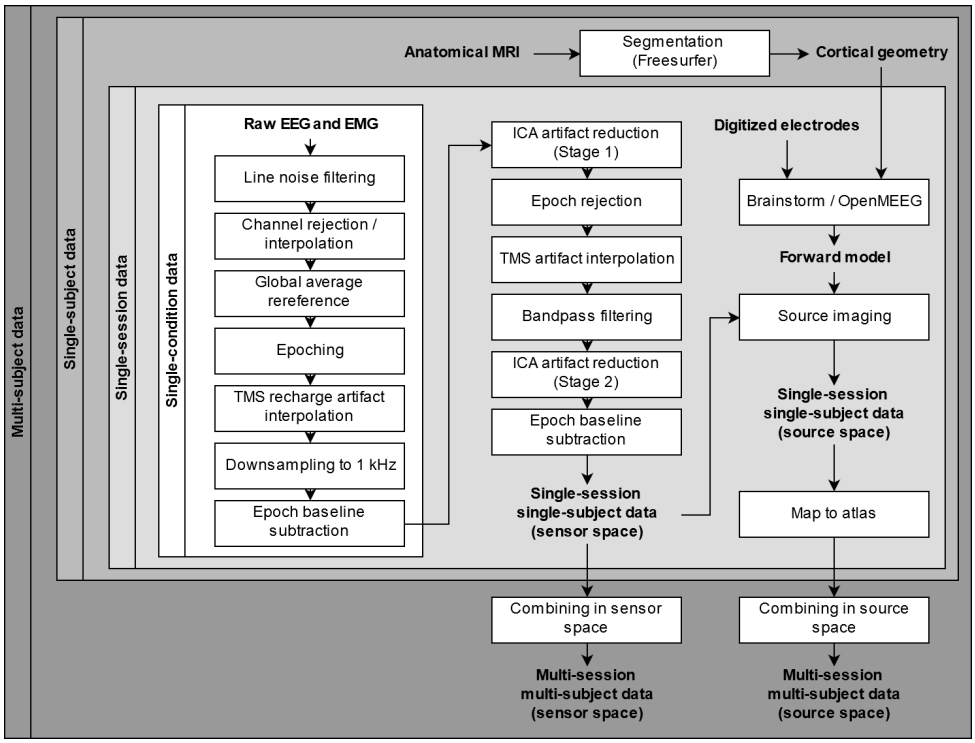

Figure 3.1: Block diagram of TMS-EEG signal processing pipeline.

to 1 kHz, and mean baseline values during a time period of [-500,-100] ms relative to pulse onset were subtracted from each epoch.

Removal/attenuation of the main TMS artifacts was accomplished primarily by a two-stage ICA-based artifact reduction pipeline, similar to that described in Rogasch et al. (2014, 2016). Prior to the first ICA stage, the primary TMS artifact was removed by zeroing the data between [-2,20] ms relative to TMS pulse onset. ICA (fastica) was then run to decompose the data, and primary decay artifact components were detected and removed. In the following stage, noisy epochs were identified and rejected; reasons for entire epoch rejection were primarily large muscle artifact (e.g. jaw clench) or coil movement causing large electrode fluctuations. The previously zeroed primary artifact timespan ([-2,20] ms) was then spline interpolated to reduce filter ringing artifacts and the data were zero-phase bandpass filtered with a 4th order Butterworth filter with cutoffs at 1 and 100 Hz. A second stage of ICA decomposition and component rejection was then run; this stage was used to reject any residual TMS-related decay and muscle artifacts, endogenous non-neural signals including eye blinks and other eye movement, temporal muscle activity, and components of noisy channels identified by poor correlations with neighboring channels (Rogasch et al., 2014, 2016). Finally, data were again baseline corrected based on a time period of [-500,-100 ms] relative to each pulse.

3.2.2 Gaussian component fitting

To account for the significant inter-individual variability in temporal and spatial profiles of TEP components, a novel Gaussian component fitting approach was implemented.

Given an array of multichannel, multi-epoch TEP data $\{\boldsymbol{D}_1, \boldsymbol{D}_2, \dots, \boldsymbol{D}_{N_e}\}$ with the data for epoch $e \in 1..N_e$ represented as $\boldsymbol{D}_e \in \mathbb{R}^{N_{ch} \times N_t}$, we can work with the average across epochs as

$$\boldsymbol{D} = \frac{1}{N_e}\sum_{e=1}^{N_e}\boldsymbol{D}_e \tag{3}$$

We can then write the average TEP for a given channel $c \in 1..N_{ch}$ as $\boldsymbol{d}_c \in \mathbb{R}^{N_t}$.

Assuming we want to fit components with a Gaussian profile, a unit amplitude basis template can be expressed as

$$\boldsymbol{b}_{\ell,w} = e^{-\left(\frac{\boldsymbol{t}-\ell}{w/3}\right)^2} \tag{4}$$

Where ℓ and w are latency and width parameters, respectively.

We can then fit an amplitude for this single template component based on a single-channel vector of data as

$$a = \boldsymbol{d}_c \cdot \frac{\boldsymbol{b}_{\ell,w}}{\left\|\boldsymbol{b}_{\ell,w}\right\|_2^2} \tag{5}$$

Alternatively, we construct a basis set of $\boldsymbol{N_{co}}$ components as

$$\boldsymbol{B}_{\boldsymbol{\ell},\boldsymbol{w}} = \left[\boldsymbol{b}_{\ell_1,w_1}, \boldsymbol{b}_{\ell_2,w_2}, \ldots\right]^T \in \mathbb{R}^{N_{co}\times N_t} \tag{6}$$

And the amplitudes $\boldsymbol{a}$ for this basis set can be fit from data with

$$\boldsymbol{a}_c = \boldsymbol{B}_{\boldsymbol{\ell},\boldsymbol{w}}^{\dagger\ T}\boldsymbol{d}_c \tag{7}$$

Where † is the pseudoinverse. We can then reconstruct an approximation of the original data as

$$\widehat{\boldsymbol{d}}_c = \boldsymbol{B}_{\boldsymbol{\ell},\boldsymbol{w}}^T\boldsymbol{a}_c \approx \boldsymbol{d}_c \tag{8}$$

And calculate the residual as $\boldsymbol{r}_c = \boldsymbol{d}_c - \widehat{\boldsymbol{d}}_c$.

After fitting to each channel using a shared basis set $\boldsymbol{B}_{\boldsymbol{\ell},\boldsymbol{w}}$ with independent per-channel amplitudes $\boldsymbol{a}_c$ for $c \in 1..N_{ch}$, we can write the total fitted amplitudes as

$$\boldsymbol{A} = [\boldsymbol{a}_1, \boldsymbol{a}_2, \ldots]^T \in \mathbb{R}^{N_{ch} \times N_{co}} \tag{9}$$

Such that the multichannel fitted data is $\widehat{\boldsymbol{D}} = \boldsymbol{A}\boldsymbol{B}_{\boldsymbol{\ell},\boldsymbol{w}} \approx \boldsymbol{D}$ and the multichannel residual is $\boldsymbol{R} = \boldsymbol{D} - \widehat{\boldsymbol{D}}$.

The challenge here is how to choose $\boldsymbol{\ell}$ and $\boldsymbol{w}$ to construct the basis set $\boldsymbol{B}_{\boldsymbol{\ell},\boldsymbol{w}}$. One option is to optimize the basis set for a single channel of interest (e.g. Cz), fix the latencies and widths accordingly, and then fit gains across all channels. This assumes that the single chosen channel is representative of all relevant activity measured on the scalp. Such a fitting procedure is relatively straightforward for a small number of components and can be accomplished with something like MATLAB's built-in nonlinear least squares fitting methods.

However, it is more useful to not constrain the fitting of width and latency parameters to a single channel. Instead, we can use a more generic optimization approach to minimize the residual, in the form

$$\underset{\boldsymbol{\ell},\boldsymbol{w}}{\operatorname{argmin}} \|\boldsymbol{R}\|_F \tag{10}$$

(where $\|\cdot\|_F$ is the Frobenius norm), subject to constraints on $\boldsymbol{\ell}$ and $\boldsymbol{w}$ based on the number of expected components and "reasonable" latency and width spans.

The cost function in Equation (10) is not generally well-behaved, with various local minima. Therefore, it is preferable to use an optimization approach that can handle exploration of the parameter space without getting trapped excessively in local minima. Here, we used an

implementation of particle swarm optimization in MATLAB (Chen, 2018; Kennedy et al., 2001; Mikki and Kishk, 2008; Perez and Behdinan, 2007).

Some modifications can be made to the cost function in Equation (10) to improve fitting behavior. To minimize the occurrence of rank-deficient overlapping component bases, an extra term can be added to the cost function to penalize excessively large fitted components that cancel out when being summed into the total fit:

$$\underset{\boldsymbol{\ell},\boldsymbol{w}}{\operatorname{argmin}} \left(\|\boldsymbol{R}\|_F + \alpha \left\| |\boldsymbol{A}| \boldsymbol{B}_{\boldsymbol{\ell},\boldsymbol{w}} \right\|_F \right) \tag{11}$$

Where α is a relative cost weight and $|\boldsymbol{A}|$ is the element-wise absolute value of the amplitude matrix $\boldsymbol{A}$.

In typical TEPs, the lower latency components (e.g. < 120 ms) are usually shorter in duration and may be lower in amplitude than some later components. The cost may therefore be dominated by the quality of fit to the larger, later components. To counteract this, the residual can be temporally weighted, such as with a simple split multiplying all residuals before 120 ms by a factor greater than 1 to give them more weight, with the cost function:

$$\underset{\boldsymbol{\ell},\boldsymbol{w}}{\operatorname{argmin}} \|\boldsymbol{R} \circ \mathbf{1}\boldsymbol{\tau}^T\|_F \tag{12}$$

Where $\circ$ is the Hadamard product, $\mathbf{1}$ is a vector of ones, and $\boldsymbol{\tau}$ is a vector of temporal weights. In this work, these weights were set such that

$$\tau_t = \begin{cases} 4, & t < 120 \text{ ms} \\ 1, & t \geq 120 \text{ ms} \end{cases} \tag{13}$$

Finally, some electrodes may have large components not of interest to be fitted, such as residual eye blink artifact in frontal electrodes. This a priori information can be incorporated by weighting the residual by channel:

$$\underset{\boldsymbol{\ell},\boldsymbol{w}}{\operatorname{argmin}}\|\boldsymbol{\gamma}\mathbf{1}^T \circ \boldsymbol{R}\|_F \tag{14}$$

Where $\boldsymbol{\gamma}$ is a vector of channel weights. In this work, these weights were set such that

$$\gamma_{ch} = \begin{cases} 1, & ch \in \text{central electrodes} \\ 0, & ch \in \text{peripheral electrodes} \end{cases} \tag{15}$$

Combining all these modifications, the final cost function used in this work was

$$\underset{\boldsymbol{\ell},\boldsymbol{w}}{\operatorname{argmin}} \left(\left\| \boldsymbol{\gamma}\mathbf{1}^T \circ \left(\boldsymbol{D} - \boldsymbol{A}\boldsymbol{B}_{\boldsymbol{\ell},\boldsymbol{w}}\right) \circ \mathbf{1}\boldsymbol{\tau}^T \right\|_F + \alpha \left\| |\boldsymbol{A}| \boldsymbol{B}_{\boldsymbol{\ell},\boldsymbol{w}} \right\|_F \right) \tag{16}$$

Table 3.1: Gaussian component fitting parameter constraints

	Latency (ms)		Width (ms)	
Component	**Min**	**Max**	**Min**	**Max**
P30	20	35	20	40
N45	35	50	10	20
P55	45	75	10	45
N100	70	145	40	80
P180	130	220	40	150
N280	205	350	40	150

It was assumed that component latencies and widths were approximately constant within a session and stimulation condition, and particle swarm optimization was run using the cost function in Equation (16) with $\boldsymbol{D}$ being the average multichannel ERP. Six components were used, with latency and width constraints shown in Table 3.1; these parameter constraints were empirically selected based on typical observed components and fitting behavior in several test datasets; these parameter constraints could be adjusted based on more comprehensive data in future work. Once the fitted component latencies and widths were obtained, per-epoch component amplitudes could be calculated using Equation (7) with per-channel per-epoch data instead of the average over all epochs.

3.2.3 Source analysis

Interindividual differences in cortical anatomy affect the EEG signals measured on the scalp, resulting in different scalp topographies between individuals even if the underlying cortical sources are identical. Additionally, volume conduction of signals between a cortical source and the measurements on the scalp results in blurring or mixing of source activity. EEG source imaging was used to account for some of this interindividual anatomical variability and to incorporate a priori information from subjects' MRI data.

Subject-specific MRI data were segmented into varying tissue types (white matter, gray matter, CSF, skull, and scalp) using FreeSurfer (Fischl, 2012). The segmented boundary meshes were then used to construct a boundary element method (BEM) model with Brainstorm and OpenMEEG (Gramfort et al., 2010; Kybic et al., 2005; Tadel et al., 2011). Electrode positions in the model were based on the digitized positions recorded at the end of each session. Source dipoles were constrained to be perpendicular to the cortical surface. Weighted minimum norm

estimation (wMNE) (Gramfort et al., 2014) was employed to estimate an inverse solution mapping scalp measurements back to the underlying gray matter surface.

While source results for individual subjects could be viewed on individual anatomy, for group level analysis it was necessary to project activity to a common brain. Individual subject's cortical source estimation data were mapped with Shepard's interpolation using FreeSurfer's spherical surface-based coregistration to an ICBM152 atlas surface for group averaging (Fischl et al., 1999; Fonov et al., 2009, 2011; Shepard, 1968; Tadel et al., 2011).

3.3 Results

Figure 3.2 shows the results of Gaussian component fitting of TMS-evoked potentials in a single subject receiving stimulation at 120% of RMT to left M1. As shown by the butterfly plots in Figure 3.2A, the fitted Gaussian components were able to represent most of the variance in the average signal, with the residual after fitting representing a relatively small portion of the original average signal energy. Figure 3.2B and Figure 3.2C show slightly different variants of scalp and inverse estimated cortical activity topographies. Figure 3.2B is a more conventional plot of topographies, in which the fitted peak latencies from the Gaussian components are used to extract raw per-channel (or per-source) signal amplitudes at that instant in time. In most cases, this representation can capture most of the apparent information in the average TEP. However, in cases where temporally adjacent components overlap significantly, the time-specific topographies may show a superposition of activity from two or more components, without allowing easy disambiguation of spatial contributions of the mixed components. Some of this mixing is evident in the fitted component at 35 ms in Figure 3.2B, which has significant spatial similarity to the earlier component peaking at 23 ms. In contrast, Figure 3.2C shows per-

channel Gaussian fitted component amplitudes. These fitted amplitudes can provide some unmixing of superimposed components, operating on the assumption that the different Gaussian temporal profiles map to components that are also spatially different. This can be seen in the N45 fitted component in Figure 3.2C, which shows a more focal and unique spatial topography, with less apparent interaction with the earlier fitted P30 component.

Figure 3.3 shows the group-level TEPs evoked by stimulation to left M1 at 120% RMT, aggregated across all 56 rTMS sessions, each containing approximately 150-180 suprathreshold pulses (depending on the number of rejected epochs).

Figure 3.4 shows the group-level TEPs evoked by rTMS pulses during 90% RMT 1 Hz stimulation to left M1, left PMd_a, left PMd_p, and left SMG targets, for both real and sham stimulation. There is a consistent P180 component visible in all of the stimulation conditions, including sham, agreeing with previous reports that this component is largely caused by auditory and somatosensory evoked potentials rather than a direct central effect of stimulation. Shorter latency components have apparently greater degrees of target-specificity, with the N45 and P55 components in particular showing localization tending to vary with changes in the site of stimulation.

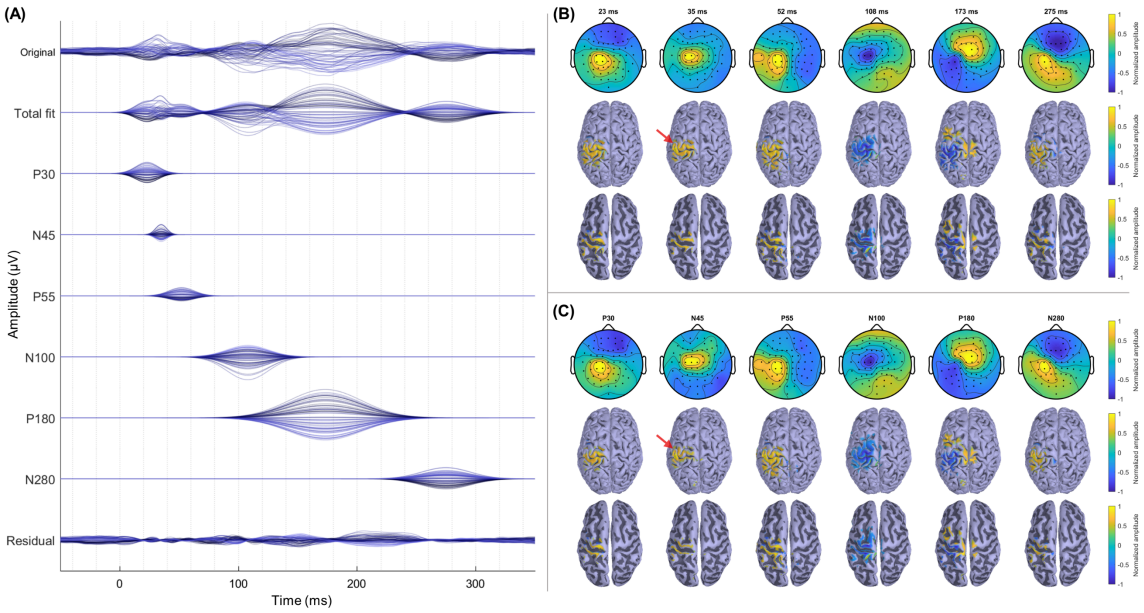

Figure 3.2: Gaussian component fitting results for TMS-evoked potentials from a single stimulation condition. *This data is for a single subject receiving intermittent single pulse stimulation at 120% of RMT to left M1. (A) shows butterfly plots with one trace per channel in each stacked plot, with trace colors varying from dark to light corresponding to channels varying from anterior to posterior on the scalp, averaged over all epochs in the dataset. The top subplot shows the original processed TEP prior to component fitting; the subplot below show the total fit, approximating the original data as a sum of the individual Gaussian components, which are shown in middle subplots. The bottom subplot shows the average residual after fitting. (B) shows scalp and source estimates corresponding to the original amplitudes at the peak latencies identified during fitting, with the cortical activity shown on the individual subject's gray matter surface, both in un-inflated (middle row) and inflated (bottom row) versions for improved visualization of activity extending into sulci. (C) shows similar plots to (B), but instead of showing the raw amplitudes at the identified latencies, these are plots of the individual fitted Gaussian component amplitudes. The red arrows indicate a particular region with a difference in profile of activity between (B) and (C).*

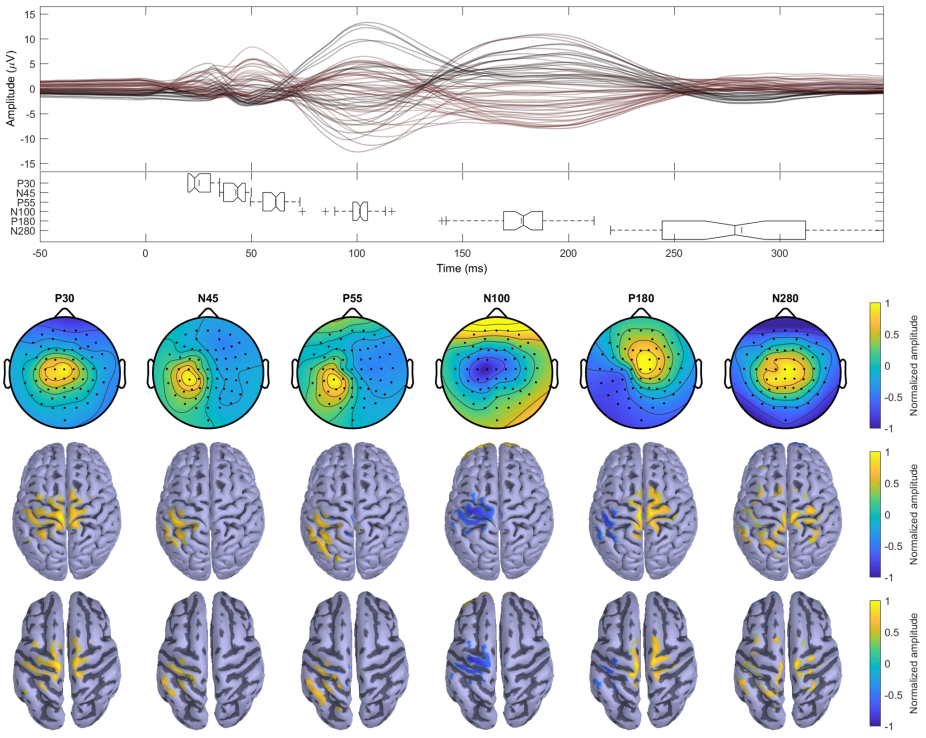

Figure 3.3: Group-aggregated TMS-evoked potentials for stimulation to left M1 at 120% RMT. *Results shown are aggregated from the excitability measurement blocks across all rTMS sessions. The top subplot shows a butterfly plot with one trace per channel, with trace colors varying from dark to light corresponding to channels ranging from anterior to posterior locations on the scalp. The boxplots show the distribution of latencies estimated by Gaussian component fitting within each session. Scalp and cortical source topographies were extracted at session-specific fitted TEP latencies and then averaged.*

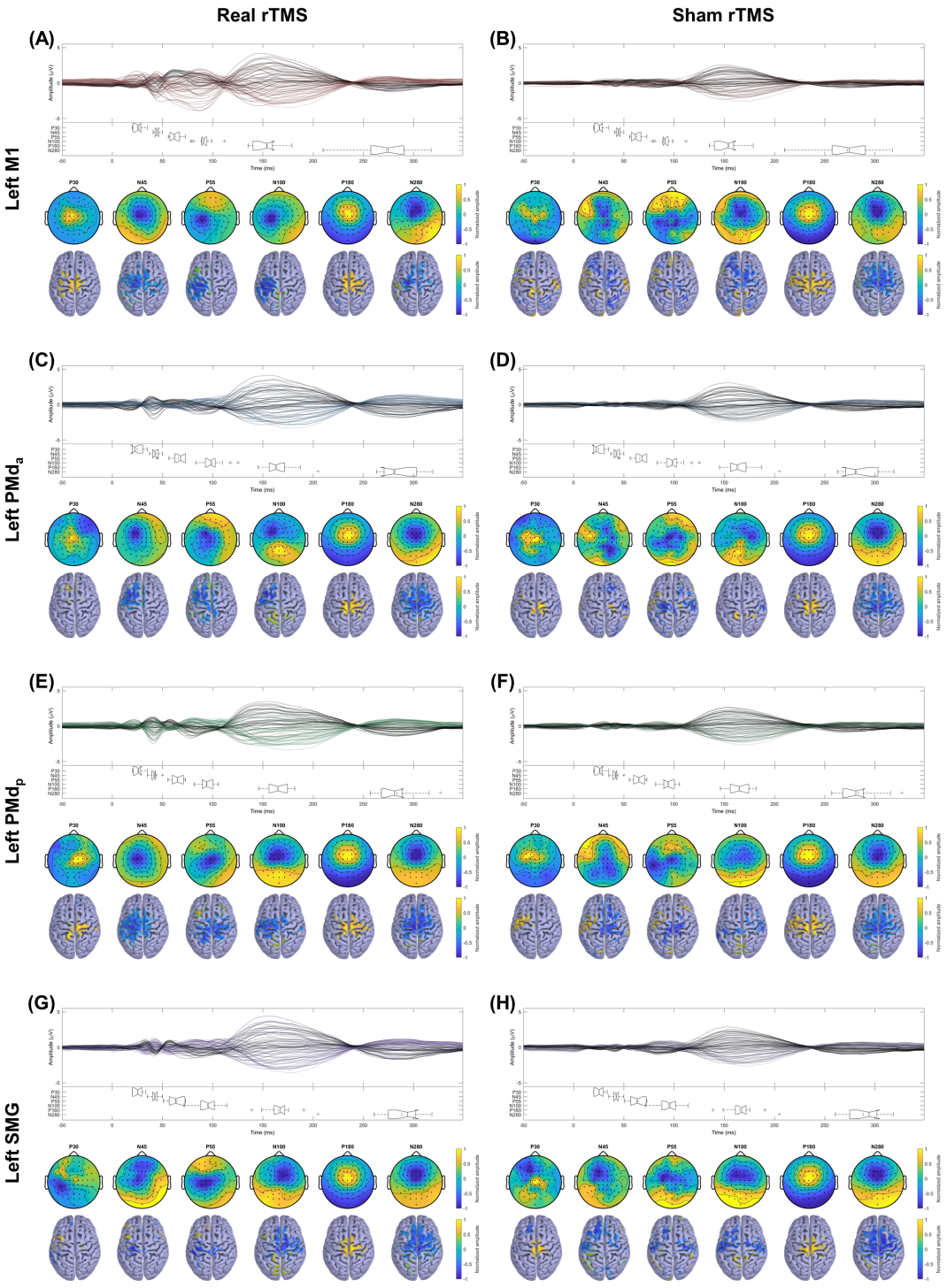

Figure 3.4: Group-aggregated rTMS-evoked potentials. *Results shown are for 1 Hz rTMS at 90% RMT to left M1 (A,B), left PMd$_a$ (C,D), left PMd$_p$ (E,F), and left SMG (G,H) for real (A,C,E,G) and sham (B,D,F,H) stimulation. The boxplots within each panel show the range of latencies estimated by Gaussian component fitting within each session. Scalp and cortical source topographies were extracted at session-specific fitted TEP latencies and then averaged.*

3.4 Discussion

The Gaussian component fitting procedure described here worked to distinguish evoked components in a variety of stimulation paradigms, including both intermittent suprathreshold stimulation to primary motor cortex, and in responses evoked by 1 Hz rTMS delivered at 90% RMT to four different sets of cortical targets. This fitting process requires minimal user intervention and no a priori assumptions on the spatial topography of evoked components, making it particularly useful for cases where topographies vary significantly either due to the targeting of a variety of stimulation sites, or due to large inter-individual variations in anatomy.

In the current implementation of the particle swarm basis optimization procedure, only temporal constraints are specified. One consequence of this is that components typically demonstrated to be of a certain sign in average scalp topographies (e.g. the N45) may be fitted as inverted peaks in some cases. While the N100 and P180 components are centrally located and of particularly robust signs, the specific topographies of earlier components can vary significantly based on differences in individual cortical anatomy, making it difficult to justify absolute rules on signs of given components at specific EEG channels. However, future alterations could be made to the basis tuning cost function and gain projections to incorporate a priori constraints on component signs.

The choice of Gaussian component profiles was empirical, based on well described typical TEP evolution profiles. For single trial component fitting and more complete modeling of average responses, it may be useful to consider other basis function shapes, such as skewed or exponentially modified Gaussian profiles with longer tails to model a sharp rise in amplitude soon after stimulation followed by a more gradual decay. However, the approach employed

here was sufficient for the current datasets and analysis techniques, given that the fitted models were able to explain most of the variance in the original signals with just six components.

The focus of the fitting results described here was on fitting average TEPs within subjects and aggregating the results for group level analysis. However, one key benefit of having a temporal basis function used for fitting is that it can potentially provide higher quality single-trial ERP amplitude estimates by effectively match filtering to look for an expected temporal component profile. This could be useful for future studies examining single-trial variability in responses and for applications using TEP features for online EEG-informed stimulation.

While the Gaussian component fitting procedure served to explain or model temporal variability in components across individuals, there is also considerable spatial variability in the topographies of evoked components. Here, we used source imaging methods to include a priori information on subject-specific anatomical features—i.e. building forward models from subject-specific MRI data modeling detailed curvature of gyri and sulci, and using surface curvature based mapping approaches to map between corresponding cortical regions in the atlas and individual brains. Group averaging of data in the common atlas source domain then allowed some degree of compensation for the individual anatomical differences generating different scalp topographies. However, it is difficult to completely validate this approach here without more precise ground truth data on the underlying activations. This issue can be addressed in part with computational simulations, which provide evidence that this source imaging approach is functioning as intended to help account for inter-individual anatomical differences (e.g. see Figure 1.3).

4 State dependency of TMS: effects of pre-stimulation context on pulse response

4.1 Introduction

Given the large amount of intra- and inter-individual variability in responses to TMS, there is a need to better understand factors influencing stimulation outcome. It can be hypothesized that the state of the brain immediately before stimulation has a strong effect on the post-stimulation response, both at the time scales of single pulses and over longer trains of stimulation.

Such state dependence has been demonstrated with various TMS paradigms. In a relatively extreme example of brain state dependence, it has been shown that TMS applied during sleep can elicit slow waves while identical stimulation during wakefulness does not (Massimini et al., 2007). In the visual system there is evidence that pre-stimulus occipital alpha power influences the likelihood of evoking visual phosphenes (Romei et al., 2008a, 2008b), and that TMS may act preferentially on different subpopulations in a stimulated region based on their baseline activity levels (Pasley et al., 2009; Perini et al., 2012; Silvanto and Pascual-Leone, 2008; Silvanto et al., 2007). Additionally, phase-dependent responses to TMS have been demonstrated in the visual system (Dugué et al., 2011). Behavioral state-dependent variation in stimulation effects have been demonstrated when stimulating dorsal premotor cortex during a motor task (Bestmann et al., 2008), and when stimulating the visual cortex during an attention task (Herring et al., 2015). Attempts to explain some variability in MEPs elicited by stimulation of primary motor cortex have suggested that power, synchrony, and phase features may all be predictive of MEP amplitudes to some degree (Ferreri et al., 2014; Sauseng et al., 2009; Schulz et al., 2014; Zrenner et al., 2018). Recent work has begun to explore the merits of informing online parameters of trains of stimulation for more effective modulation of excitability, such as by stimulating during

time periods of high or low oscillatory power (Bonnard et al., 2016; Kraus et al., 2016), or specific oscillatory phases (Bergmann et al., 2012; Zrenner et al., 2018).

In this work, we focus on two types of pre-stimulus state: behavioral task dependency, and oscillatory phase dependency, and specifically how these factors influence the TMS-evoked EEG response.

4.2 Methods

4.2.1 Experiments

The data for these analyses were collected as part of the experiments described in Chapter 2. Specifically relevant are (1) data recorded during the excitability measurement blocks of the sequential rTMS-BCI experiments, in which intermittent single pulses of TMS were applied to left M1 at 120% RMT at rest in 20 subjects across 56 sessions, and (2) data recorded during the concurrent TMS-BCI experiments in which intermittent single pulses of TMS were applied during motor and rest tasks, at both 90% and 120% RMT to left M1, left PMd, and vertex in 8 subjects across 13 sessions. See Chapter 2 for details on the experimental methods.

4.2.2 Preliminary signal processing

The data presented in this chapter were processed with the signal processing pipeline described in Chapter 3 to attenuate TMS-induced artifacts and other non-neural signals. See Chapter 3 for a detailed description of these signal processing methods.

4.2.3 Phase estimation

A large focus of this chapter is on sensitivity of TMS responses to pre-stimulation phase. Estimation of phase of a particular EEG signal immediately before each TMS pulse is non-trivial;

the need for eventual real-time estimation of phase, and the large TMS-induced artifact and potential for immediate oscillatory changes in response to TMS mean that the phase estimation must be causal—the estimation algorithm cannot use "future" data after the pulse to aid in pre-stimulation phase estimation.

Various phase estimators have been developed and applied to analyze neural signals (see Lepage et al. (2013) for a review), particularly to infer connectivity or synchrony between disparate brain regions. Examples include the Hilbert transform and complex Morlet wavelets. However, the most common forms of these estimators are acausal, in that they estimate phase at a given time based on a short window of time spanning both before and after this time. While causal Morlet wavelets can be employed to circumvent this issue to some degree, there are benefits to being able to predict phase some time in advance of the available data, such as in a real-time online estimate-and-stimulate setup (Zrenner et al., 2016, 2018). Here, we used a phase estimation approach similar to that described in Zrenner et al. (2018), fitting an autoregressive model to the data to then extrapolate time courses into the future and apply conventional acausal phase estimation approaches on this forward-predicted time course.

A simulated example illustration of this approach is shown in Figure 4.1. Here, an input signal was synthesized as a sum of three sinusoidal components at 3, 10, and 25 Hz with additive Gaussian noise. Assuming we want to estimate phase at time zero, but only have data before -100 ms, the chosen approach fits an autoregressive model using Burg's method and applies the model to extrapolate or forward predict up to (in this case) time 300 ms. The combined original plus extrapolated signal are then bandpass filtered at the frequency of interest (e.g. 10 Hz), and phase is extracted from an FFT-based Hilbert transform of the data. Without extrapolation, the effects of implicit zero-padding with convolution of the bandpass

filter cause transient signal deviations that lead to large errors in phase estimation even with very short forward prediction intervals.

For the phase estimation results here, analysis was performed on individual session data from the excitability measurement blocks of study 1 (see Chapter 2 for details). To reduce the impact of outlying data in which M1 may not have been targeted precisely, blocks within each session with median MEP amplitudes < 200 µV (representing < 10% of all data) were excluded.

4.2.4 Statistical analyses

To quantify the effects of task context on stimulation response, we used linear mixed effects models with fixed slopes, as implemented in the "lme4" library in R (Bates et al., 2014). The

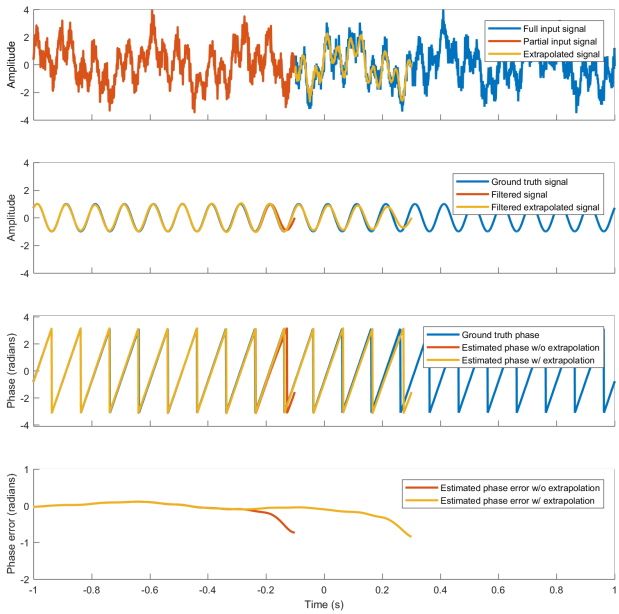

Figure 4.1: Simulated example of phase estimation approach. *(A) shows the synthesized input signal over the full timespan, reduced to just before -100 ms, and then the results of autoregressive model fitting and extrapolating to forward predict the signal. (B) shows the same signals after bandpass filtering around 10 Hz. (C) shows the results of extracting phase from the Hilbert transform of the signals in (B). Finally, (D) shows the phase estimate error as the deviation between the phases estimated with partial information versus those estimated with the full signal time course.*

mixed effects modeling approach allowed specification of random effects to account for variability across individual subjects and sessions. While aggregated results are presented in plots for visualization here, the mixed effects models were based on the non-aggregated data, incorporating information on the spread of within-condition repeated measures. Model coefficient confidence intervals were estimated via likelihood profiling (Bates et al., 2014).

To quantify relationships between pre-stimulation alpha phase and resulting MEP amplitudes, we used a combination of binning and per-session aggregation to find group-level sensitivity curves. Because the relevant phase scale (i.e. bin size) was not known a priori, several different bin sizes were evaluated. Determining whether these resulting binned sensitivity curves are statistically significant while accounting for differences in number of bins, number of aggregated groups, and the potential for biases in phase estimation resulting in nonuniform distributions of phase estimates is not straightforward. To solve this issue, we used a randomization approach to estimate a distribution for the null hypothesis: for each of 1000 repetitions, pairings between estimated phases and MEP values were shuffled within sessions, processed with the same binning and group aggregation methods as used on the non-shuffled data, and used to find the intervals containing all but N of the median phase bin values for 95% of the shuffled repetitions. These intervals can be interpreted as follows: for N=1, we would expect 95% of null datasets with no relationship between phase and EMP amplitude to have no median phase bin values exceeding the interval, and therefore an observation with at least one median phase bin value exceeding the interval is unlikely to be a chance result.

4.3 Results

4.3.1 Motor task dependency

Figure 4.2 shows aggregated peak-to-peak MEP amplitudes evoked by stimulation to the three cortical targets at subthreshold and suprathreshold intensities. As expected, suprathreshold stimulation to left M1 was the condition that most robustly evoked large amplitude MEPs. The stimulation at 120% RMT targeted to left PMd_p also elicited moderate amplitude MEPs, presumably due to direct activation of M1 given that the coil orientations for targeting M1 and PMd_p were in close proximity. The results of linear mixed effects modeling of the MEP amplitudes as a function of condition and task are shown in Figure 4.3. The drastically larger non-normalized MEP amplitudes for the suprathreshold M1 and suprathreshold PMd_p are apparent in Figure 4.3A, with this also showing that the slightly elevated MEP amplitudes for subthreshold stimulation are significant. The task-specific model coefficients shown in Figure 4.3B indicate that the main significant task-specific effect was decreased MEP amplitudes for

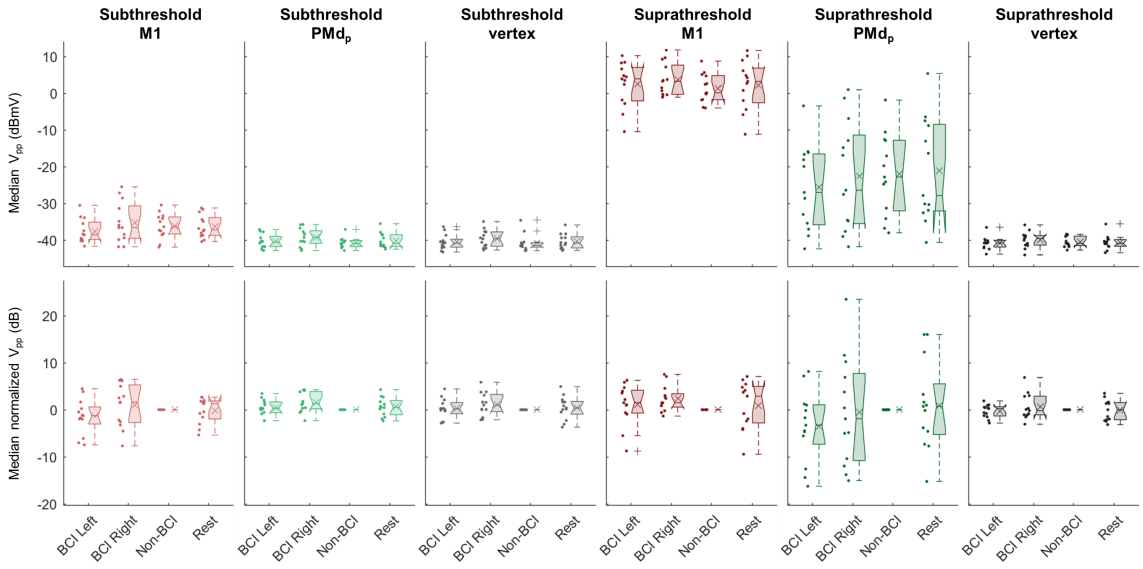

Figure 4.2: Task-dependent variations in MEP amplitudes. *The top row of plots shows un-normalized peak to peak amplitude values, while the bottom shows values after per-session normalization to median amplitude in the non-BCI blocks.*

stimulation to left PMd_p during BCI left tasks, with a 95% confidence interval of [-4.93, -1.50] dB. Stimulation to right M1 produced a marginally significant elevation in MEP amplitudes, with a 95% confidence interval of [0.01, 3.43] dB.

Aggregated TEPs are shown in Figure 4.4, and represent the average TEPs evoked by each specific stimulation target and intensity combination, with all task conditions pooled. Note that there is intrinsic variation in TEP amplitudes across stimulation targets, with (particularly for earlier components) very different spatial topographies associated with each peak latency. Several features are evident from the butterfly plots in this figure: spatial profiles of stimulation common to each stimulation target but varying in amplitude as a function of stimulation intensity, and evoked components common across all stimulation conditions. These latter components are evident even in stimulation to vertex, which is generally targeted as a control

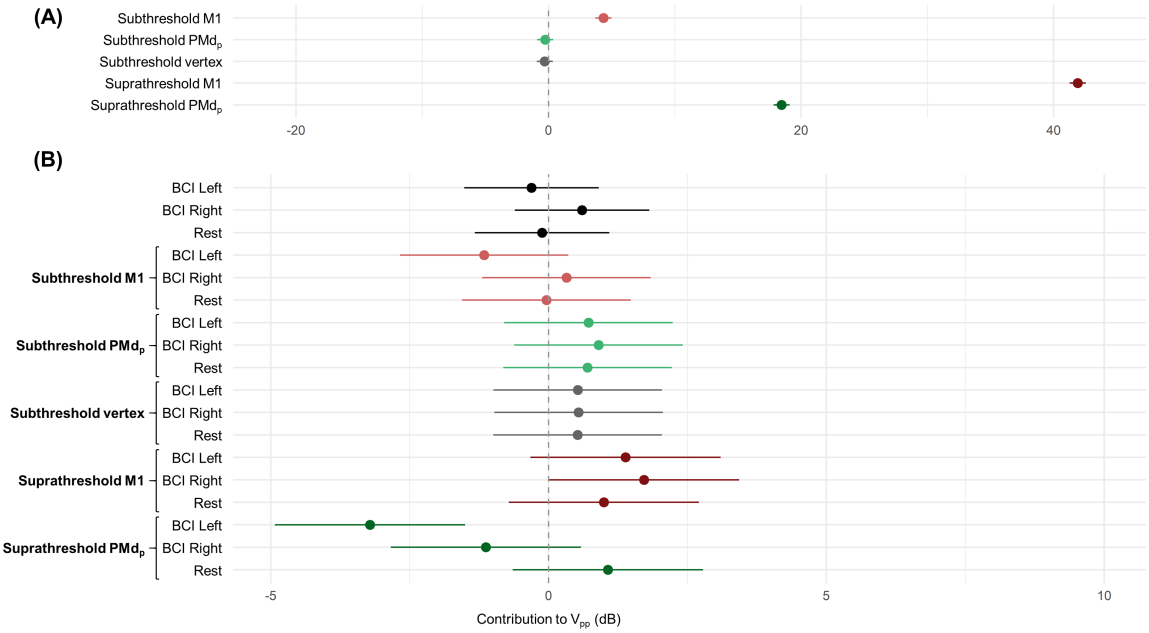

Figure 4.3: Linear mixed effects model coefficients for MEP amplitudes as a function of task and stimulation condition. *Bars indicate 95% confidence intervals. Values can be interpreted as modeled contributions to MEP amplitude relative to the suprathreshold vertex and non-BCI conditions. Coefficients in (A) and (B) are from the same model, but shown on different horizontal scales for clarity.*

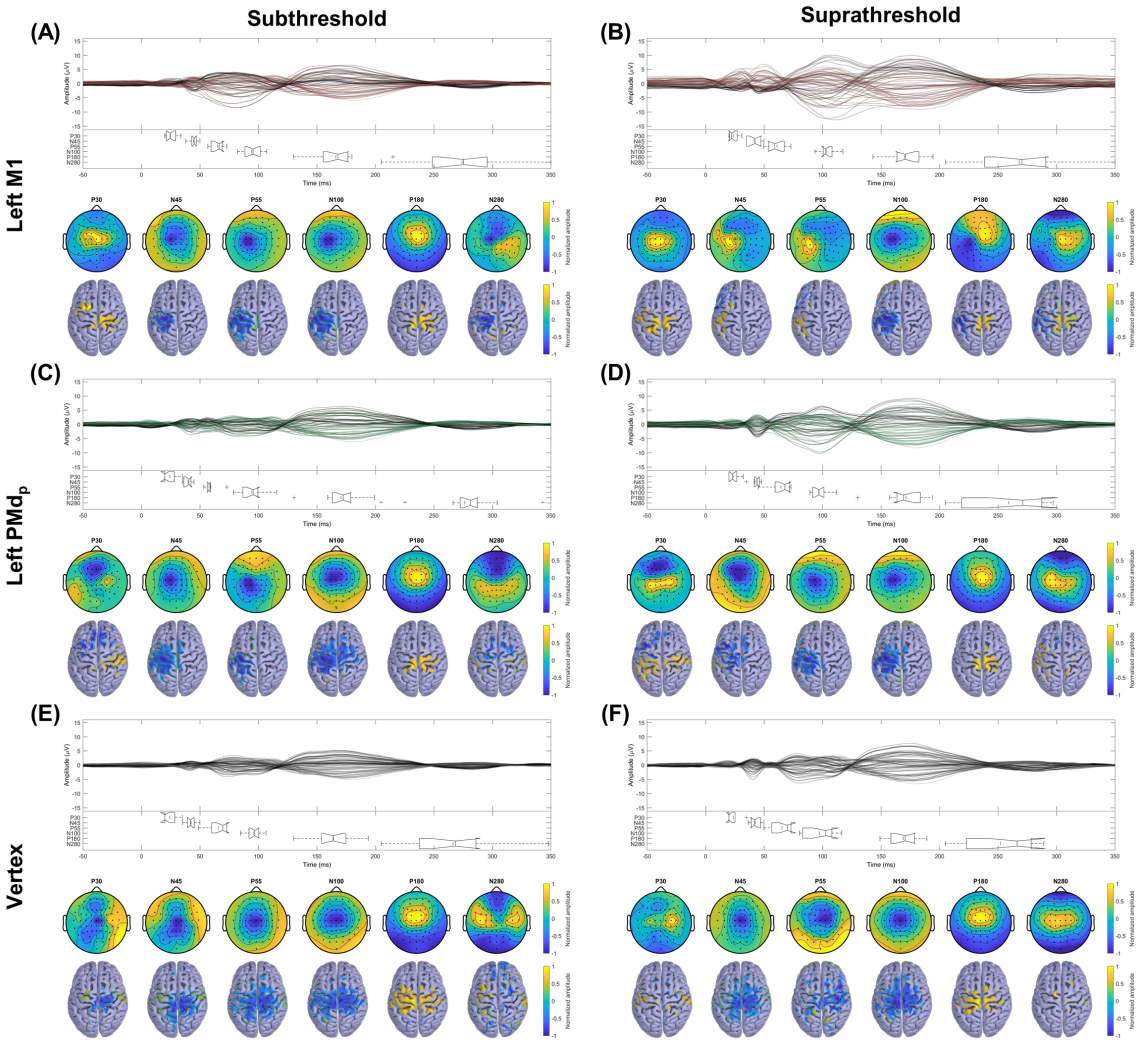

Figure 4.4: Mean TEPs for intermittent subthreshold and suprathreshold pulses to left M1, left PMd_p, and vertex targets aggregated across all sessions and task conditions.

region with very little neural tissue; therefore these specific components likely reflect, at least in part, auditory or somatosensory evoked potentials rather than any more direct electromagnetic stimulation of the brain. However, particularly with the suprathreshold intensity, it is possible that the vertex stimulation condition is directly affecting some adjacent neural tissue.

Figure 4.5 and Figure 4.6 show TEP amplitude components for electrode C3 aggregated within subject, task, and stimulation condition. These TEP amplitudes are based on session- and

stimulation-specific Gaussian component fits, as described in Chapter 3. Figure 4.8 shows the results of linear mixed effects modeling of the contributions of task and stimulation conditions to C3 N100 amplitudes for the same data. The top several coefficients reflect target-specific but not task-specific effects, with it being expected to see very different N100 (and other TEP component) amplitudes depending on the stimulation site. The main task-specific effects were for BCI left, BCI right, and rest conditions during subthreshold M1 stimulation all having more positive (in most cases corresponding to a reduced negative amplitude) N100 amplitude relative to the N100s evoked during the non-BCI rest blocks.

To further explore the differences in N100 amplitude indicated by the linear mixed effects model, Figure 4.7 shows aggregated difference TEPs contrasting several pairs of task conditions during subthreshold stimulation of left M1. In particular, the more positive (reduced negative amplitude) N100 at C3 is evident in Figure 4.7A and Figure 4.7B; source imaging estimates suggest that this change is localized primarily to the left precentral gyrus.

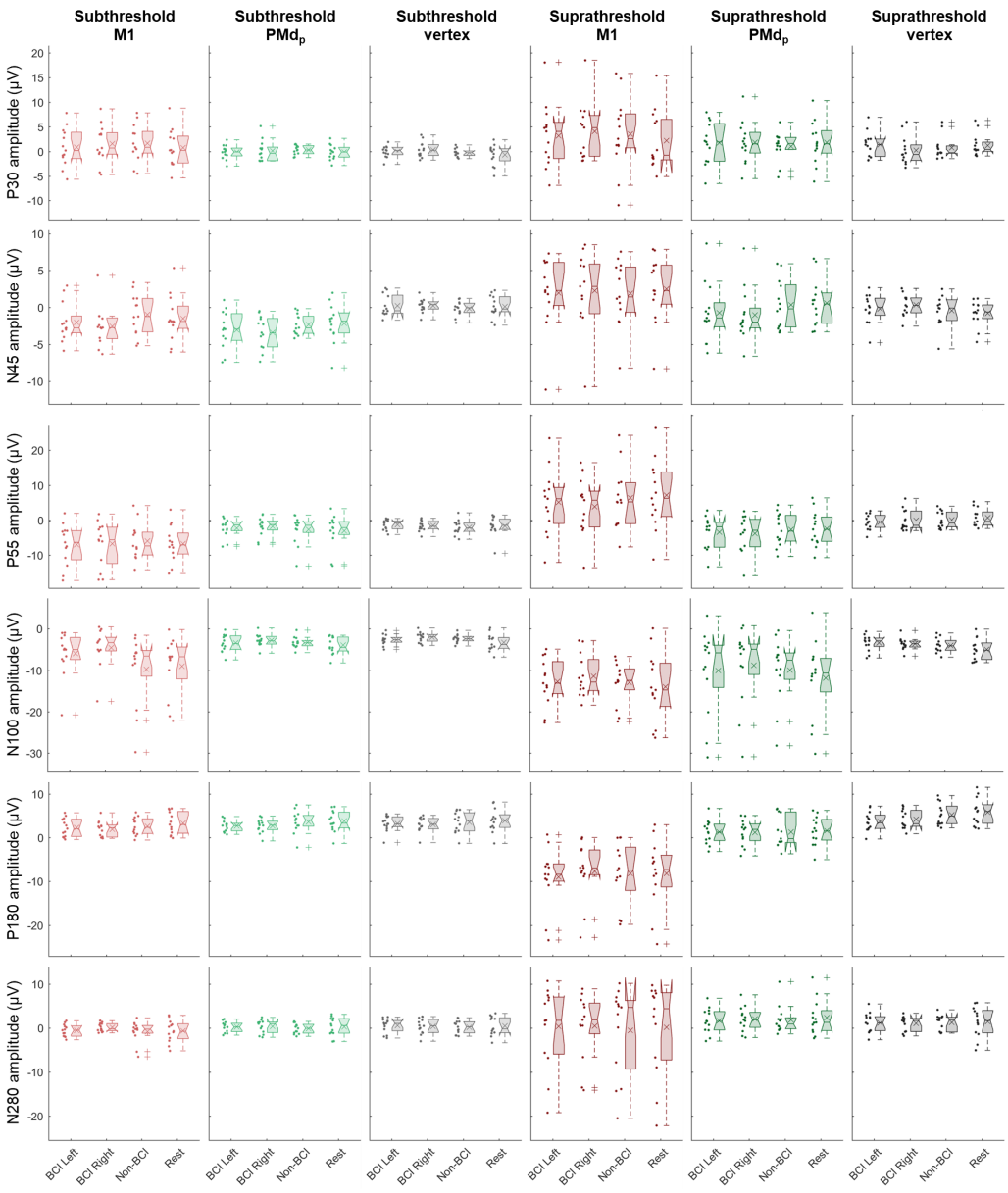

Figure 4.5: Task-dependent variation in TEP amplitudes. *Amplitudes shown are for electrode C3, obtained from Gaussian component fits, and aggregated within each task, stimulation condition, and session.*

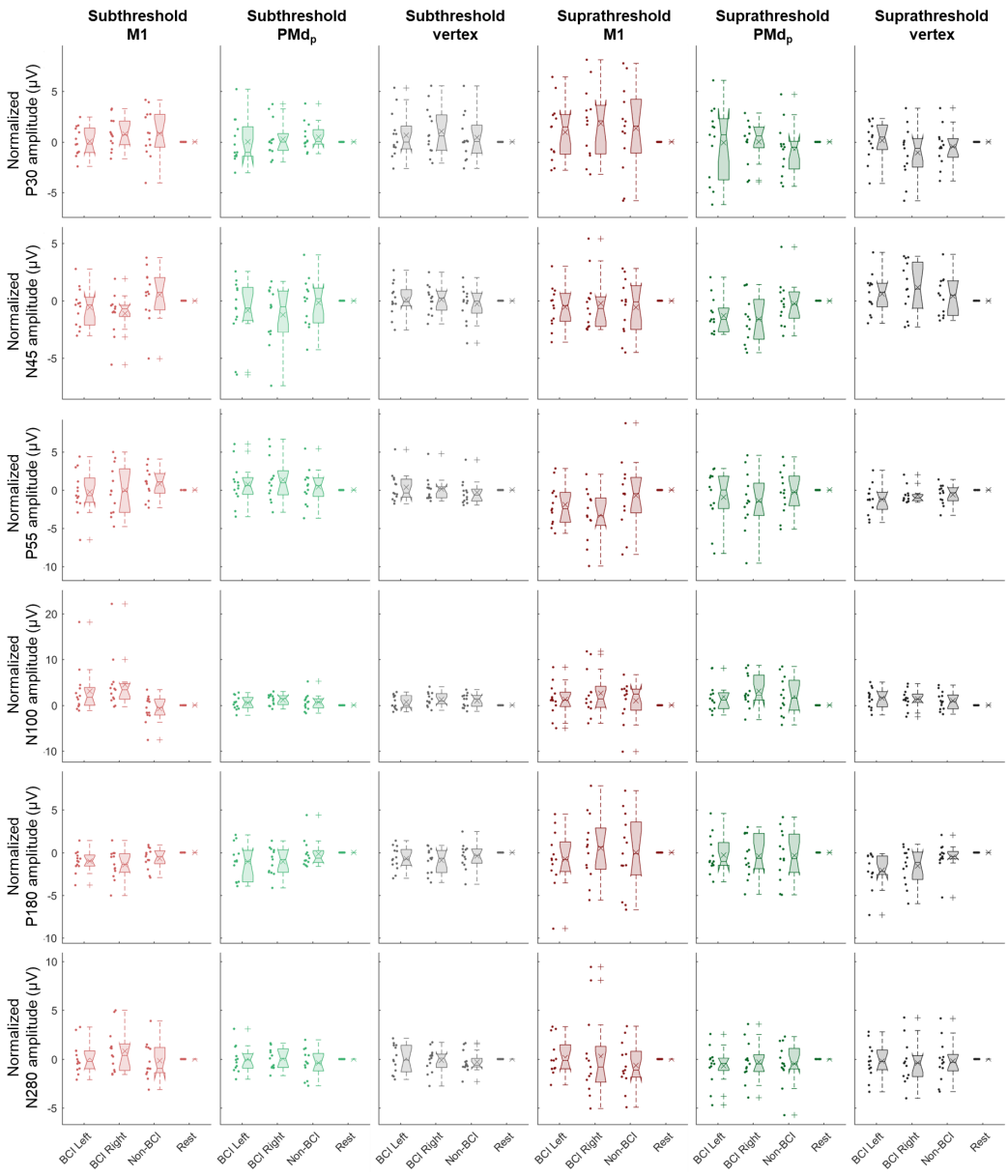

Figure 4.6: Task-dependent variation in normalized TEP amplitudes. *Amplitudes shown are for electrode C3, obtained from Gaussian component fits, normalized by subtracting the mean TEP amplitude in the rest condition within each stimulation condition and session.*

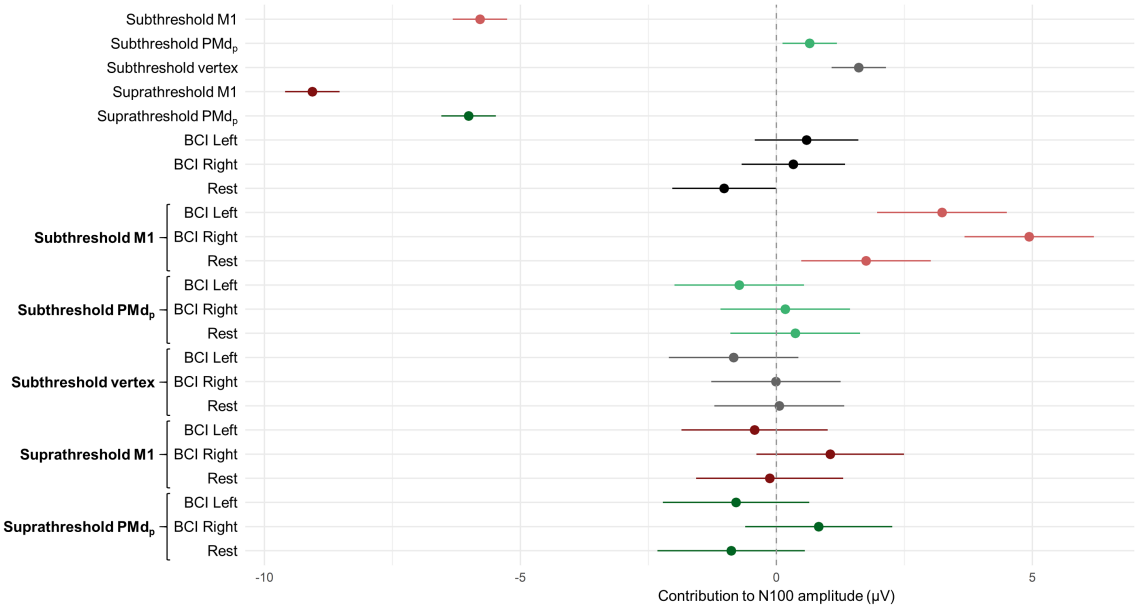

Figure 4.8: Linear mixed effects model coefficients for fitted N100 amplitudes at electrode C3 as a function of task and stimulation condition. *Bars indicate 95% confidence intervals. Values can be interpreted as modeled contributions to N100 amplitude relative to the suprathreshold vertex and non-BCI conditions.*

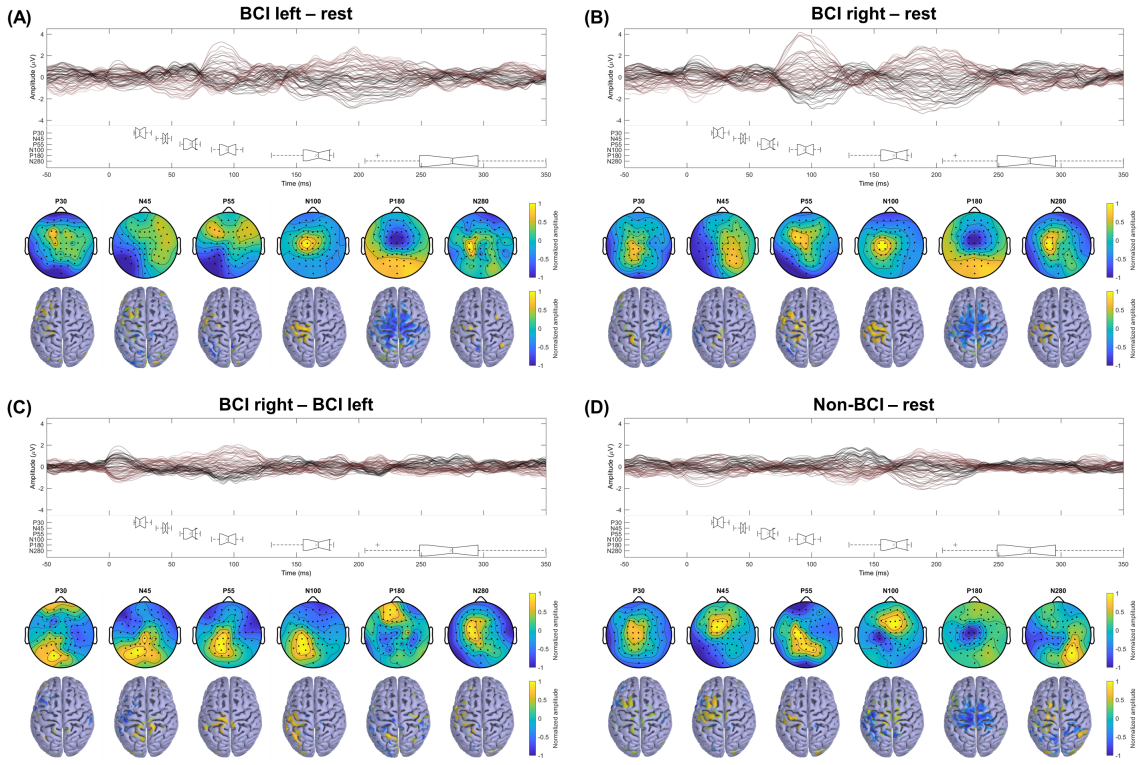

Figure 4.7: TEP differences between tasks for subthreshold stimulation to left M1. *Epochs were aggregated and subtracted within each session and condition, then averaged at the group level.*

4.3.2 Alpha phase dependency

Significant relationships between pre-stimulation phase and MEP amplitude were found, as shown in Figure 4.9. This figure shows phase sensitivity curves for 3 different phase estimation input features based on unweighted sensor values (conventional C3), spatially weighted sensor values (Laplacian C3), or source features (mean estimated source activity in a subject-specific ROI on the precentral gyrus for each subject). Several significant deviations outside of the null hypothesis bounds were observed for all bin sizes, indicating a significant relationship between pre-stimulation alpha phase and resulting MEP amplitudes for suprathreshold stimulation to left

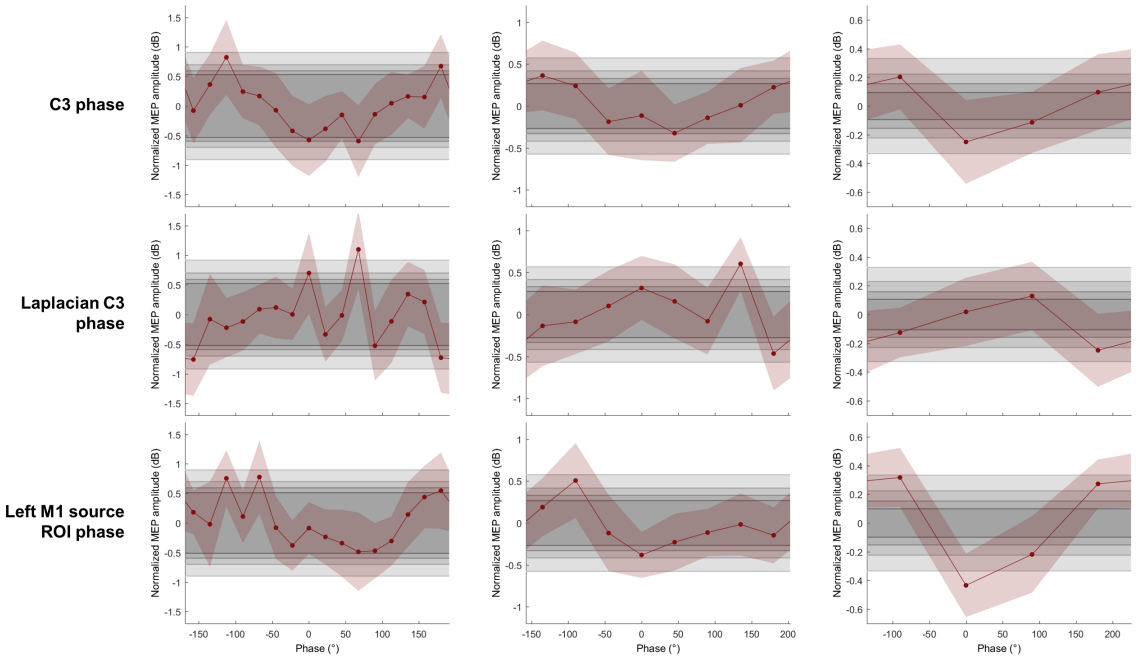

Figure 4.9: Phase sensitivity curves relating pre-stimulation phase to resulting MEP amplitude. *Per-trial estimates of phase at the time of stimulation were binned into 16 (left), 8 (middle), or 4 (right) bins and aggregated over sessions. Phase estimates were obtained based on 3 different signal features: an unweighted signal from electrode C3 (upper), a Laplacian spatial weighted signal centered at electrode C3 (middle), and a signal obtained by averaging estimated source activity within in a subject-specific ROI on the precentral gyrus for each subject (lower). Points indicate the median aggregated normalized MEP amplitudes within each phase bin, with red shaded areas around each point indicating an approximate 95% confidence interval on the median. Gray shaded regions indicate null hypothesis bounds that were not exceeded by 1,2,3, or 4 (for progressively smaller intervals) bin median values in 95% of the shuffled null data.*

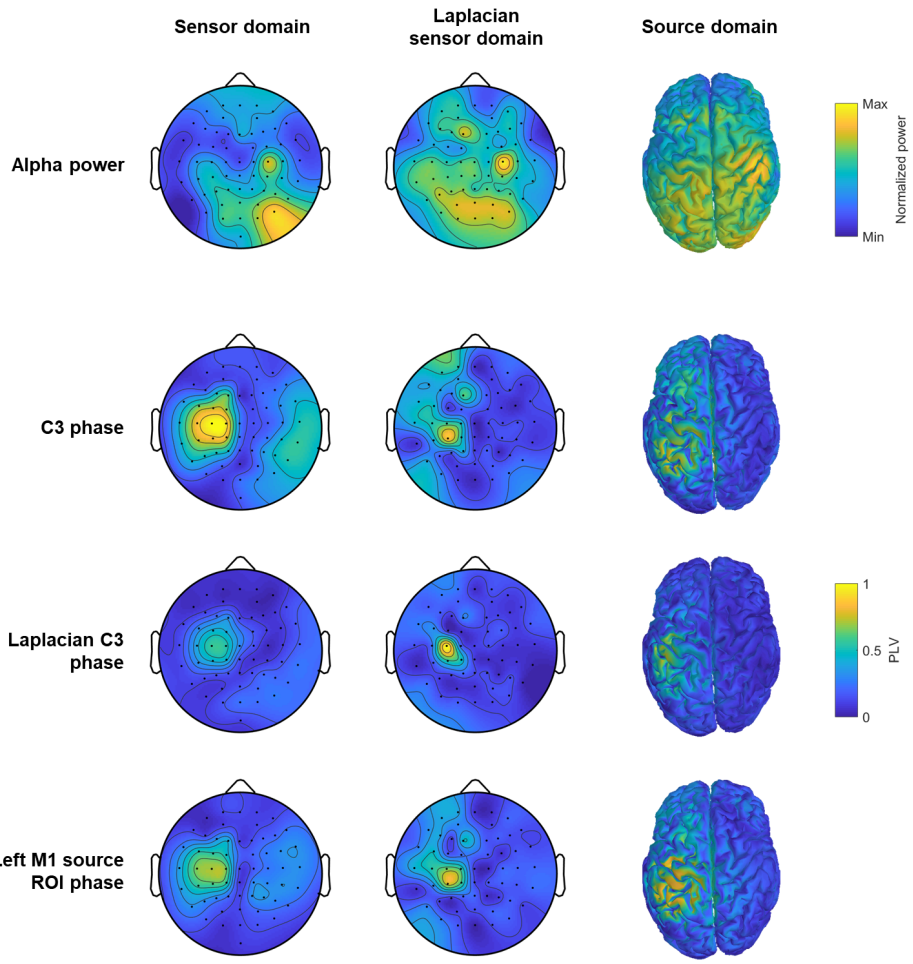

Figure 4.10: Alpha power and phase-locking values in a single subject. *Results shown are based on conventional sensor data, Laplacian-weighted data, and estimated source activity. Mean baseline alpha power is shown for each domain (upper), as well as phase-locking values across all channels / sources in the domain compared to seed phase estimates obtained from conventional C3, Laplacian weighted C3, and mean activity of a subject-specific source ROI located on the precentral gyrus.*

M1. Phase estimation with a control site not expected to be informative (electrode POz) did not produce any deviations outside of the null hypothesis bounds (not shown).

In comparing possible phase estimation features, it is helpful to examine the spatial extent of a given measured oscillation. The upper plots in Figure 4.10 show mean alpha band power during the pre-stimulation baseline time period in sensor, Laplacian sensor, and source spaces for a single example subject. These band powers reflect total oscillatory activity, possibly the sum of

multiple independent (i.e. incoherent) oscillators. To focus specifically on the coherent oscillation used for phase estimation here, we can quantify the coherence between a seed phase estimate and other phases using the phase-locking value (PLV) (Aydore et al., 2013; Lachaux et al., 1999), with a PLV of 0 indicating no phase coherence and a value of 1 indicating complete phase coherence (regardless of any constant phase offset). Using our primary phase estimates from electrode C3 and the left M1 ROI, the lower plots in Figure 4.10 show the spatial extent of the oscillatory components emphasized by each input feature, across domains. As expected, each seed shows the highest phase locking with the features in its own domain (e.g. conventional electrodes for C3 phase estimate, source dipoles for the source estimate). The Laplacian estimate shows lower PLVs for non-Laplacian features in the sensor and source domain, and a sharp drop-off in phase locking even for Laplacian channels with distance from C3, indicating either a highly localized oscillation measured with the Laplacian weights at C3, or that the estimate itself is noisy and not consistent when estimated at nearby similar points. Interestingly, the source ROI and conventional C3 seeds show a high phase locking value in the Laplacian sensor domain peaking in the region interpolated between electrodes C3 and CP3; this indicates a possible shift in “optimal” measurement location for this particular oscillation that is not completely captured by the single Laplacian weighted estimate centered at C3.

To move beyond dependence on the MEP outcome measure, it can be relevant to examine the TMS-evoked EEG response for phase sensitivity as well. Since pre-stimulation phase can affect post-stimulation time-locked TEPs even in the absence of any stimulation effect, it is important to control for this possible confound. Figure 4.11 shows group-averaged TEPs binned by estimated pre-stimulation phase for electrode C3. Clear phase-specific separation of traces can be observed leading up to the time of stimulation, due to the binning of epochs by phase within

this time period. After subtracting the average TEP response across all phase bins, the phase-specific effects can be seen in Figure 4.11B.

These phase-specific TEP components can also be viewed as multichannel topographies, as shown in Figure 4.12 for four of the eight phase bins. Examining topographies at peak time points in each phase-specific oscillatory component, clear inversion of topographies can be observed with 180° phase offsets, with the primary oscillation localized near electrode C3.

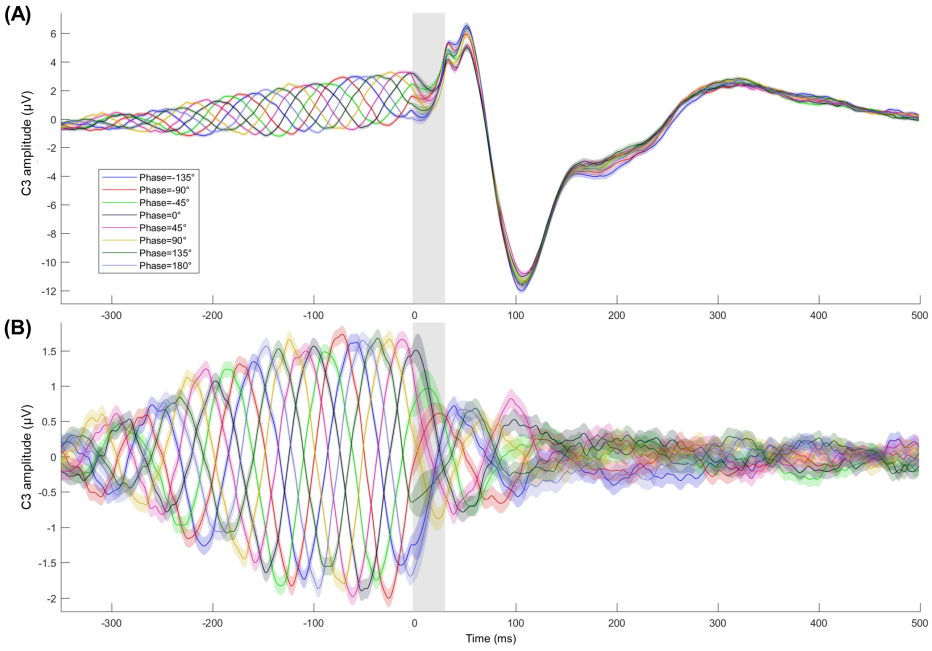

Figure 4.11: Group averaged C3 TEPs binned by pre-stimulation phase. *Epochs binned based on a left M1 source ROI in each session. TEPs are shown without (A) and with (B) the grand average subtracted within each session, such that (B) shows only phase-specific components of the signals not shared by all phase bins.*

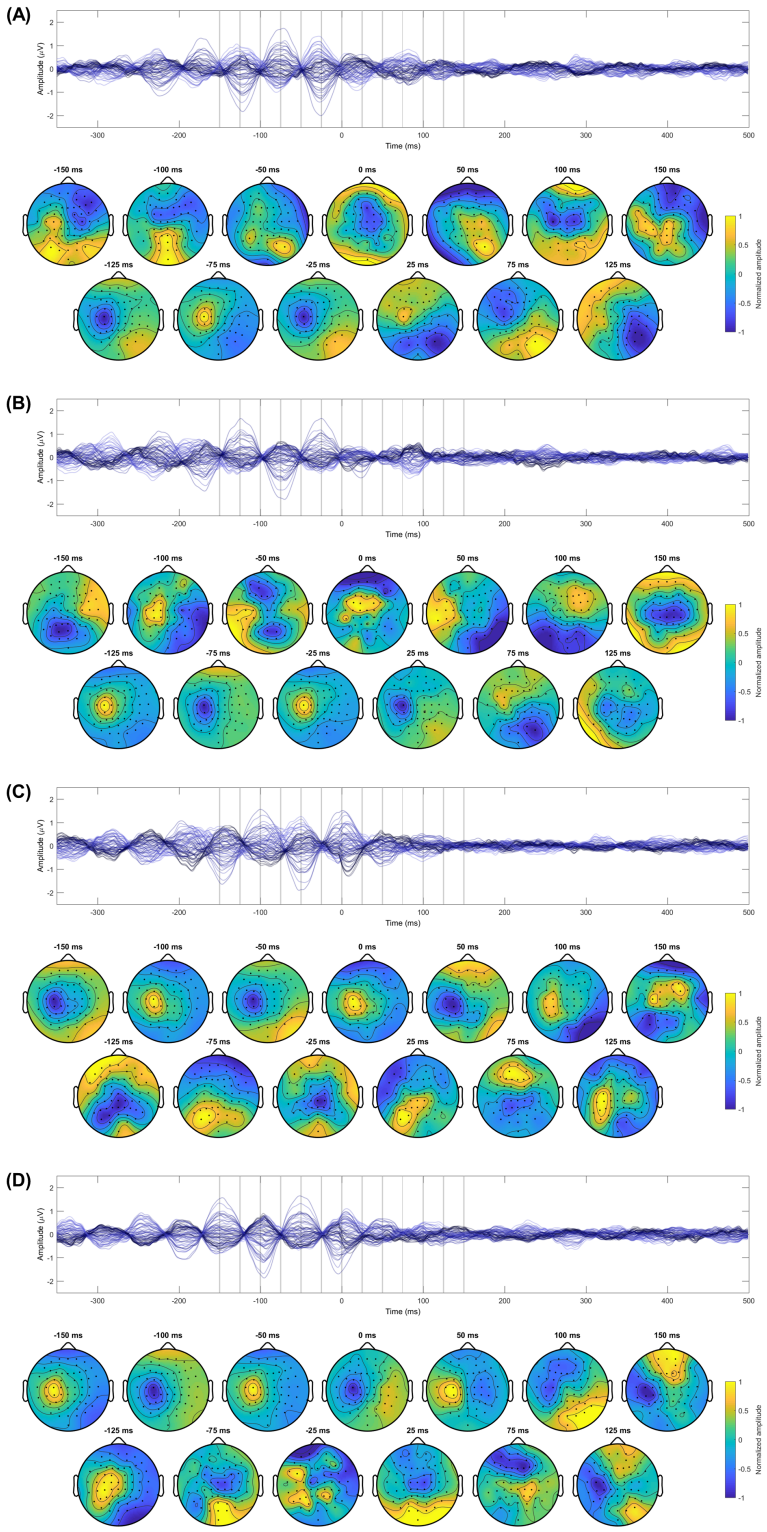

Figure 4.12: Subset of group averaged phase-specific TEPs after average phase-independent TEP subtraction. *Based on the same data as Figure 4.11, but shown for all electrodes and a subset of phases. (A,B,C,D) correspond to phase bins (-90°, 90°, 0°, 180°) respectively.*

4.4 Discussion

4.4.1 Motor task dependency

Some task-dependent effects of stimulation on MEP amplitude and TEP components were observed. For MEPs, the strongest task-dependent effects was seen for stimulation to the left PMd_p target, particularly a reduction in MEP amplitude when stimulating during left MI tasks compared to others. The presence of some MEPs for stimulation to this premotor cortex site likely reflects direct stimulation of the nearby primary motor cortex rather than some indirect activation via premotor activation; assuming this is the case, this condition actually provided data on pulses applied to M1 at an intermediate intensity near the RMT of each subject. It was at these near-RMT levels that the strongest task-dependent effects were observed, suggesting that the stronger pulses applied at 120% RMT were of sufficient intensity to mostly override any task-specific differences in excitability. Furthermore, the sign of the change, with a decrease in MEP amplitude during the BCI left task, indicates the presence of stronger inhibition of ipsilateral primary motor cortex (left hemisphere) during left motor imagery.

As shown by the linear mixed effect modeling results shown Figure 4.8, this is also corroborated by changes in the N100 component amplitudes. The N100 has been implicated in inhibitory processes and attention (Bender et al., 2005; Bonnard et al., 2009; Bruckmann et al., 2012; Chung et al., 2015; Kaarre et al., 2018; Kičić et al., 2008; Nikulin et al., 2003; Van Doren et al., 2015). Here, task-specific effects on N100 were observed particularly for subthreshold stimulation to left M1, with all pulses applied during the BCI task blocks generating more positive (generally weaker negative amplitude) N100 responses compared to those applied during longer non-BCI rest blocks. This could be attributed to differences in attentive state, with

even the “rest” trials during the BCI blocks involving a higher level of arousal than the extended period of several minutes of rest during the non-BCI blocks. The greatest task-specific effect on the N100 was seen during BCI right trials, supporting greatest decrease in inhibition at the stimulation site during tasks involving the same region.

4.4.2 Alpha phase dependency

The observation of significant relationships between pre-stimulation phase and resulting MEP amplitudes corroborates other recently reported work (Zrenner et al., 2018).

The presence of sharp changes in median MEP amplitudes between adjacent bins even for the narrowest bin size (22.5°) here indicate the possibility of relatively strong sensitivity to phase change, with differences in outcomes for only small difference in phase; this suggests that the accuracy of phase estimates may be important for maximizing the utility of phase-informed stimulation approaches. However, the largest bin size (90°) also showed significant deviations outside of the null hypothesis bounds, indicating that even crude phase estimates can be sufficiently informative to predict stimulation outcome.

Phase estimates based on features in each of three domains (conventional sensor, Laplacian sensor, and source space) were able to show significant phase-specific effects on MEP amplitude. At the coarsest binning level (90° bin width), the source imaging based features showed the most significant deviations outside of the null hypothesis bounds, suggesting the these source imaging features could more reliably estimate a phase predictive of stimulation outcome. However, further work is needed to confirm whether this finding holds across subjects and binning parameters.

4.4.3 Conclusion

The work presented here supports the claim that pre-stimulation state can affect stimulation outcome. This has implications for development of future EEG-informed stimulation approaches. One particular type of EEG-informed stimulation involves phase-dependent timing of administration of single pulses (or bursts of pulses) based on real-time estimation and prediction of phase (Zrenner et al., 2018). Our results provide evidence for the promise of this approach, and demonstrate several variants of input features for phase estimation and the scale of phase-specific effects with different binning parameters.

Future work will be needed to extend these findings for stimulation outside of the primary motor cortex. Although the main effects here were observed for phase sensitivity on MEP amplitude, other effects on TEP amplitudes or other features could be used to identify phase dependencies in stimulation of other brain regions. This could be critical for improving efficacy and reliability of stimulation for various clinical targets, including stimulation of prefrontal cortex sites.

Phase is just one possible relevant metric of brain state that could influence or predict response to stimulation. While acquisition of information matching the full complexity of the underlying true brain state is not feasible with EEG alone, various other possibly relevant features are available, such as fluctuations in band power and connectivity between brain regions. Unlike phase, which changes on the order of milliseconds for the frequencies of interest here, these other features may fluctuate over longer time scales, allowing more reliable estimation of subtle or noisy state variables by averaging over longer time periods.

The current state of approaches for neuromodulation clearly demand improved understanding of stimulation effects and tailoring of stimulation parameters to individuals for more effective interventions. EEG-informed TMS offers a variety of possible methods for addressing these needs, providing information to tailor when, where, and how stimulation is applied. From approaches looking at TMS-evoked potentials to quantify stimulation effect over longer time scales, to adjusting pulse-to-pulse stimulation parameters based on real-time state estimation, these EEG-informed TMS methods hold great promise for future improvements in clinical therapies and research interventions.

5 Bibliography

Abbruzzese, G., Trompetto, C., and Schieppati, M. (1996). The excitability of the human motor cortex increases during execution and mental imagination of sequential but not repetitive finger movements. Exp. Brain Res. *111*, 465–472.

Ahn, M., and Jun, S.C. (2015). Performance variation in motor imagery brain–computer interface: A brief review. J. Neurosci. Methods *243*, 103–110.

Ajiboye, A.B., Willett, F.R., Young, D.R., Memberg, W.D., Murphy, B.A., Miller, J.P., Walter, B.L., Sweet, J.A., Hoyen, H.A., Keith, M.W., et al. (2017). Restoration of reaching and grasping movements through brain-controlled muscle stimulation in a person with tetraplegia: a proof-of-concept demonstration. The Lancet *0*.

Alkadhi, H., Brugger, P., Boendermaker, S.H., Crelier, G., Curt, A., Hepp-Reymond, M.-C., and Kollias, S.S. (2005). What Disconnection Tells about Motor Imagery: Evidence from Paraplegic Patients. Cereb. Cortex *15*, 131–140.

Allison, B., Luth, T., Valbuena, D., Teymourian, A., Volosyak, I., and Graser, A. (2010). BCI Demographics: How Many (and What Kinds of) People Can Use an SSVEP BCI? IEEE Trans. Neural Syst. Rehabil. Eng. *18*, 107–116.

Amiez, C., Kostopoulos, P., Champod, A.-S., and Petrides, M. (2006). Local Morphology Predicts Functional Organization of the Dorsal Premotor Region in the Human Brain. J. Neurosci. *26*, 2724–2731.

Ang, K.K., Chua, K.S.G., Phua, K.S., Wang, C., Chin, Z.Y., Kuah, C.W.K., Low, W., and Guan, C. (2014). A Randomized Controlled Trial of EEG-Based Motor Imagery Brain-Computer Interface Robotic Rehabilitation for Stroke. Clin. EEG Neurosci. 1550059414522229.

Attene, M. (2010). A lightweight approach to repairing digitized polygon meshes. Vis. Comput. *26*, 1393–1406.

Aydore, S., Pantazis, D., and Leahy, R.M. (2013). A Note on the Phase Locking Value and its Properties. NeuroImage *74*, 231–244.

Barker, A.T., Jalinous, R., and Freeston, I.L. (1985). Non-invasive magnetic stimulation of human motor cortex. The Lancet *325*, 1106–1107.

Bates, D., Mächler, M., Bolker, B., and Walker, S. (2014). Fitting Linear Mixed-Effects Models using lme4. ArXiv14065823 Stat.

Bender, S., Basseler, K., Sebastian, I., Resch, F., Kammer, T., Oelkers-Ax, R., and Weisbrod, M. (2005). Electroencephalographic response to transcranial magnetic stimulation in children: Evidence for giant inhibitory potentials. Ann. Neurol. *58*, 58–67.

Berger, P.D.H. (1929). Über das Elektrenkephalogramm des Menschen. Arch. Für Psychiatr. Nervenkrankh. *87*, 527–570.

Bergmann, T.O., Mölle, M., Schmidt, M.A., Lindner, C., Marshall, L., Born, J., and Siebner, H.R. (2012). EEG-Guided Transcranial Magnetic Stimulation Reveals Rapid Shifts in Motor Cortical Excitability during the Human Sleep Slow Oscillation. J. Neurosci. *32*, 243–253.

Besl, P.J., and McKay, N.D. (1992). A Method for Registration of 3-D Shapes. IEEE Trans. Pattern Anal. Mach. Intell. *14*, 239–256.

Bestmann, S., Swayne, O., Blankenburg, F., Ruff, C.C., Haggard, P., Weiskopf, N., Josephs, O., Driver, J., Rothwell, J.C., and Ward, N.S. (2008). Dorsal premotor cortex exerts state-dependent causal influences on activity in contralateral primary motor and dorsal premotor cortex. Cereb. Cortex N. Y. N 1991 *18*, 1281–1291.

Bigdely-Shamlo, N., Mullen, T., Kothe, C., Su, K.-M., and Robbins, K.A. (2015). The PREP pipeline: standardized preprocessing for large-scale EEG analysis. Front. Neuroinformatics *9*, 16.

Birbaumer, N., Kubler, A., Ghanayim, N., Hinterberger, T., Perelmouter, J., Kaiser, J., Iversen, I., Kotchoubey, B., Neumann, N., and Flor, H. (2000). The thought translation device (TTD) for completely paralyzed patients. IEEE Trans. Rehabil. Eng. *8*, 190–193.

Blankertz, B., Tangermann, M., Vidaurre, C., Fazli, S., Sannelli, C., Haufe, S., Maeder, C., Ramsey, L., Sturm, I., Curio, G., et al. (2010a). The Berlin Brain-Computer Interface: Non-Medical Uses of BCI Technology. Front. Neurosci. *4*.

Blankertz, B., Sannelli, C., Halder, S., Hammer, E.M., Kübler, A., Müller, K.-R., Curio, G., and Dickhaus, T. (2010b). Neurophysiological predictor of SMR-based BCI performance. NeuroImage *51*, 1303–1309.

Bonato, C., Miniussi, C., and Rossini, P.M. (2006). Transcranial magnetic stimulation and cortical evoked potentials: A TMS/EEG co-registration study. Clin. Neurophysiol. *117*, 1699–1707.

Bonnard, M., Spieser, L., Meziane, H.B., De Graaf, J.B., and Pailhous, J. (2009). Prior intention can locally tune inhibitory processes in the primary motor cortex: direct evidence from combined TMS-EEG. Eur. J. Neurosci. *30*, 913–923.

Bonnard, M., Chen, S., Gaychet, J., Carrere, M., Woodman, M., Giusiano, B., and Jirsa, V. (2016). Resting state brain dynamics and its transients: a combined TMS-EEG study. Sci. Rep. *6*, 31220.

Braack, E.M. ter, Vos, C.C. de, and Putten, M.J.A.M. van (2013). Masking the Auditory Evoked Potential in TMS–EEG: A Comparison of Various Methods. Brain Topogr. *28*, 520–528.

Bradberry, T.J., Gentili, R.J., and Contreras-Vidal, J.L. (2010). Reconstructing Three-Dimensional Hand Movements from Noninvasive Electroencephalographic Signals. J. Neurosci. *30*, 3432–3437.

Bradberry, T.J., Gentili, R.J., and Contreras-Vidal, J.L. (2011). Fast attainment of computer cursor control with noninvasively acquired brain signals. J. Neural Eng. *8*, 036010.

Bruckmann, S., Hauk, D., Roessner, V., Resch, F., Freitag, C.M., Kammer, T., Ziemann, U., Rothenberger, A., Weisbrod, M., and Bender, S. (2012). Cortical inhibition in attention deficit hyperactivity disorder: new insights from the electroencephalographic response to transcranial magnetic stimulation. Brain aws071.

Bruns, C. (2017). pyopenvr: Python bindings for Valve's OpenVR virtual reality SDK.

Buch, E., Weber, C., Cohen, L.G., Braun, C., Dimyan, M.A., Ard, T., Mellinger, J., Caria, A., Soekadar, S., Fourkas, A., et al. (2008). Think to Move: a Neuromagnetic Brain-Computer Interface (BCI) System for Chronic Stroke. Stroke *39*, 910–917.

Burke, D., and Pierrot-Deseilligny, E. (2010). Caveats when studying motor cortex excitability and the cortical control of movement using transcranial magnetic stimulation. Clin. Neurophysiol. *121*, 121–123.

Buzsáki, G., Anastassiou, C.A., and Koch, C. (2012). The origin of extracellular fields and currents — EEG, ECoG, LFP and spikes. Nat. Rev. Neurosci. *13*, 407–420.

Casali, A.G., Casarotto, S., Rosanova, M., Mariotti, M., and Massimini, M. (2010). General indices to characterize the electrical response of the cerebral cortex to TMS. NeuroImage *49*, 1459–1468.

Casarotto, S., Lauro, L.J.R., Bellina, V., Casali, A.G., Rosanova, M., Pigorini, A., Defendi, S., Mariotti, M., and Massimini, M. (2010). EEG Responses to TMS Are Sensitive to Changes in the Perturbation Parameters and Repeatable over Time. PLOS ONE *5*, e10281.

Casula, E.P., Tarantino, V., Basso, D., Arcara, G., Marino, G., Toffolo, G.M., Rothwell, J.C., and Bisiacchi, P.S. (2014). Low-frequency rTMS inhibitory effects in the primary motor cortex: Insights from TMS-evoked potentials. NeuroImage *98*, 225–232.

Chaudhary, U., Xia, B., Silvoni, S., Cohen, L.G., and Birbaumer, N. (2017). Brain–Computer Interface–Based Communication in the Completely Locked-In State. PLOS Biol. *15*, e1002593.

Chen, S. (2018). psomatlab.

Chong, B.W.X., and Stinear, C.M. (2017). Modulation of motor cortex inhibition during motor imagery. J. Neurophysiol. jn.00549.2016.

Chung, S.W., Rogasch, N.C., Hoy, K.E., and Fitzgerald, P.B. (2015). Measuring Brain Stimulation Induced Changes in Cortical Properties Using TMS-EEG. Brain Stimulat. *8*, 1010–1020.

Cocchi, L., and Zalesky, A. (2018). Personalized transcranial magnetic stimulation in psychiatry. Biol. Psychiatry Cogn. Neurosci. Neuroimaging *0*.

Collinger, J.L., Wodlinger, B., Downey, J.E., Wang, W., Tyler-Kabara, E.C., Weber, D.J., McMorland, A.J., Velliste, M., Boninger, M.L., and Schwartz, A.B. (2013). High-performance neuroprosthetic control by an individual with tetraplegia. The Lancet *381*, 557–564.

Cona, G., Marino, G., and Semenza, C. (2017). TMS of supplementary motor area (SMA) facilitates mental rotation performance: Evidence for sequence processing in SMA. NeuroImage *146*, 770–777.

Conde, V., Akopian, I., Tomasevic, L., Stanek, K., Bergmann, T.O., and Siebner, H.R. (2017). P122 Contribution of integrated somatosensory and auditory inputs to the cortical response evoked by transcranial magnetic stimulation: A sham TMS-EEG study. Clin. Neurophysiol. *128*, e75–e76.

Cuypers, K., Thijs, H., and Meesen, R.L.J. (2014). Optimization of the Transcranial Magnetic Stimulation Protocol by Defining a Reliable Estimate for Corticospinal Excitability. PLOS ONE *9*, e86380.

Dalal, S.S., Rampp, S., Willomitzer, F., and Ettl, S. (2014). Consequences of EEG electrode position error on ultimate beamformer source reconstruction performance. Front. Neurosci. *8*.

Dale, A.M., Fischl, B., and Sereno, M.I. (1999). Cortical Surface-Based Analysis: I. Segmentation and Surface Reconstruction. NeuroImage *9*, 179–194.

De Munck, J.C., Vijn, P.C.M., and Spekreijse, H. (1991). A practical method for determining electrode positions on the head. Electroencephalogr. Clin. Neurophysiol. *78*, 85–87.

Decety, J., and Jeannerod, M. (1995). Mentally simulated movements in virtual reality: does Fitt's law hold in motor imagery? Behav. Brain Res. *72*, 127–134.

Decety, J., Jeannerod, M., and Prablanc, C. (1989). The timing of mentally represented actions. Behav. Brain Res. *34*, 35–42.

Deng, Z.-D., Lisanby, S.H., and Peterchev, A.V. (2013). Electric field depth-focality tradeoff in transcranial magnetic stimulation: Simulation comparison of 50 coil designs. Brain Stimulat. *6*, 1–13.

Donchin, E., Spencer, K.M., and Wijesinghe, R. (2000). The mental prosthesis: assessing the speed of a P300-based brain-computer interface. IEEE Trans. Rehabil. Eng. *8*, 174–179.

Du, X., Choa, F.-S., Summerfelt, A., Rowland, L.M., Chiappelli, J., Kochunov, P., and Hong, L.E. (2017). N100 as a generic cortical electrophysiological marker based on decomposition of TMS-evoked potentials across five anatomic locations. Exp. Brain Res. *235*, 69–81.

Dubin, M.J., Liston, C., Avissar, M.A., Ilieva, I., and Gunning, F.M. (2017). Network-Guided Transcranial Magnetic Stimulation for Depression. Curr. Behav. Neurosci. Rep. *4*, 70–77.

Dugué, L., Marque, P., and VanRullen, R. (2011). The Phase of Ongoing Oscillations Mediates the Causal Relation between Brain Excitation and Visual Perception. J. Neurosci. *31*, 11889–11893.

Edelman, B.J., Baxter, B., and He, B. (2016). EEG Source Imaging Enhances the Decoding of Complex Right-Hand Motor Imagery Tasks. IEEE Trans. Biomed. Eng. *63*, 4–14.

Esterman, M., Thai, M., Okabe, H., DeGutis, J., Saad, E., Laganiere, S.E., and Halko, M.A. (2017). Network-targeted cerebellar transcranial magnetic stimulation improves attentional control. NeuroImage *156*, 190–198.

Facchini, S., Muellbacher, W., Battaglia, F., Boroojerdi, B., and Hallett, M. (2002). Focal enhancement of motor cortex excitability during motor imagery: a transcranial magnetic stimulation study. Acta Neurol. Scand. *105*, 146–151.

Fadiga, L., Buccino, G., Craighero, L., Fogassi, L., Gallese, V., and Pavesi, G. (1998). Corticospinal excitability is specifically modulated by motor imagery: a magnetic stimulation study. Neuropsychologia *37*, 147–158.

Fang, Q., and Boas, D.A. (2009). Tetrahedral mesh generation from volumetric binary and grayscale images. In IEEE International Symposium on Biomedical Imaging: From Nano to Macro, 2009. ISBI '09, pp. 1142–1145.

Farwell, L.A., and Donchin, E. (1988). Talking off the top of your head: toward a mental prosthesis utilizing event-related brain potentials. Electroencephalogr. Clin. Neurophysiol. *70*, 510–523.

Ferreri, F., Pasqualetti, P., Määttä, S., Ponzo, D., Ferrarelli, F., Tononi, G., Mervaala, E., Miniussi, C., and Rossini, P.M. (2011). Human brain connectivity during single and paired pulse transcranial magnetic stimulation. NeuroImage *54*, 90–102.

Ferreri, F., Vecchio, F., Ponzo, D., Pasqualetti, P., and Rossini, P.M. (2014). Time-varying coupling of EEG oscillations predicts excitability fluctuations in the primary motor cortex as reflected by motor evoked potentials amplitude: An EEG-TMS study. Hum. Brain Mapp. *35*, 1969–1980.

Fischl, B. (2012). FreeSurfer. NeuroImage *62*, 774–781.

Fischl, B., Sereno, M.I., Tootell, R.B., Dale, A.M., and others (1999). High-resolution intersubject averaging and a coordinate system for the cortical surface. Hum. Brain Mapp. *8*, 272–284.

Fonov, V., Evans, A., McKinstry, R., Almli, C., and Collins, D. (2009). Unbiased nonlinear average age-appropriate brain templates from birth to adulthood. NeuroImage *47*, S102.

Fonov, V., Evans, A.C., Botteron, K., Almli, C.R., McKinstry, R.C., and Collins, D.L. (2011). Unbiased average age-appropriate atlases for pediatric studies. NeuroImage *54*, 313–327.

Friedrich, E.V.C., Neuper, C., and Scherer, R. (2013). Whatever Works: A Systematic User-Centered Training Protocol to Optimize Brain-Computer Interfacing Individually. PLoS ONE *8*, e76214.

Gangitano, M., Valero-Cabré, A., Tormos, J.M., Mottaghy, F.M., Romero, J.R., and Pascual-Leone, Á. (2002). Modulation of input–output curves by low and high frequency repetitive transcranial magnetic stimulation of the motor cortex. Clin. Neurophysiol. *113*, 1249–1257.

Gao, X., Xu, D., Cheng, M., and Gao, S. (2003). A BCI-based environmental controller for the motion-disabled. IEEE Trans. Neural Syst. Rehabil. Eng. *11*, 137–140.

George, M.S., Wassermann, E.M., Williams, W.A., Callahan, A., Ketter, T.A., Basser, P., Hallett, M., and Post, R.M. (1995). Daily repetitive transcranial magnetic stimulation (rTMS) improves mood in depression. Neuroreport *6*, 1853–1856.

George, M.S., Lisanby, S.H., Avery, D., McDonald, W.M., Durkalski, V., Pavlicova, M., Anderson, B., Nahas, Z., Bulow, P., Zarkowski, P., et al. (2010). Daily Left Prefrontal Transcranial Magnetic Stimulation Therapy for Major Depressive Disorder: A Sham-Controlled Randomized Trial. Arch. Gen. Psychiatry *67*, 507–516.

Gerardin, E., Sirigu, A., Lehéricy, S., Poline, J.-B., Gaymard, B., Marsault, C., Agid, Y., and Bihan, D.L. (2000). Partially Overlapping Neural Networks for Real and Imagined Hand Movements. Cereb. Cortex *10*, 1093–1104.

Gerschlager, W., Siebner, H.R., and Rothwell, J.C. (2001). Decreased corticospinal excitability after subthreshold 1 Hz rTMS over lateral premotor cortex. Neurology *57*, 449–455.

Goetz, S.M., Luber, B., Lisanby, S.H., and Peterchev, A.V. (2014). A Novel Model Incorporating Two Variability Sources for Describing Motor Evoked Potentials. Brain Stimulat. *7*, 541–552.

Goetz, S.M., Luber, B., Lisanby, S.H., Murphy, D.L.K., Kozyrkov, I.C., Grill, W.M., and Peterchev, A.V. (2016). Enhancement of Neuromodulation with Novel Pulse Shapes Generated by Controllable Pulse Parameter Transcranial Magnetic Stimulation. Brain Stimulat. *9*, 39–47.

Gramfort, A., Papadopoulo, T., Olivi, E., and Clerc, M. (2010). OpenMEEG: opensource software for quasistatic bioelectromagnetics. Biomed. Eng. OnLine *9*, 45.

Gramfort, A., Luessi, M., Larson, E., Engemann, D.A., Strohmeier, D., Brodbeck, C., Parkkonen, L., and Hämäläinen, M.S. (2014). MNE software for processing MEG and EEG data. NeuroImage *86*, 446–460.

Grosse-Wentrup, M., and Schölkopf, B. (2013). A Review of Performance Variations in SMR-Based Brain−Computer Interfaces (BCIs). In Brain-Computer Interface Research, C. Guger, B.Z. Allison, and G. Edlinger, eds. (Springer Berlin Heidelberg), pp. 39–51.

Guillot, A., Collet, C., Nguyen, V.A., Malouin, F., Richards, C., and Doyon, J. (2009). Brain activity during visual versus kinesthetic imagery: An fMRI study. Hum. Brain Mapp. *30*, 2157–2172.

Halder, S., Agorastos, D., Veit, R., Hammer, E.M., Lee, S., Varkuti, B., Bogdan, M., Rosenstiel, W., Birbaumer, N., and Kübler, A. (2011). Neural mechanisms of brain–computer interface control. NeuroImage *55*, 1779–1790.

Hammer, E.M., Halder, S., Blankertz, B., Sannelli, C., Dickhaus, T., Kleih, S., Müller, K.-R., and Kübler, A. (2012). Psychological predictors of SMR-BCI performance. Biol. Psychol. *89*, 80–86.

Han, B.H., Chun, I.K., Lee, S.C., and Lee, S.Y. (2004). Multichannel magnetic stimulation system design considering mutual couplings among the stimulation coils. IEEE Trans. Biomed. Eng. *51*, 812–817.

Hanakawa, T. (2011). Rostral premotor cortex as a gateway between motor and cognitive networks. Neurosci. Res. *70*, 144–154.

Hardwick, R.M., Rottschy, C., Miall, R.C., and Eickhoff, S.B. (2013). A quantitative meta-analysis and review of motor learning in the human brain. NeuroImage *67*, 283–297.

Hartwigsen, G., Bestmann, S., Ward, N.S., Woerbel, S., Mastroeni, C., Granert, O., and Siebner, H.R. (2012). Left Dorsal Premotor Cortex and Supramarginal Gyrus Complement Each Other during Rapid Action Reprogramming. J. Neurosci. *32*, 16162–16171.

Hashimoto, R., and Rothwell, J.C. (1999). Dynamic changes in corticospinal excitability during motor imagery. Exp. Brain Res. *125*, 75–81.

He, P., and Estepp, J.R. (2013). A practical method for quickly determining electrode positions in high-density EEG studies. Neurosci. Lett. *541*, 73–76.

He, B., Musha, T., Okamoto, Y., Homma, S., Nakajima, Y., and Sato, T. (1987). Electric Dipole Tracing in the Brain By Means of the Boundary Element Method and Its Accuracy. IEEE Trans. Biomed. Eng. *BME-34*, 406–414.

He, B., Yang, L., Wilke, C., and Yuan, H. (2011). Electrophysiological imaging of brain activity and connectivity-challenges and opportunities. IEEE Trans. Biomed. Eng. *58*, 1918–1931.

He, B., Gao, S., Yuan, H., and Wolpaw, J.R. (2013). Brain–Computer Interfaces. In Neural Engineering, B. He, ed. (Boston, MA: Springer US), pp. 87–151.

He, B., Baxter, B., Edelman, B.J., Cline, C.C., and Ye, W.W. (2015). Noninvasive Brain-Computer Interfaces Based on Sensorimotor Rhythms. Proc. IEEE *103*, 907–925.

Heller, L., and van Hulsteyn, D.B. (1992). Brain stimulation using electromagnetic sources: theoretical aspects. Biophys. J. *63*, 129–138.

Herring, J.D., Thut, G., Jensen, O., and Bergmann, T.O. (2015). Attention Modulates TMS-Locked Alpha Oscillations in the Visual Cortex. J. Neurosci. *35*, 14435–14447.

Herwig, U., Schönfeldt-Lecuona, C., Wunderlich, A.P., von Tiesenhausen, C., Thielscher, A., Walter, H., and Spitzer, M. (2001). The navigation of transcranial magnetic stimulation. Psychiatry Res. Neuroimaging *108*, 123–131.

Hétu, S., Grégoire, M., Saimpont, A., Coll, M.-P., Eugène, F., Michon, P.-E., and Jackson, P.L. (2013). The neural network of motor imagery: An ALE meta-analysis. Neurosci. Biobehav. Rev. *37*, 930–949.

Hill, N.J., Häuser, A.-K., and Schalk, G. (2014). A general method for assessing brain-computer interface performance and its limitations. J. Neural Eng. *11*, 026018.

Hinder, M.R., Goss, E.L., Fujiyama, H., Canty, A.J., Garry, M.I., Rodger, J., and Summers, J.J. (2014). Inter- and Intra-individual Variability Following Intermittent Theta Burst Stimulation: Implications for Rehabilitation and Recovery. Brain Stimulat. *7*, 365–371.

Hochberg, L.R., Serruya, M.D., Friehs, G.M., Mukand, J.A., Saleh, M., Caplan, A.H., Branner, A., Chen, D., Penn, R.D., and Donoghue, J.P. (2006). Neuronal ensemble control of prosthetic devices by a human with tetraplegia. Nature *442*, 164–171.

Hochberg, L.R., Bacher, D., Jarosiewicz, B., Masse, N.Y., Simeral, J.D., Vogel, J., Haddadin, S., Liu, J., Cash, S.S., van der Smagt, P., et al. (2012). Reach and grasp by people with tetraplegia using a neurally controlled robotic arm. Nature *485*, 372–375.

Hotson, G., McMullen, D.P., Fifer, M.S., Johannes, M.S., Katyal, K.D., Para, M.P., Armiger, R., Anderson, W.S., Thakor, N.V., Wester, B.A., et al. (2016). Individual finger control of a modular prosthetic limb using high-density electrocorticography in a human subject. J. Neural Eng. *13*, 026017.

Inan, U.S., and Inan, A.S. (1998). Engineering Electromagnetics (Addison Wesley Longman, Inc).

Janssen, A.M., Oostendorp, T.F., and Stegeman, D.F. (2015). The coil orientation dependency of the electric field induced by TMS for M1 and other brain areas. J. NeuroEngineering Rehabil. *12*, 1–13.

Jarosiewicz, B., Sarma, A.A., Bacher, D., Masse, N.Y., Simeral, J.D., Sorice, B., Oakley, E.M., Blabe, C., Pandarinath, C., Gilja, V., et al. (2015). Virtual typing by people with tetraplegia using a self-calibrating intracortical brain-computer interface. Sci. Transl. Med. *7*, 313ra179-313ra179.

Jeannerod, M. (1995). Mental imagery in the motor context. Neuropsychologia *33*, 1419–1432.

Jeannerod, M., and Frak, V. (1999). Mental imaging of motor activity in humans. Curr. Opin. Neurobiol. *9*, 735–739.

Jenkinson, M., Pechaud, M., and Smith, S. (2005). BET2: MR-based estimation of brain, skull and scalp surfaces. In Eleventh Annual Meeting of the Organization for Human Brain Mapping, p.

Johnson, J.S., Kundu, B., Casali, A.G., and Postle, B.R. (2012). Task-dependent changes in cortical excitability and effective connectivity: a combined TMS-EEG study. J. Neurophysiol. *107*, 2383–2392.

Johnson, N.N., Carey, J., Edelman, B., Doud, A., Grande, A., Lakshminarayan, K., and He, B. (2017). Combined rTMS and virtual reality brain-computer interface training for motor recovery after stroke. J. Neural Eng.

Jung, N.H., Delvendahl, I., Kuhnke, N.G., Hauschke, D., Stolle, S., and Mall, V. (2010). Navigated transcranial magnetic stimulation does not decrease the variability of motor-evoked potentials. Brain Stimulat. *3*, 87–94.

Kaarre, O., Äikiä, M., Kallioniemi, E., Könönen, M., Kekkonen, V., Heikkinen, N., Kivimäki, P., Tolmunen, T., Määttä, S., and Laukkanen, E. (2018). Association of the N100 TMS-evoked potential with attentional processes: A motor cortex TMS–EEG study. Brain Cogn. *122*, 9–16.

Kasahara, K., DaSalla, C.S., Honda, M., and Hanakawa, T. (2015). Neuroanatomical correlates of brain–computer interface performance. NeuroImage *110*, 95–100.

Kasess, C.H., Windischberger, C., Cunnington, R., Lanzenberger, R., Pezawas, L., and Moser, E. (2008). The suppressive influence of SMA on M1 in motor imagery revealed by fMRI and dynamic causal modeling. NeuroImage *40*, 828–837.

Kennedy, J.F., Kennedy, J., Eberhart, R.C., and Shi, Y. (2001). Swarm Intelligence (Morgan Kaufmann).

Kerwin, L.J., Keller, C.J., Wu, W., Narayan, M., and Etkin, A. (2017). Test-retest reliability of transcranial magnetic stimulation EEG evoked potentials. Brain Stimul. Basic Transl. Clin. Res. Neuromodulation *0*.

Kičić, D., Lioumis, P., Ilmoniemi, R.J., and Nikulin, V.V. (2008). Bilateral changes in excitability of sensorimotor cortices during unilateral movement: Combined electroencephalographic and transcranial magnetic stimulation study. Neuroscience *152*, 1119–1129.

Koessler, L., Maillard, L., Benhadid, A., Vignal, J.-P., Braun, M., and Vespignani, H. (2007). Spatial localization of EEG electrodes. Neurophysiol. Clin. Neurophysiol. *37*, 97–102.

Koessler, L., Cecchin, T., Caspary, O., Benhadid, A., Vespignani, H., and Maillard, L. (2011). EEG–MRI Co-registration and Sensor Labeling Using a 3D Laser Scanner. Ann. Biomed. Eng. *39*, 983–995.

Komssi, S., and Kähkönen, S. (2006). The novelty value of the combined use of electroencephalography and transcranial magnetic stimulation for neuroscience research. Brain Res. Rev. *52*, 183–192.

Komssi, S., Kähkönen, S., and Ilmoniemi, R.J. (2004). The effect of stimulus intensity on brain responses evoked by transcranial magnetic stimulation. Hum. Brain Mapp. *21*, 154–164.

Kraeutner, S.N., Keeler, L.T., and Boe, S.G. (2015). Motor imagery-based skill acquisition disrupted following rTMS of the inferior parietal lobule. Exp. Brain Res.

Kraus, D., Naros, G., Bauer, R., Khademi, F., Leão, M.T., Ziemann, U., and Gharabaghi, A. (2016). Brain State-Dependent Transcranial Magnetic Closed-Loop Stimulation Controlled by Sensorimotor Desynchronization Induces Robust Increase of Corticospinal Excitability. Brain Stimulat. *9*, 415–424.

Kübler, A., Neumann, N., Kaiser, J., Kotchoubey, B., Hinterberger, T., and Birbaumer, N.P. (2001). Brain-computer communication: Self-regulation of slow cortical potentials for verbal communication. Arch. Phys. Med. Rehabil. *82*, 1533–1539.

Kybic, J., Clerc, M., Abboud, T., Faugeras, O., Keriven, R., and Papadopoulo, T. (2005). A common formalism for the Integral formulations of the forward EEG problem. IEEE Trans. Med. Imaging *24*, 12–28.

Lachaux, J., Rodriguez Eugenio, Martinerie Jacques, and Varela Francisco J. (1999). Measuring phase synchrony in brain signals. Hum. Brain Mapp. *8*, 194–208.

LaFleur, K., Cassady, K., Doud, A., Shades, K., Rogin, E., and He, B. (2013). Quadcopter control in three-dimensional space using a noninvasive motor imagery-based brain–computer interface. J. Neural Eng. *10*, 046003.

Le, J., Lu, M., Pellouchoud, E., and Gevins, A. (1998). A rapid method for determining standard 10/10 electrode positions for high resolution EEG studies. Electroencephalogr. Clin. Neurophysiol. *106*, 554–558.

Lécuyer, A., Lotte, F., Reilly, R.B., Leeb, R., Hirose, M., Slater, M., and others (2008). Brain-computer interfaces, virtual reality, and videogames. IEEE Comput. *41*, 66–72.

Lee, P.-L., Sie, J.-J., Liu, Y.-J., Wu, C.-H., Lee, M.-H., Shu, C.-H., Li, P.-H., Sun, C.-W., and Shyu, K.-K. (2010). An SSVEP-Actuated Brain Computer Interface Using Phase-Tagged Flickering Sequences: A Cursor System. Ann. Biomed. Eng. *38*, 2383–2397.

Leeb, R., Lancelle, M., Kaiser, V., Fellner, D.W., and Pfurtscheller, G. (2013). Thinking Penguin: Multimodal Brain-Computer Interface Control of a VR Game. IEEE Trans. Comput. Intell. AI Games *5*, 117–128.

Lefaucheur, J.-P., André-Obadia, N., Antal, A., Ayache, S.S., Baeken, C., Benninger, D.H., Cantello, R.M., Cincotta, M., de Carvalho, M., De Ridder, D., et al. (2014). Evidence-based guidelines on the therapeutic use of repetitive transcranial magnetic stimulation (rTMS). Clin. Neurophysiol. *125*, 2150–2206.

Lepage, K.Q., Kramer, M.A., and Eden, U.T. (2013). Some Sampling Properties of Common Phase Estimators. Neural Comput. *25*, 901–921.

Lepping, P., Schönfeldt-Lecuona, C., Sambhi, R.S., Lanka, S.V.N., Lane, S., Whittington, R., Leucht, S., and Poole, R. (2014). A systematic review of the clinical relevance of repetitive transcranial magnetic stimulation. Acta Psychiatr. Scand. *130*, 326–341.

Lim, C.G., Lee, T.S., Guan, C., Fung, D.S.S., Zhao, Y., Teng, S.S.W., Zhang, H., and Krishnan, K.R.R. (2012). A Brain-Computer Interface Based Attention Training Program for Treating Attention Deficit Hyperactivity Disorder. PLOS ONE *7*, e46692.

Lioumis, P., Kičić, D., Savolainen, P., Mäkelä, J.P., and Kähkönen, S. (2009). Reproducibility of TMS—Evoked EEG responses. Hum. Brain Mapp. *30*, 1387–1396.

Lopes da Silva, F. (2013). EEG and MEG: Relevance to Neuroscience. Neuron *80*, 1112–1128.

López-Alonso, V., Cheeran, B., Río-Rodríguez, D., and Fernández-del-Olmo, M. (2014). Inter-individual Variability in Response to Non-invasive Brain Stimulation Paradigms. Brain Stimulat. *7*, 372–380.

Lorey, B., Pilgramm, S., Bischoff, M., Stark, R., Vaitl, D., Kindermann, S., Munzert, J., and Zentgraf, K. (2011). Activation of the Parieto-Premotor Network Is Associated with Vivid Motor Imagery—A Parametric fMRI Study. PLoS ONE *6*, e20368.

Lotte, F., Larrue, F., and Mühl, C. (2013a). Flaws in current human training protocols for spontaneous Brain-Computer Interfaces: lessons learned from instructional design. Front. Hum. Neurosci. *7*.

Lotte, F., Faller, J., Guger, C., Renard, Y., Pfurtscheller, G., Lécuyer, A., Leeb, R., Allison, B.Z., Dunne, S., Leeb, R., et al. (2013b). Combining BCI with Virtual Reality: Towards New Applications and Improved BCI. In Towards Practical Brain-Computer Interfaces, (Springer Berlin Heidelberg), pp. 197–220.

Lu, M.-K., Arai, N., Tsai, C.-H., and Ziemann, U. (2012). Movement related cortical potentials of cued versus self-initiated movements: Double dissociated modulation by dorsal premotor cortex versus supplementary motor area rTMS. Hum. Brain Mapp. *33*, 824–839.

Luber, B.M., Davis, S., Bernhardt, E., Neacsiu, A., Kwapil, L., Lisanby, S.H., and Strauman, T.J. (2017). Using neuroimaging to individualize TMS treatment for depression: Toward a new paradigm for imaging-guided intervention. NeuroImage *148*, 1–7.

Lule, D., Noirhomme, Q., Kleih, S.C., Chatelle, C., Halder, S., Demertzi, A., Bruno, M.-A., Gosseries, O., Vanhaudenhuyse, A., Schnakers, C., et al. (2013). Probing command following in patients with disorders of consciousness using a brain–computer interface. Clin. Neurophysiol. *124*, 101–106.

Maeda, F., Keenan, J.P., Tormos, J.M., Topka, H., and Pascual-Leone, A. (2000). Interindividual variability of the modulatory effects of repetitive transcranial magnetic stimulation on cortical excitability. Exp. Brain Res. *133*, 425–430.

Mahjoory, K., Nikulin, V.V., Botrel, L., Linkenkaer-Hansen, K., Fato, M.M., and Haufe, S. (2017). Consistency of EEG source localization and connectivity estimates. NeuroImage *152*, 590–601.

Mäki, H., and Ilmoniemi, R.J. (2010). The relationship between peripheral and early cortical activation induced by transcranial magnetic stimulation. Neurosci. Lett. *478*, 24–28.

Massimini, M., Ferrarelli, F., Esser, S.K., Riedner, B.A., Huber, R., Murphy, M., Peterson, M.J., and Tononi, G. (2007). Triggering sleep slow waves by transcranial magnetic stimulation. Proc. Natl. Acad. Sci. *104*, 8496–8501.

Meng, J., Zhang, S., Bekyo, A., Olsoe, J., Baxter, B., and He, B. (2016). Noninvasive Electroencephalogram Based Control of a Robotic Arm for Reach and Grasp Tasks. Sci. Rep. *6*, 38565.

Michel, C.M., Murray, M.M., Lantz, G., Gonzalez, S., Spinelli, L., and Grave de Peralta, R. (2004). EEG source imaging. Clin. Neurophysiol. *115*, 2195–2222.

Middendorf, M., McMillan, G., Calhoun, G., Jones, K.S., and others (2000). Brain-computer interfaces based on the steady-state visual-evoked response. IEEE Trans. Rehabil. Eng. *8*, 211–214.

Mikki, S.M., and Kishk, A.A. (2008). Particle Swarm Optimization: A Physics-Based Approach. Synth. Lect. Comput. Electromagn. *3*, 1–103.

Mochizuki, H., Huang, Y.-Z., and Rothwell, J.C. (2004). Interhemispheric interaction between human dorsal premotor and contralateral primary motor cortex. J. Physiol. *561*, 331–338.

Müller-Dahlhaus, J.F.M., Orekhov, Y., Liu, Y., and Ziemann, U. (2008). Interindividual variability and age-dependency of motor cortical plasticity induced by paired associative stimulation. Exp. Brain Res. *187*, 467–475.

Münchau, A., Bloem, B.R., Irlbacher, K., Trimble, M.R., and Rothwell, J.C. (2002). Functional connectivity of human premotor and motor cortex explored with repetitive transcranial magnetic stimulation. J. Neurosci. *22*, 554–561.

Mutanen, T., Mäki, H., and Ilmoniemi, R.J. (2013). The Effect of Stimulus Parameters on TMS–EEG Muscle Artifacts. Brain Stimulat. *6*, 371–376.

Nettekoven, C., Volz, L.J., Leimbach, M., Pool, E.-M., Rehme, A.K., Eickhoff, S.B., Fink, G.R., and Grefkes, C. (2015). Inter-individual variability in cortical excitability and motor network connectivity following multiple blocks of rTMS. NeuroImage *118*, 209–218.

Neuper, C., and Pfurtscheller, G. (2010). Neurofeedback Training for BCI Control. 65–78.

Neuper, C., Scherer, R., Reiner, M., and Pfurtscheller, G. (2005). Imagery of motor actions: Differential effects of kinesthetic and visual–motor mode of imagery in single-trial EEG. Cogn. Brain Res. *25*, 668–677.

Ngomo, S., Leonard, G., Moffet, H., and Mercier, C. (2012). Comparison of transcranial magnetic stimulation measures obtained at rest and under active conditions and their reliability. J. Neurosci. Methods *205*, 65–71.

Nicolo, P., Ptak, R., and Guggisberg, A.G. (2015). Variability of behavioural responses to transcranial magnetic stimulation: Origins and predictors. Neuropsychologia.

Nielsen, J.F. (1996). Logarithmic Distribution of Amplitudes of Compound Muscle Action Potentials Evoked by Transcranial Magnetic Stimulation. J. Clin. Neurophysiol. *13*, 423.

Nikulin, V.V., Kičić, D., Kähkönen, S., and Ilmoniemi, R.J. (2003). Modulation of electroencephalographic responses to transcranial magnetic stimulation: evidence for changes in cortical excitability related to movement. Eur. J. Neurosci. *18*, 1206–1212.

Noirhomme, Q., Brecheisen, R., Lesenfants, D., Antonopoulos, G., and Laureys, S. (2017). "Look at my classifier's result": Disentangling unresponsive from (minimally) conscious patients. NeuroImage *145*, *Part B*, 288–303.

Ono, T., Kimura, A., and Ushiba, J. (2013). Daily training with realistic visual feedback improves reproducibility of event-related desynchronisation following hand motor imagery. Clin. Neurophysiol. *124*, 1779–1786.

Opie, G.M., Rogasch, N.C., Goldsworthy, M.R., Ridding, M.C., and Semmler, J.G. (2017). Investigating TMS–EEG Indices of Long-Interval Intracortical Inhibition at Different Interstimulus Intervals. Brain Stimulat. *10*, 65–74.

Opitz, A., Fox, M.D., Craddock, R.C., Colcombe, S., and Milham, M.P. (2016). An integrated framework for targeting functional networks via transcranial magnetic stimulation. NeuroImage *127*, 86–96.

O'Reardon, J.P., Solvason, H.B., Janicak, P.G., Sampson, S., Isenberg, K.E., Nahas, Z., McDonald, W.M., Avery, D., Fitzgerald, P.B., Loo, C., et al. (2007). Efficacy and Safety of Transcranial Magnetic Stimulation in the Acute Treatment of Major Depression: A Multisite Randomized Controlled Trial. Biol. Psychiatry *62*, 1208–1216.

O'Shea, J., Johansen-Berg, H., Trief, D., Göbel, S., and Rushworth, M.F.S. (2007). Functionally Specific Reorganization in Human Premotor Cortex. Neuron *54*, 479–490.

Parmigiani, S., Barchiesi, G., and Cattaneo, L. (2015). The dorsal premotor cortex exerts a powerful and specific inhibitory effect on the ipsilateral corticofacial system: a dual-coil transcranial magnetic stimulation study. Exp. Brain Res. 1–8.

Pascual-Leone, A., Gates, J.R., and Dhuna, A. (1991). Induction of speech arrest and counting errors with rapid-rate transcranial magnetic stimulation. Neurology *41*, 697–702.

Pascual-Leone, A., Rubio, B., Pallardó, F., and Catalá, M.D. (1996). Rapid-rate transcranial magnetic stimulation of left dorsolateral prefrontal cortex in drug-resistant depression. The Lancet *348*, 233–237.

Pascual-Marqui, R.D., Michel, C.M., and Lehmann, D. (1994). Low resolution electromagnetic tomography: a new method for localizing electrical activity in the brain. Int. J. Psychophysiol. *18*, 49–65.

Pasley, B.N., Allen, E.A., and Freeman, R.D. (2009). State-Dependent Variability of Neuronal Responses to Transcranial Magnetic Stimulation of the Visual Cortex. Neuron *62*, 291–303.

Paus, T., Sipila, P.K., and Strafella, A.P. (2001). Synchronization of Neuronal Activity in the Human Primary Motor Cortex by Transcranial Magnetic Stimulation: An EEG Study. J. Neurophysiol. *86*, 1983–1990.

Pelgrims, B., Andres, M., and Olivier, E. (2009). Double Dissociation between Motor and Visual Imagery in the Posterior Parietal Cortex. Cereb. Cortex *19*, 2298–2307.

Pelgrims, B., Michaux, N., Olivier, E., and Andres, M. (2011). Contribution of the primary motor cortex to motor imagery: A subthreshold TMS study. Hum. Brain Mapp. *32*, 1471–1482.

Perez, R.E., and Behdinan, K. (2007). Particle Swarm Approach for Structural Design Optimization. Comput Struct *85*, 1579–1588.

Perini, F., Cattaneo, L., Carrasco, M., and Schwarzbach, J.V. (2012). Occipital Transcranial Magnetic Stimulation Has an Activity-Dependent Suppressive Effect. J. Neurosci. *32*, 12361–12365.

Petrichella, S., Johnson, N., and He, B. (2017). The influence of corticospinal activity on TMS-evoked activity and connectivity in healthy subjects: A TMS-EEG study. PLOS ONE *12*, e0174879.

Pfurtscheller, G., and Neuper, C. (1997). Motor imagery activates primary sensorimotor area in humans. Neurosci. Lett. *239*, 65–68.

Picard, N., and Strick, P.L. (2001). Imaging the premotor areas. Curr. Opin. Neurobiol. *11*, 663–672.

Premoli, I., Castellanos, N., Rivolta, D., Belardinelli, P., Bajo, R., Zipser, C., Espenhahn, S., Heidegger, T., Müller-Dahlhaus, F., and Ziemann, U. (2014a). TMS-EEG Signatures of GABAergic Neurotransmission in the Human Cortex. J. Neurosci. *34*, 5603–5612.

Premoli, I., Rivolta, D., Espenhahn, S., Castellanos, N., Belardinelli, P., Ziemann, U., and Müller-Dahlhaus, F. (2014b). Characterization of GABAB-receptor mediated neurotransmission in the human cortex by paired-pulse TMS–EEG. NeuroImage *103*, 152–162.

Ramos-Murguialday, A., Broetz, D., Rea, M., Läer, L., Yilmaz, Ö., Brasil, F.L., Liberati, G., Curado, M.R., Garcia Cossio, E., Vyziotis, A., et al. (2013). Brain–machine interface in chronic stroke rehabilitation: A controlled study. Ann. Neurol. *74*, 100–108.

Reis, P.M.R., and Lochmann, M. (2015). Using a motion capture system for spatial localization of EEG electrodes. Front. Neurosci. *9*.

Rizzo, V., Siebner, H.R., Modugno, N., Pesenti, A., Münchau, A., Gerschlager, W., Webb, R.M., and Rothwell, J.C. (2004). Shaping the excitability of human motor cortex with premotor rTMS. J. Physiol. *554*, 483–495.

Rogasch, N.C., Thomson, R.H., Daskalakis, Z.J., and Fitzgerald, P.B. (2013). Short-Latency Artifacts Associated with Concurrent TMS–EEG. Brain Stimulat. *6*, 868–876.

Rogasch, N.C., Thomson, R.H., Farzan, F., Fitzgibbon, B.M., Bailey, N.W., Hernandez-Pavon, J.C., Daskalakis, Z.J., and Fitzgerald, P.B. (2014). Removing artefacts from TMS-EEG recordings using independent component analysis: Importance for assessing prefrontal and motor cortex network properties. NeuroImage *101*, 425–439.

Rogasch, N.C., Daskalakis, Z.J., and Fitzgerald, P.B. (2015). Cortical inhibition of distinct mechanisms in the dorsolateral prefrontal cortex is related to working memory performance: A TMS–EEG study. Cortex *64*, 68–77.

Rogasch, N.C., Sullivan, C., Thomson, R.H., Rose, N.S., Bailey, N.W., Fitzgerald, P.B., Farzan, F., and Hernandez-Pavon, J.C. (2016). Analysing concurrent transcranial magnetic stimulation and electroencephalographic data: A review and introduction to the open-source TESA software. NeuroImage.

Romei, V., Rihs, T., Brodbeck, V., and Thut, G. (2008a). Resting electroencephalogram alpha-power over posterior sites indexes baseline visual cortex excitability. Neuroreport *19*, 203–208.

Romei, V., Brodbeck, V., Michel, C., Amedi, A., Pascual-Leone, A., and Thut, G. (2008b). Spontaneous Fluctuations in Posterior α-Band EEG Activity Reflect Variability in Excitability of Human Visual Areas. Cereb. Cortex *18*, 2010–2018.

Rossi, S., Hallett, M., Rossini, P.M., and Pascual-Leone, A. (2009). Safety, ethical considerations, and application guidelines for the use of transcranial magnetic stimulation in clinical practice and research. Clin. Neurophysiol. *120*, 2008–2039.

Rossini, P.M., Burke, D., Chen, R., Cohen, L.G., Daskalakis, Z., Di Iorio, R., Di Lazzaro, V., Ferreri, F., Fitzgerald, P.B., George, M.S., et al. (2015). Non-invasive electrical and magnetic stimulation of the brain, spinal cord, roots and peripheral nerves: Basic principles and procedures for routine clinical and research application. An updated report from an I.F.C.N. Committee. Clin. Neurophysiol. *126*, 1071–1107.

Roth, M., Decety, J., Raybaudi, M., Massarelli, R., Delon-Martin, C., Segebarth, C., Morand, S., Gemignani, A., Décorps, M., and Jeannerod, M. (1996). Possible involvement of primary motor

cortex in mentally simulated movement: a functional magnetic resonance imaging study. Neuroreport *7*, 1280–1284.

Roth, Y., Levkovitz, Y., Pell, G.S., Ankry, M., and Zangen, A. (2014). Safety and Characterization of a Novel Multi-channel TMS Stimulator. Brain Stimulat. *7*, 194–205.

Ruohonen, D.J., and Ilmoniemi, R.J. (1998). Focusing and targeting of magnetic brain stimulation using multiple coils. Med. Biol. Eng. Comput. *36*, 297–301.

Ruohonen, J., Ravazzani, P., Grandori, F., and Ilmoniemi, R.J. (1999). Theory of multichannel magnetic stimulation: toward functional neuromuscular rehabilitation. IEEE Trans. Biomed. Eng. *46*, 646–651.

Rushworth, M.F., Ellison, A., and Walsh, V. (2001). Complementary localization and lateralization of orienting and motor attention. Nat. Neurosci. *4*, 656–661.

Russell, G.S., Jeffrey Eriksen, K., Poolman, P., Luu, P., and Tucker, D.M. (2005). Geodesic photogrammetry for localizing sensor positions in dense-array EEG. Clin. Neurophysiol. *116*, 1130–1140.

Saari, J., Kallioniemi, E., Tarvainen, M., and Julkunen, P. (2017). Oscillatory TMS-EEG-responses as a Measure of the Cortical Excitability Threshold. IEEE Trans. Neural Syst. Rehabil. Eng. *PP*, 1–1.

Sauseng, P., Klimesch, W., Gerloff, C., and Hummel, F.C. (2009). Spontaneous locally restricted EEG alpha activity determines cortical excitability in the motor cortex. Neuropsychologia *47*, 284–288.

Schalk, G., McFarland, D.J., Hinterberger, T., Birbaumer, N., and Wolpaw, J.R. (2004). BCI2000: a general-purpose brain-computer interface (BCI) system. IEEE Trans. Biomed. Eng. *51*, 1034–1043.

Schilberg, L., Schuhmann, T., and Sack, A.T. (2017). Interindividual Variability and Intraindividual Reliability of Intermittent Theta Burst Stimulation-induced Neuroplasticity Mechanisms in the Healthy Brain. J. Cogn. Neurosci. 1–11.

Schulz, H., Übelacker, T., Keil, J., Müller, N., and Weisz, N. (2014). Now I am Ready—Now I am not: The Influence of Pre-TMS Oscillations and Corticomuscular Coherence on Motor-Evoked Potentials. Cereb. Cortex *24*, 1708–1719.

Sharma, N., and Baron, J.-C. (2013). Does motor imagery share neural networks with executed movement: a multivariate fMRI analysis. Front. Hum. Neurosci. *7*.

Shepard, D. (1968). A Two-dimensional Interpolation Function for Irregularly-spaced Data. In Proceedings of the 1968 23rd ACM National Conference, (New York, NY, USA: ACM), pp. 517–524.

Siebner, H.R., Bergmann, T.O., Bestmann, S., Massimini, M., Johansen-Berg, H., Mochizuki, H., Bohning, D.E., Boorman, E.D., Groppa, S., Miniussi, C., et al. (2009). Consensus paper: Combining transcranial stimulation with neuroimaging. Brain Stimulat. *2*, 58–80.

Silvanto, J., and Pascual-Leone, A. (2008). State-Dependency of Transcranial Magnetic Stimulation. Brain Topogr. *21*, 1–10.

Silvanto, J., Muggleton, N.G., Cowey, A., and Walsh, V. (2007). Neural adaptation reveals state-dependent effects of transcranial magnetic stimulation. Eur. J. Neurosci. *25*, 1874–1881.

Silvoni, S., and Ramos-Murguialday, A. (2011). Brain-computer interface in stroke: a review of progress. Clin. EEG ….

Smith, S.M. (2002). Fast robust automated brain extraction. Hum. Brain Mapp. *17*, 143–155.

Soekadar, S.R., Birbaumer, N., Slutzky, M.W., and Cohen, L.G. (2015). Brain–machine interfaces in neurorehabilitation of stroke. Neurobiol. Dis. *83*, 172–179.

Sohrabpour, A., Lu, Y., Worrell, G., and He, B. (2016). Imaging brain source extent from EEG/MEG by means of an iteratively reweighted edge sparsity minimization (IRES) strategy. NeuroImage *142*, 27–42.

Sollmann, N., Hauck, T., Obermüller, T., Hapfelmeier, A., Meyer, B., Ringel, F., and Krieg, S.M. (2013). Inter- and intraobserver variability in motor mapping of the hotspot for the abductor policis brevis muscle. BMC Neurosci. *14*, 94.

Sommer, M., Wu, T., Tergau, F., and Paulus, W. (2002). Intra- and interindividual variability of motor responses to repetitive transcranial magnetic stimulation. Clin. Neurophysiol. *113*, 265–269.

Suppa, A., Bologna, M., Gilio, F., Lorenzano, C., Rothwell, J.C., and Berardelli, A. (2008). Preconditioning Repetitive Transcranial Magnetic Stimulation of Premotor Cortex Can Reduce But Not Enhance Short-Term Facilitation of Primary Motor Cortex. J. Neurophysiol. *99*, 564–570.

Szameitat, A.J., Shen, S., and Sterr, A. (2007). Motor imagery of complex everyday movements. An fMRI study. NeuroImage *34*, 702–713.

Tadel, F., Baillet, S., Mosher, J.C., Pantazis, D., and Leahy, R.M. (2011). Brainstorm: A User-Friendly Application for MEG/EEG Analysis. Comput. Intell. Neurosci. *2011*.

Taylor, D.M. (2002). Direct Cortical Control of 3D Neuroprosthetic Devices. Science *296*, 1829–1832.

Thielscher, A., and Kammer, T. (2002). Linking Physics with Physiology in TMS: A Sphere Field Model to Determine the Cortical Stimulation Site in TMS. NeuroImage *17*, 1117–1130.

Thielscher, A., and Kammer, T. (2004). Electric field properties of two commercial figure-8 coils in TMS: calculation of focality and efficiency. Clin. Neurophysiol. *115*, 1697–1708.

Thielscher, A., Opitz, A., and Windhoff, M. (2011). Impact of the gyral geometry on the electric field induced by transcranial magnetic stimulation. NeuroImage *54*, 234–243.

Tiitinen, H., Virtanen, J., Ilmoniemi, R.J., Kamppuri, J., Ollikainen, M., Ruohonen, J., and Näätänen, R. (1999). Separation of contamination caused by coil clicks from responses elicited by transcranial magnetic stimulation. Clin. Neurophysiol. *110*, 982–985.

Tomassini, V., Jbabdi, S., Klein, J.C., Behrens, T.E.J., Pozzilli, C., Matthews, P.M., Rushworth, M.F.S., and Johansen-Berg, H. (2007). Diffusion-Weighted Imaging Tractography-Based Parcellation of the Human Lateral Premotor Cortex Identifies Dorsal and Ventral Subregions with Anatomical and Functional Specializations. J. Neurosci. *27*, 10259–10269.

Touge, T., Gerschlager, W., Brown, P., and Rothwell, J.C. (2001). Are the after-effects of low-frequency rTMS on motor cortex excitability due to changes in the efficacy of cortical synapses? Clin. Neurophysiol. *112*, 2138–2145.

Towle, V.L., Bolaños, J., Suarez, D., Tan, K., Grzeszczuk, R., Levin, D.N., Cakmur, R., Frank, S.A., and Spire, J.-P. (1993). The spatial location of EEG electrodes: locating the best-fitting sphere relative to cortical anatomy. Electroencephalogr. Clin. Neurophysiol. *86*, 1–6.

Ueno, S., Tashiro, T., and Harada, K. (1988). Localized stimulation of neural tissues in the brain by means of a paired configuration of time-varying magnetic fields. J. Appl. Phys. *64*, 5862–5864.

Uithol, S., Franca, M., Heimann, K., Marzoli, D., Capotosto, P., Tommasi, L., and Gallese, V. (2015). Single-pulse Transcranial Magnetic Stimulation Reveals Contribution of Premotor Cortex to Object Shape Recognition. Brain Stimulat. *8*, 953–956.

Vallence, A.-M., Goldsworthy, M.R., Hodyl, N.A., Semmler, J.G., Pitcher, J.B., and Ridding, M.C. (2015). Inter- and intra-subject variability of motor cortex plasticity following continuous theta-burst stimulation. Neuroscience *304*, 266–278.

Van Doren, J., Langguth, B., and Schecklmann, M. (2015). TMS-related potentials and artifacts in combined TMS-EEG measurements: Comparison of three different TMS devices. Neurophysiol. Clin. Neurophysiol. *45*, 159–166.

Vansteensel, M.J., Pels, E.G.M., Bleichner, M.G., Branco, M.P., Denison, T., Freudenburg, Z.V., Gosselaar, P., Leinders, S., Ottens, T.H., Van Den Boom, M.A., et al. (2016). Fully Implanted Brain–Computer Interface in a Locked-In Patient with ALS. N. Engl. J. Med. *375*, 2060–2066.

Vasilyev, A., Liburkina, S., Yakovlev, L., Perepelkina, O., and Kaplan, A. (2017). Assessing motor imagery in brain-computer interface training: Psychological and neurophysiological correlates. Neuropsychologia *97*, 56–65.

Veniero, D., Bortoletto, M., and Miniussi, C. (2009). TMS-EEG co-registration: On TMS-induced artifact. Clin. Neurophysiol. *120*, 1392–1399.

Veniero, D., Maioli, C., and Miniussi, C. (2010). Potentiation of Short-Latency Cortical Responses by High-Frequency Repetitive Transcranial Magnetic Stimulation. J. Neurophysiol. *104*, 1578–1588.

Veniero, D., Bortoletto, M., and Miniussi, C. (2013). Cortical modulation of short-latency TMS-evoked potentials. Front. Hum. Neurosci. *6*.

Vernet, M., Bashir, S., Yoo, W.-K., Perez, J.M., Najib, U., and Pascual-Leone, A. (2013). Insights on the neural basis of motor plasticity induced by theta burst stimulation from TMS–EEG. Eur. J. Neurosci. *37*, 598–606.

Vernet, M., Bashir, S., Yoo, W.-K., Oberman, L., Mizrahi, I., Ifert-Miller, F., Beck, C.J., and Pascual-Leone, A. (2014). Reproducibility of the effects of theta burst stimulation on motor cortical plasticity in healthy participants. Clin. Neurophysiol. *125*, 320–326.

Vidaurre, C., and Blankertz, B. (2010). Towards a Cure for BCI Illiteracy. Brain Topogr. *23*, 194–198.

Wagner, T.A., Zahn, M., Grodzinsky, A.J., and Pascual-Leone, A. (2004). Three-dimensional head model Simulation of transcranial magnetic stimulation. IEEE Trans Biomed Eng *51*, 1586–1598.

Wang, W., Collinger, J.L., Degenhart, A.D., Tyler-Kabara, E.C., Schwartz, A.B., Moran, D.W., Weber, D.J., Wodlinger, B., Vinjamuri, R.K., Ashmore, R.C., et al. (2013). An Electrocorticographic Brain Interface in an Individual with Tetraplegia. PLoS ONE *8*, e55344.

Wassermann, E.M. (1998). Risk and safety of repetitive transcranial magnetic stimulation: report and suggested guidelines from the International Workshop on the Safety of Repetitive Transcranial Magnetic Stimulation, June 5–7, 1996. Electroencephalogr. Clin. Neurophysiol. Potentials Sect. *108*, 1–16.

Weigand, A., Horn, A., Caballero, R., Cooke, D., Stern, A.P., Taylor, S.F., Press, D., Pascual-Leone, A., and Fox, M.D. (2017). Prospective Validation That Subgenual Connectivity Predicts Antidepressant Efficacy of Transcranial Magnetic Stimulation Sites. Biol. Psychiatry.

Werf, Y.D.V.D., and Paus, T. (2006). The neural response to transcranial magnetic stimulation of the human motor cortex. I. Intracortical and cortico-cortical contributions. Exp. Brain Res. *175*, 231–245.

Williams, J., Pearce, A.J., Loporto, M., Morris, T., and Holmes, P.S. (2012). The relationship between corticospinal excitability during motor imagery and motor imagery ability. Behav. Brain Res. *226*, 369–375.

Windhoff, M., Opitz, A., and Thielscher, A. (2013). Electric field calculations in brain stimulation based on finite elements: an optimized processing pipeline for the generation and usage of accurate individual head models. Hum. Brain Mapp. *34*, 923–935.

Wolpaw, J.R., and McFarland, D.J. (2004). Control of a two-dimensional movement signal by a noninvasive brain-computer interface in humans. Proc. Natl. Acad. Sci. U. S. A. *101*, 17849–17854.

Wolpaw, J.R., McFarland, D.J., Neat, G.W., and Forneris, C.A. (1991). An EEG-based brain-computer interface for cursor control. Electroencephalogr. Clin. Neurophysiol. *78*, 252–259.

Wolpaw, J.R., Birbaumer, N., McFarland, D.J., Pfurtscheller, G., and Vaughan, T.M. (2002). Brain–computer interfaces for communication and control. Clin. Neurophysiol. *113*, 767–791.

Xu, R., Jiang, N., Lin, C., Mrachacz-Kersting, N., Dremstrup, K., and Farina, D. (2014). Enhanced Low-Latency Detection of Motor Intention From EEG for Closed-Loop Brain-Computer Interface Applications. IEEE Trans. Biomed. Eng. *61*, 288–296.

Yuan, H., and He, B. (2014). Brain-Computer Interfaces Using Sensorimotor Rhythms: Current State and Future Perspectives. IEEE Trans. Biomed. Eng. *61*, 1425–1435.

Yuan, H., Liu, T., Szarkowski, R., Rios, C., Ashe, J., and He, B. (2010). Negative covariation between task-related responses in alpha/beta-band activity and BOLD in human sensorimotor cortex: An EEG and fMRI study of motor imagery and movements. NeuroImage *49*, 2596–2606.

Zrenner, C., Belardinelli, P., Müller-Dahlhaus, F., and Ziemann, U. (2016). Closed-Loop Neuroscience and Non-Invasive Brain Stimulation: A Tale of Two Loops. Front. Cell. Neurosci. *10*.

Zrenner, C., Desideri, D., Belardinelli, P., and Ziemann, U. (2018). Real-time EEG-defined excitability states determine efficacy of TMS-induced plasticity in human motor cortex. Brain Stimulat. *11*, 374–389.

(2018). openvr: OpenVR SDK (Valve Software).

6 Appendix 1: Subject-specific optimization of channel currents for multichannel transcranial magnetic stimulation

Abstract

The goal of this work is to develop a focal transcranial magnetic stimulation (TMS) system using a multichannel coil array for high-resolution neuromodulation. We proposed a novel spatially-distributed stimulation strategy to significantly improve the focality of TMS. Computer simulations were conducted to evaluate the proposed approach and test the merits of multichannel TMS. Three different multichannel coil arrays were modeled in addition to a conventional figure-8 coil for comparison. Simulations were performed on finite element head models of six subjects constructed from anatomical MR images via an automated pipeline. Multichannel TMS arrays exhibited significantly more focal induced electric field magnitudes compared to the figure-8 coil. Additionally, electrical steering of stimulation sites without physical movement of the coil array was demonstrated.

6.1 Introduction

Transcranial magnetic stimulation (TMS) is a form of neuromodulation that can noninvasively stimulate regions of the brain. Large transient currents driven through one or more loops of wire induce transient magnetic fields; these magnetic fields penetrate through the skull and other tissue relatively unimpeded, and induce transient currents in the brain. Initial TMS development began in the 1980s using a single circular coil to induce large loops of current in the brain (Barker et al., 1985). Within several years the field progressed to using a figure-8 coil,

in which counter-rotating currents in a pair of coils induce more focal electric fields (Ueno et al., 1988). Since the development of this figure-8 coil, many alternative coil designs have been proposed, but few demonstrate significant improvements over the figure-8 (Deng et al., 2013), and have thus not yet reached widespread use. The majority of these designs propose complex coil geometries, but still rely on a single channel stimulator to supply current. However, there is great potential for improvement in the form of multichannel TMS (mTMS), in which multiple coils are driven by independent stimulator channels.

With a multichannel stimulator, currents in individual stimulation coils can be selected to control each coil's influence on the induced electric field produced by an entire coil array. This weighting of channels enables two primary benefits of mTMS: stimulation focality can be improved by partial cancellation of opposing fields, and the site of stimulation can be electrically steered without physical movement of the coil array (Ruohonen and Ilmoniemi, 1998). This approach requires calculation of channel currents, or “weights”, to achieve a desired induced electric field. This optimization is typically accomplished through minimization of a cost function involving coil currents and desired field profiles (e.g. (Han et al., 2004; Ruohonen and Ilmoniemi, 1998; Ruohonen et al., 1999).

Due to the significant influence of individuals' cortical geometry and cerebrospinal fluid (CSF) distribution on the fields induced by TMS (Thielscher et al., 2011), calculation of optimal channel weights for mTMS is highly dependent on individual head geometry. This work demonstrates automated subject-specific optimization of coil currents for mTMS using a variety of possible coil configurations.

6.2 Methods

Anatomical T1 MRI scans (1 mm isotropic) were acquired from six human subjects (three male). Each subject provided written consent prior to participating in an imaging protocol approved by the University of Minnesota Institutional Review Board. Subject-specific finite element meshes were constructed from this MRI data using the SimNIBS pipeline (Windhoff et al., 2013), which integrates several of the tools described below. Surface meshes at the boundaries between white matter (WM), gray matter (GM), CSF, skull, scalp, and air were segmented with FreeSurfer (Dale et al., 1999; Fischl, 2012; Fischl et al., 1999) and the FSL Brain Extraction Tool (BET) (Jenkinson et al., 2005; Smith, 2002). Meshes were manipulated with MeshFix (Attene, 2010) and other tools within SimNIBS. Finite element method (FEM) modeling was performed with GetFEM++ in MATLAB, as described in (Windhoff et al., 2013). Postprocessing, data analysis, and visualization were accomplished with Iso2Mesh (Fang and Boas, 2009) and custom scripts in MATLAB.

Head models were segmented into five tissue types, with a constant isotropic conductivity value from (Wagner et al., 2004) assigned to each: $\sigma_{\mathrm{WM}} = 0.126$ S/m, $\sigma_{\mathrm{GM}} = 0.276$ S/m, $\sigma_{\mathrm{CSF}} = 1.654$ S/m, $\sigma_{\mathrm{skull}} = 0.010$ S/m, $\sigma_{\mathrm{scalp}} = 0.465$ S/m.

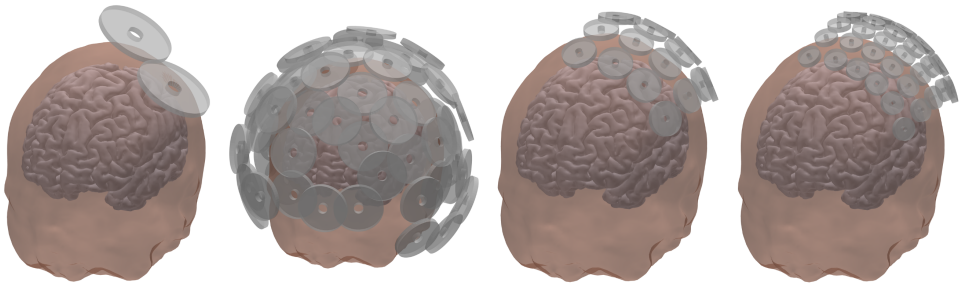

Figure 6.1: Coil arrays used in simulations. *From left to right: figure-8 coil, 64-channel whole head array, 16-channel local array, and 32-channel local array. Representative subject's scalp and gray matter surfaces shown for reference.*

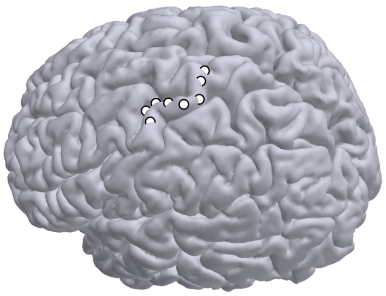

Figure 6.2: Stimulation targets in one subject.

Individual coils were modeled as point clouds of magnetic dipoles, as described in (Thielscher and Kammer, 2002, 2004). Fields were modeled at a single peak value of dI/dt, without simulating the full temporal characteristics of the TMS pulse and assuming that all stimulation channels were in phase. Field strengths presented here are scaled by the maximum field strength in each solution.

6.2.1 Multichannel Optimization

For a given coil array orientation, the induced electric field in the tissue was solved independently for each channel. Total induced electric field for the whole array was then calculated by weighted superposition of separate E_x, E_y, and E_z components of electric field of all channels at every point in the mesh. Mutual coupling between coils was assumed to be negligible for these simulations.

Coil weights were determined by minimizing the cost function given in Equation (17), where at each node n, E_d is the desired electric field magnitude, $\vec{E}_c$ is the unweighted electric field contribution from each coil c, and w_c is the weight for each coil.

$$\underset{w_c}{\operatorname{argmin}} \sum_{n \in \mathrm{GM}} \left(E_d(n) - \left\| \sum_c w_c \vec{E}_c(n) \right\| \right)^2 \tag{17}$$

For the multichannel array simulations, the desired electric field E_d was set to 1 at all nodes within a fixed radius (5 mm) of a target on the GM surface, and 0 everywhere else. Coil weight optimization was performed only on the GM surface for efficiency, though it is also feasible to minimize a cost function over the full head volume.

6.2.2 Simulation experiments

Four coil types were compared across eight stimulation targets in each of six subjects. The coil types are depicted in Figure 6.1.

The figure-8 coil model was based on a standard Magstim 70 mm diameter coil, as described in (Windhoff et al., 2013). The coil was oriented perpendicular to a line passing through a target on the GM surface and the approximate center of the brain, centered over the target, with distance calculated such that the coil windings were positioned 5 mm from the outer scalp surface. The figure-8 coil was rotated approximately 45° from the midline, per common practice for motor cortex stimulation.

The 64-channel whole-head array consisted of 64 circular coils 50 mm in diameter. The coils were oriented over selected positions on the 10-10 electrode coordinate system of a reference brain, and overlapped in two layers without any intersections. This overlapping arrangement was chosen to allow relatively large diameter coils, which are preferable for reducing mechanical strain from Lorenz forces and improving heat capacity, to be assembled into a dense array. Coils were not adjusted to match the 10-10 positions of individual subjects.

The 16-channel local array consisted of a curved 4×4 grid of non-overlapping circular coils 30 mm in diameter. It was positioned such that the array center was approximately over the hand knob of the left motor cortex, and remained in the same fixed position for simulations of all

targets. The 36-channel local array consisted of a curved 6×6 grid of non-overlapping circular coils 20 mm in diameter. It was positioned in the same way as the 16-channel array.

For each subject dataset, eight targets were selected along what was approximated as the left primary motor cortex based on anatomical features. See Figure 6.2 for an example. The targets were selected on one brain, and then mapped to the other datasets via FreeSurfer's normalized pial surfaces. Minor manual adjustments to these targets were made in each subject to keep the targets along outermost gyral contours, as this study did not aim to examine deeper brain stimulation.

Electric field distributions on the GM surface were compared for each simulation. Array performance was quantified by examining the GM surface area where induced electric field exceeded a threshold of 50% of the maximum value.

6.3 Results

Simulations indicate that the multichannel arrays produce more focal induced electric field magnitudes on the GM surface than the figure-8 coil. Figure 6.3 shows the electric fields induced by the four coil types for one target on one subject. The field produced by the figure-8 coil is visibly more diffuse, while the 36-channel array produces the most focal of field distributions.

These results generalize across multiple subjects. Figure 6.4 displays examples of optimized stimulation with the 16-channel array at one target across all six subjects. The large variation in induced electric field across subjects illustrates the significant role of subject-specific cortical geometry in shaping the induced fields, but the consistent focality of stimulation demonstrates that the multichannel arrays can account for this variation. Overall results are summarized in Figure 6.5, which shows in the top row that the surface area of supra-threshold electric field

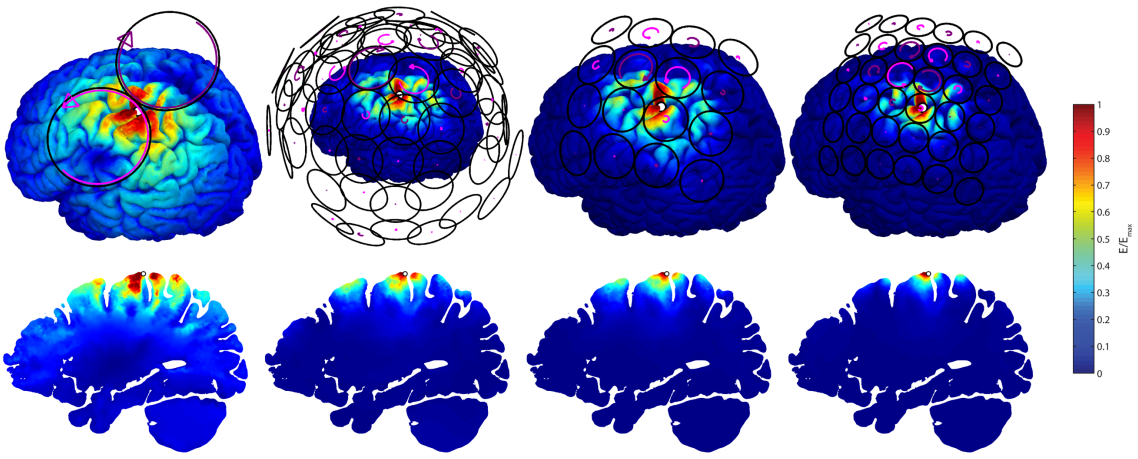

Figure 6.3: Simulation results for the four coil types in one subject. *Top row shows plots of electric field magnitude on GM surface. Bottom row shows plots of electric field magnitude in a parasagittal slice of GM and WM through the target. Radius of arrows is proportional to channel weight, color of arrows indicates clockwise (dark purple) or counterclockwise (light purple) current flow. White circle indicates target location on cortex*

magnitude on the cortex outside of the target region is notably higher for the figure-8 coil than for the multichannel arrays. These figures demonstrate that this improvement in focality holds across subjects and across the selected target locations.

As shown in the parasagittal slices in the bottom row of Figure 6.3, the electric field induced by the figure-8 penetrates deeper into the brain than the fields of the multichannel arrays. It should be noted with regard to this penetration depth that the multichannel weights were only optimized for stimulation on the cortex, and that deeper multichannel stimulation could potentially be achieved by modifying the channel weighting cost function in (17).

The choice of threshold at 50% of the maximum electric field magnitude is arbitrary. Figure 6.6 shows surface areas above threshold outside the target region for a broad range of thresholds, for which the multichannel arrays are consistently more focal.

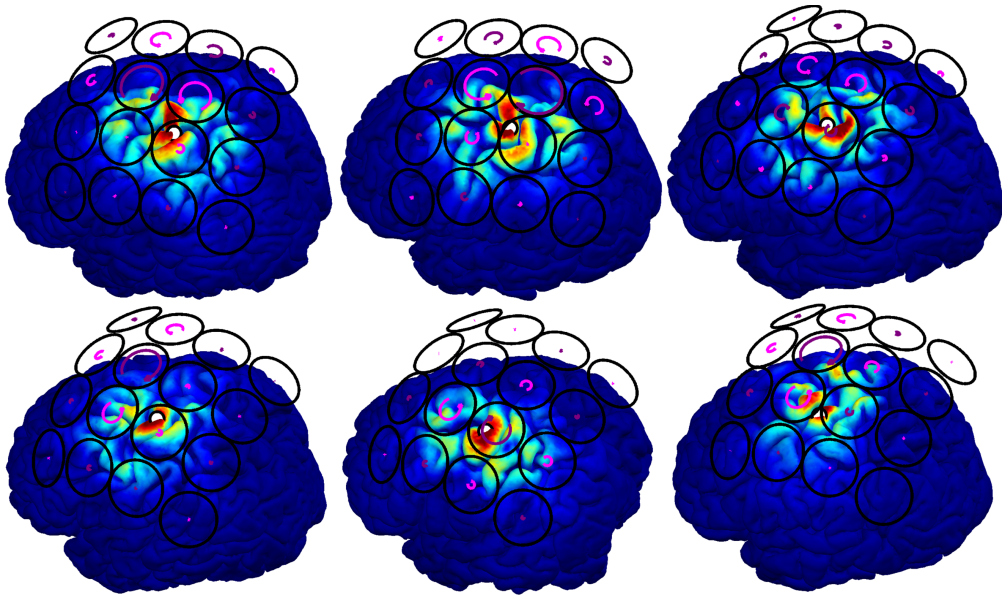

Figure 6.4: 16-channel array simulation results. *Electric field magnitude induced for all six subjects at one target.*

6.4 Discussion and conclusion

We present the first direct comparison between a conventional figure-8 coil and mTMS coil arrays. The high level of pipeline automation implemented here allowed for analysis of a larger number of subjects than presented in past mTMS work, and may make it feasible to apply this subject-specific modeling approach to guide actual stimulation experiments in the future.

Our simulation results indicate that the multichannel arrays can exhibit superior focality over the figure-8. This improved focality has the potential to improve the specificity of TMS for brain mapping and therapeutic applications. Additionally, the simulations presented here have demonstrated the ability of mTMS to "steer" the site of stimulation while keeping the array fixed with respect to the head. This steering of current could be useful for rapid sequential-pulse paradigms such as paired-pulse TMS, where stimulation is delivered to multiple cortical sites in rapid succession. Conventional TMS hardware is limited to one or at most two stimulation sites

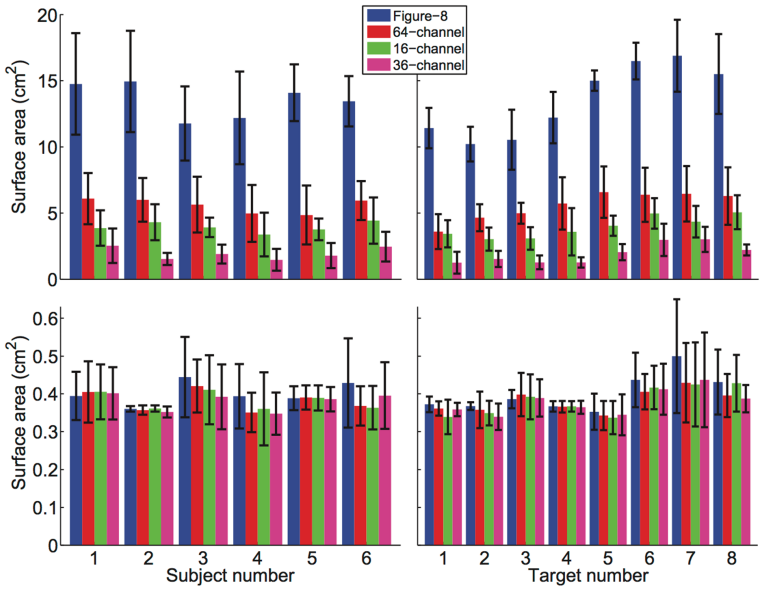

Figure 6.5: Quantification of focality across subjects. *Mean surface area of GM above threshold outside (top) and inside (bottom) of target stimulation region, averaged across targets (left) and across subjects (right). Error bars indicate standard deviation.*

per hemisphere, but a multichannel array would reasonably be able to target a much larger number of sites.

Despite these benefits, there are several key factors that limit mTMS. As the number of channels increase, so too do hardware complexity and power requirements (Ruohonen and Ilmoniemi, 1998). The cost of stimulator units will likely need to decrease before high-channel count stimulators will be accessible to a large audience. As an intermediate solution, a small multi-channel stimulator could drive a subset of a larger coil array to still benefit from improved focality and stimulation steering without extreme hardware complexity.

The last issue is constraints on coil size. Although the 36-channel array of 20 mm coils was shown to have superior focality, this size of coil may not be feasible in practice. The increased current needed to stimulate with a smaller coil, increased mechanical strain from Lorenz forces, and reduced heat capacity from reduced overall mass combine to make smaller coils

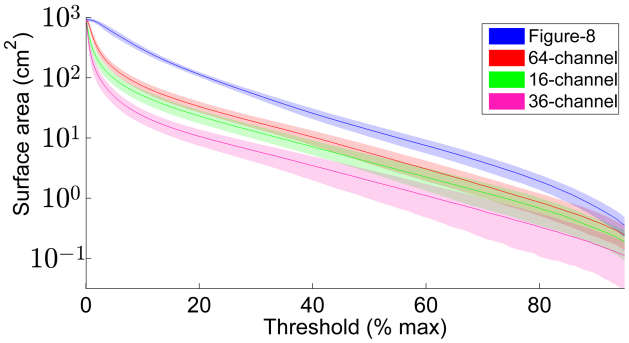

Figure 6.6: Surface area of GM above threshold outside of target stimulation as a function of threshold. *Averaged across all subjects and targets. Extents of shaded curves indicate standard deviation.*

impractical. This was the motivation for simulating the 64-channel whole-head array with slightly overlapping 50 mm coils; this coil diameter is already commonly used in figure-8 designs, and would have fewer issues with heating and mechanical strain compared to smaller coils.

There are many future directions for research related to mTMS. The simulations presented here could be extended with more advanced optimization cost functions to target deeper brain regions or to minimize stimulation in specific regions. Currently this optimization is based on induced electric field magnitude; however, this field strength does not necessarily directly correlate to modulation of neuronal activity. Individual neuron models could be incorporated into the optimization procedure to more accurately predict the effects of stimulation. The present optimization procedure relies heavily on subject-specific finite-element models to predict induced electric fields in the brain. These models could be improved by incorporation of more accurate anatomical information, such as anisotropic tissue conductivities. Modeling of the coupling between coils and full temporal characteristics of the stimulator circuits would also improve relevance.

The described approach can model any array geometry, and future work is warranted to determine what configurations might improve upon the rectangular grid and arbitrary 64-channel arrays presented here. Finally, these modeling predictions need to be validated using actual multichannel stimulator hardware in an experimental setting. TMS hardware that supports a small number of independent channels is just starting to become available (Roth et al., 2014), and increased channel counts in the future should open up a broader range of mTMS applications.

7 Appendix 2: EEG electrode digitization with commercial virtual reality hardware

This is adapted from a manuscript currently in review as: Cline, C.C., Coogan, C., and He, B. EEG electrode digitization with commercial virtual reality hardware. PLOS ONE. In review.

Abstract

Accurate spatial co-registration of EEG electrode positions with individual head models is an important component for EEG source localization and imaging. Due to variations in head shape between individuals, this requires measurements of electrode locations in each individual. Existing hardware for digitization can be accurate, but also relatively expensive. With the goal of making digitization more accessible for a range of research laboratories, we have developed an open-source software tool that can make use of less expensive consumer virtual reality hardware for EEG electrode digitization. Here we describe our developed VRDigitizer system and compare it to existing digitization solutions. Experimental evaluations were performed in a phantom head model and in 12 human subjects. In our comparison experiments, VRDigitizer was able to measure electrode positions with a mean error of 3.74 mm, compared to 1.73 mm and 2.98 mm for the commercial systems tested.

7.1 Introduction

Electroencephalography (EEG) uses electrodes on the scalp to noninvasively record electrical signals generated by the brain and conducted through the cerebrospinal fluid, skull, and scalp (He et al., 2011). This process of volume conduction effectively blurs the EEG signals measured on the scalp, limiting the spatial resolution of these signals. Patterns of EEG activity observed on the scalp can be highly dependent on the cortical geometry of the underlying sources, and therefore analysis of EEG sensor activity is challenging with regard to its origins within the brain.

In order to improve the spatial resolution of EEG, source imaging and localization approaches have been developed for estimating the underlying cortical source activity responsible for signals observed on the scalp, essentially projecting these signals back onto the brain (Edelman et al., 2016; He et al., 1987; Mahjoory et al., 2017; Michel et al., 2004; Pascual-Marqui et al., 1994; Sohrabpour et al., 2016). A critical component of these approaches is the construction of a volume conduction model, which relates signals produced on the cortical surface to those measured by specific EEG electrodes on the scalp. Especially when using subject-specific head models for source imaging, it is critical to have an accurate estimate of where each EEG electrode was located on the subject's head (Dalal et al., 2014). While standard EEG montages are widely used and allow approximate estimates of electrode locations, there can be large variability in head shape and cap placement across individuals and sessions. Therefore, it is preferable to actually measure the physical locations of the EEG electrode on individual subjects in order to build more accurate models for source imaging.

Various methods are available for digitizing, or measuring the 3D locations, of EEG electrodes on the head (De Munck et al., 1991; He and Estepp, 2013; Koessler et al., 2007, 2011; Le et al., 1998; Reis and Lochmann, 2015; Russell et al., 2005; Towle et al., 1993). Hardware digitization solutions involve some method of 3D spatial measurements, such as pointing a tracked stylus at each electrode or photogrammetry-based methods that use images taken from multiple angles to reconstruct electrode location (Russell et al., 2005). However, the cost of such digitization hardware has typically been on the order of $10,000, making these methods expensive for EEG research and broader applications.

In recent years, several consumer-oriented room-scale virtual reality (VR) systems have been introduced to the market. These systems, such as the HTC Vive, use 6 degree-of-freedom (DOF)

tracking of a head-mounted display (HMD) and associated peripherals to provide immersive virtual reality experiences. Marketed for individual consumers, these systems currently cost less than $1000. Conveniently, the 6DOF tracking of VR controllers can be used for the same purpose as more specialized hardware digitization solutions for EEG electrode localization, at a significantly lower price.

The primary goal of this work was to develop an open-source software package to facilitate digitization of EEG electrodes with cost-effective consumer VR hardware. We also aimed to characterize the typical digitization performance of such a system, and to compare it to other existing digitization systems.

7.2 Methods

7.2.1 Hardware

The HTC Vive system includes a head mounted display (HMD), two tracked controllers, and two beacon devices called Lighthouses. These Lighthouses emit alternating horizontal and vertical sweeps of infrared light using a laser diode, in addition to interleaved synchronization flashes from an array of infrared LEDs. Multiple photodiodes on each tracked device (e.g. a controller) measure the relative perceived times of these infrared sweeps, allowing for 6DOF pose estimation. Multiple Lighthouses can be used in tandem to enhance localization accuracy and provide redundancy in case of optical occlusion. The lighthouses can communicate via optical or cabled synchronization depending on the required room setting. Each tracked device also has a 6DOF inertial measurement unit (IMU) to sense acceleration and rotational velocity, allowing for higher-temporal resolution relative pose tracking. Sensor fusion algorithms integrated into the Vive system merge the optical Lighthouse and IMU data together to calculate pose estimates

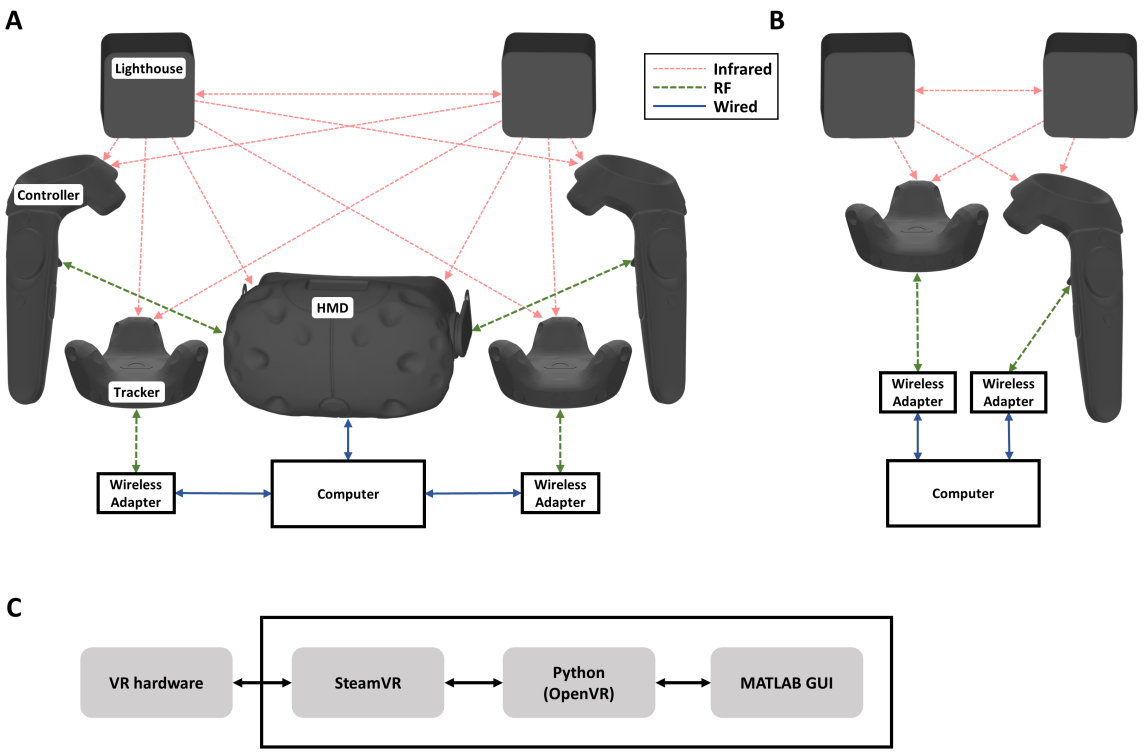

Figure 7.1: Diagrams of connections between hardware and software components of the VR digitizer system. *(A) Complete Vive hardware setup, with two controllers each communicating with the computer through the HMD, two trackers connected via independent wireless adapters, and all tracked devices receiving signals from two Lighthouses. (B) Reduced Vive hardware setup, with a single tracker and controller communicating through wireless adapters without an HMD. (C) Connections between software components.*

that are passed on to the client software. In addition to the controllers, other tracked devices called “Vive Trackers” are available which include essentially the same tracking hardware without controls in a more compact form factor. The HMD is typically tethered to a computer, and up to two tracked devices can be paired to communicate wirelessly through the HMD, with additional devices using a wireless adapter that pairs the device to the computer (Figure 7.1A). Although the Vive system is primarily designed to be used with the HMD, individual controllers and trackers can be used without an HMD by pairing solely through wireless adapters and configuring the OpenVR software to use a simulated “null” HMD (Figure 7.1B).

7.2.2 Software

A custom helper program written in Python leverages PyOpenVR (Bruns, 2017) to obtain tracking data from the VR hardware. PyOpenVR consists of bindings to the open-source OpenVR API (2018), which provides a standardized interface for communicating with various VR systems from multiple vendors. The Python helper acquires tracking data for each device, in the form of a rigid spatial transformation matrix that encodes position and orientation in a common coordinate system. These spatial transforms are transmitted along with additional information (e.g. controller button states) via TCP to MATLAB.

The primary functions for the VR digitizer software are implemented in MATLAB, with the Python component described above mainly serving to relay raw device state data. The key components of the MATLAB GUI are described here. The custom software and system implemented are referred to as “VRDigitizer” below.

Each measurement consists of the 3D position of a reference endpoint on the controller. With the Python component constantly streaming live tracking data to MATLAB, pressing a button on the controller triggers a sample. In the simplest case, a sample position could be obtained from the single most recent tracking state. However, the raw Vive tracking data is optimized for gaming performance, not for accurate digitization; specifically, there is some high frequency jitter in the tracking data, and some low frequency drift that persists for up to several seconds after the end of controller movement. To reduce the effect of high frequency jitter, the tracking data over a window of time (e.g. 0.5 sec) are averaged. To deal with the low frequency drift, measurements are required to be stable (defined as being within an empirical threshold, such as 1 mm) over a window of time (e.g. 0.5 sec). With each triggered sample, optional audio and

haptic cues indicate to the user whether or not a measurement was deemed valid. The exact filter settings (window lengths, stability threshold) are user-configurable to allow selecting for a tradeoff between accuracy and speed of digitization.

The Vive Lighthouses emit reference signals used by all tracked devices for estimating pose in a common 3D space. While some tracking can be achieved with just one Lighthouse, accuracy is improved if each tracked device can "see" both Lighthouses at the time of measurement. This can be ensured by proper room setup and tracker positioning. Since pose estimates with only one Lighthouse tend to be less stable over time, the stability threshold described above helps to prevent low-precision measurements from being recorded while a tracked device's view of one Lighthouse is occluded.

Electrode positions are typically defined relative to anatomical landmarks on the head, such as the nasion and preauricular points. These landmarks facilitate coregistration of electrode positions with MRI data and anatomical head models. VRDigitizer allows specification of arbitrary fiducial points. Fiducials can be measured repeatedly to improve accuracy by averaging and to verify consistency across repeated measurements.

When digitizing electrode positions, it is useful to have a predefined electrode montage specifying the electrode names and channel numbers for a given experimental setup. These montages can vary depending on the EEG cap vendor or other custom experimental requirements. VRDigitizer allows importing of many standard montage file formats, including optional specification of template electrode positions for visualization of "expected" electrode locations. During digitization, VRDigitizer provides optional audio cues through text-to-speech to indicate the next measurement to be made, e.g. speaking the name of the current electrode,

and most functions can be carried out by pressing buttons on the controller; these features facilitate more efficient interaction with the GUI, allowing the operator to stay near the subject and reducing overall time for digitization.

Electrode positions can be visualized relative to arbitrary surface meshes, such as scalp or cortical surfaces segmented from MRI data. If a subject-specific head model is available, this can aid with visualization of electrode locations during measurement. VRDigitizer supports import of several common mesh formats (.stl, .fsmesh, .off, etc.). In the absence of a subject-specific head surface, an atlas head surface can be used by default.

During digitization, the controller is moved in 3D space to the location of a point to measure. For precise measurements, a single "endpoint" on the controller needs to be defined; this facilitates proper compensation for controller rotation around the endpoint. VRDigitizer allows specification of an arbitrary endpoint relative to the controller; to define this endpoint, a simple calibration routine is used. The user enters a calibration mode in the software, and records several measurements across a range of controller rotations, keeping the intended endpoint fixed in space.

The calibration measurements are processed as follows. The i^{th} sample from the PyOpenVR is structured as a 4×4 rigid spatial transform $\boldsymbol{T}_i$ that converts from controller-relative space to a global space. Defining a point $\vec{x}_0 = [0\ 0\ 0\ 1]$ as the origin of the controller, $\boldsymbol{T}_i\vec{x}_0$ gives the location of the center of the controller in global space. The goal of calibration is to find $\vec{x}_c$ in the device-relative space that defines the offset of the intended endpoint relative to the $\vec{x}_0$. The global position $\vec{x}_g$ of the endpoint for the i^{th} measurement can then be calculated from $\boldsymbol{T}_i(\vec{x}_0 + \vec{x}_c)$. Given a set of N spatial transforms $\{T_i\}$, each from a measurement with a

different controller orientation around the shared fixed endpoint, $\vec{x}_c$ can be obtained through numerical optimization. Specifically, the optimization problem can be expressed as:

$$\underset{\vec{x}_c}{\operatorname{argmin}} \sum_{i=1}^{N} \left| \underbrace{\boldsymbol{T}_i(\vec{x}_0 + \vec{x}_c)}_{\vec{x}_{gi}} - \frac{1}{N} \sum_{j=1}^{N} \underbrace{\boldsymbol{T}_j(\vec{x}_0 + \vec{x}_c)}_{\vec{x}_{gj}} \right|_2 \tag{18}$$

The solution to this expression is the $\vec{x}_c$ that minimizes the spread of $\{\vec{x}_g\}$ derived from the calibration measurements. Metrics of calibration quality can be obtained from terms of this cost function, such as the maximum deviation from the mean:

$$\max_{i \in N} \left| \vec{x}_{gi} - \frac{1}{N} \sum_{j=1}^{N} \vec{x}_{gj} \right|_2 \tag{19}$$

VRDigitizer solves Equation (18) using constrained nonlinear optimization as implemented by 'fmincon' in MATLAB. The results of calibration are shown by VRDigitizer with a depiction of the estimated endpoint position relative to the controller and a visualization of individual calibration measurements; an example of this is shown in Figure 7.2.

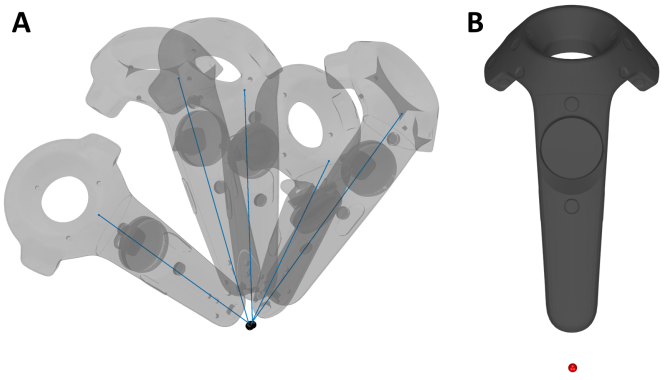

Figure 7.2: Example of endpoint calibration. *(A) Visualization of calibration process, showing five samples measured with varied rotations about the selected endpoint. Black spheres indicate the estimated endpoint location for each sample, and blue lines connect the estimated endpoint to the controller origin. (B) Final endpoint location relative to controller. The endpoint (red sphere) is offset from controller since it was defined as a point at the end of a micro USB cable stub not included in the controller 3D model.*

During electrode digitization, the subject's head may move over time. If there is no compensation for this change in position, error is introduced between the measurements before and after a given movement. One solution to this is to attempt to fix the subject's head during digitization measurements, thus minimizing movement. However, this may not be feasible for many experimental setups based on subject comfort and other factors. The solution more commonly used by EEG digitization systems is to simultaneously track head position in addition to the measurement stylus. VRDigitizer can perform this head tracking using standalone tracked devices fixed to the subject's head. While the HMD is designed for head tracking and is bundled with the core Vive hardware, its straps are likely to block many electrodes and the faceplate itself blocks the nasion, an anatomical landmark typically measured during digitization. Instead, VRDigitizer can use standalone Vive Trackers, smaller devices with tracking hardware similar to the controller but without buttons, to measure head movement. When enabled, VRDigitizer measures the controller endpoint relative to one or more trackers, allowing compensation for head movement in real-time.

Many EEG digitization systems use a single additional tracking device for head movement compensation. However, if this head tracker moves relative to the head during measurement, additional error can be introduced. With only a single tracker on the head, this problem may go undetected during measurement. VRDigitizer allows the use of multiple head trackers; if one tracker moves on the head, the mismatch in trackers can be detected and a warning can notify the user to realign the trackers or remeasure fiducials with the new tracker positions.

In addition to digitization of anatomical fiducials and electrodes, arbitrary points on the head surface can also be sampled. These points may be used to assist with MRI coregistration or atlas warping during post-processing

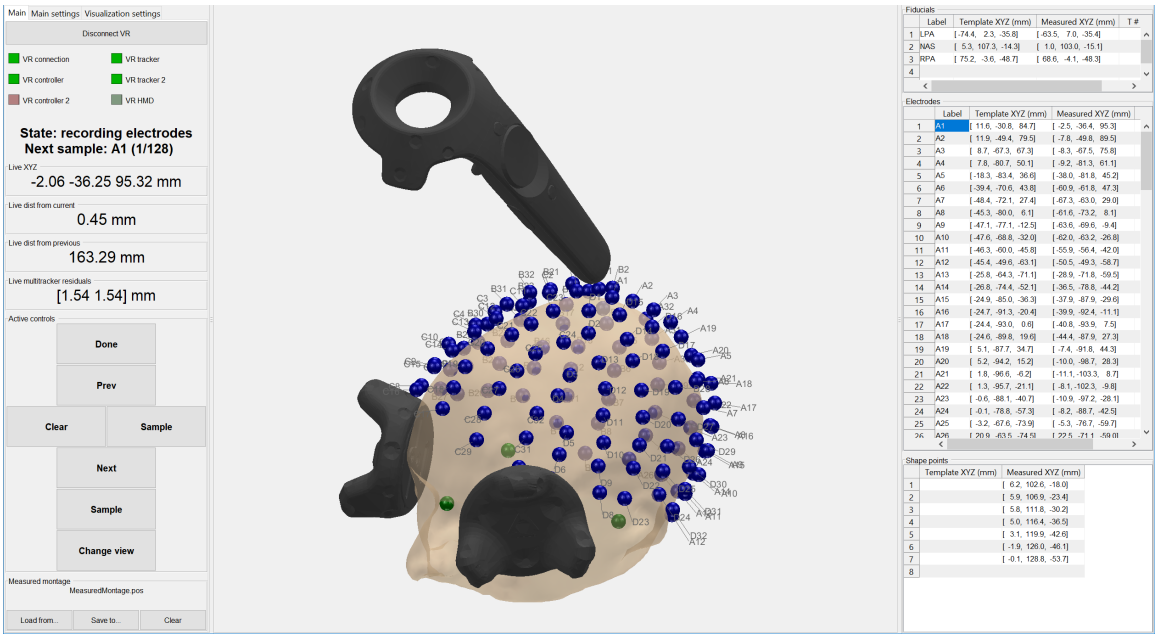

Figure 7.3: Screenshot of main VRDigitizer GUI window.

VRDigitizer can provide real-time visualization of various components, including the head surface, template montage, measured fiducials, measured electrodes, and endpoint, controller, and tracker positions. This is illustrated in Figure 7.3, which shows an example screenshot from the main VRDigitizer GUI window.

7.2.3 Experimental evaluation

To characterize the expected accuracy of the VRDigitizer setup and compare it to other digitization methods, two sets of experiments were performed. The first set involved a "phantom" styrofoam head, while the second involved 12 human subjects who provided written informed consent under a protocol approved by the University of Minnesota Institutional Review Board. In both series of experiments, BioSemi 128 channel caps with a radial montage were used.

In addition to VRDigitizer, two other systems were utilized for calibration accuracy comparison. The first was a Brainsight neuronavigation system (Rogue Research), which uses a Polaris Vicra stereo infrared camera to track infrared reflective spheres fixed on rigid frames for monitoring the pose of a stylus relative to glasses on the subject's head. The second system was a Polhemus FASTRAK utilizing the open-source Brainstorm software (Tadel et al., 2011); this system uses electromagnetic tracking with a fixed wired RF transmitter and two wired 6DOF tracked receivers, one in a stylus and another on the subject's head.

Two different variations of VRDigitizer setups were used: digitization with no trackers (i.e. no compensation for head movement), and with two head trackers. In the no tracker condition, the phantom head was secured to a rigid support, and human subjects used a chinrest and forehead support attached to a table to minimize head movement; no HMD was connected, instead a single wireless adapter was used to connect to the controller. In the two-tracker condition, Vive trackers were secured with a Velcro strap to either side of the forehead (as illustrated in Figure 7.3); the controller and both trackers were connected via the HMD and a single wireless adapter.

Vive Lighthouses were attached to the wall in diagonally opposite corners of the room (4.25 m apart, 2.6 m above the floor), and were synchronized optically. A stub of a microUSB cable was inserted into the base of the controller to provide a precise digitization endpoint; this location of the endpoint at the base of the controller (as shown in Figure 7.2) also helped to ensure the photodiode sensors at the top of the controller maintained a view of both Lighthouses during digitization.

The VRDigitizer calibration interface was used to calibrate the endpoint position relative to the center of the controller. Approximately 10 measurements were sampled with the controller rotated into different orientations around the selected endpoint, which was held at a fixed point in space throughout calibration.

With each subject or phantom iteration, 5 whole-head digitizations were performed, consisting of VRDigitizer without trackers ("NoTrackers"), VRdigitizer with two trackers ("TwoTrackers"), Polhemus with Brainstorm ("Brainstorm"), and two Brainsight repetitions. The VRDigitizer NoTrackers condition included head restraint, while the other conditions did not. Subjects donned the cap once and kept the cap in place throughout the 5 digitizations, for a total duration of about 50-60 minutes.

For each digitization dataset collected with each system, several steps were performed. Head trackers (as applicable) were fixed to the head. Anatomical fiducials were digitized first; with the same nasion and left and right preauricular points measured with each system. Next, electrodes were digitized, always proceeding in order from BioSemi electrodes A1,A2,... to D32. Finally, each fiducial was re-measured twice as a head shape point.

7.2.4 Analysis

To quantify localization accuracy, digitization errors were calculated using one Brainsight dataset in each subject (or phantom repetition) as the reference or "ground truth". Each dataset was aligned to the reference by estimating and applying a single rigid spatial transformation that best aligned paired sets of points across the datasets (Besl and McKay, 1992). These alignment points were either the anatomical fiducials only (i.e. aligning by fiducials) or the measured electrode locations (i.e. aligning by electrodes). The former case is representative of common

use of EEG digitization data in practice, in which as a first stage of co-registration with MRI the digitized points are aligned by the corresponding anatomical fiducial locations in the MRI. However, in this case of aligning by fiducials, inconsistency in a single fiducial location can propagate and appear as error in localization across all electrodes on the head. Therefore, the second case of aligning by electrodes was used to provide an estimate of electrode localization accuracy independent of anatomical fiducial measurements. After alignment, localization error was quantified as the Euclidean distance between each electrode and its corresponding reference location. Statistical comparisons were calculated using Student's t-test with Bonferroni correction for multiple comparisons.

7.3 Results

Example digitization results using VRDigitizer with two trackers for a single subject are shown in Figure 7.4. Aligned to the reference Brainsight digitization dataset by electrodes, the RMS localization error here was 3.95 mm, and the maximum error was 8.41 mm. For comparison,

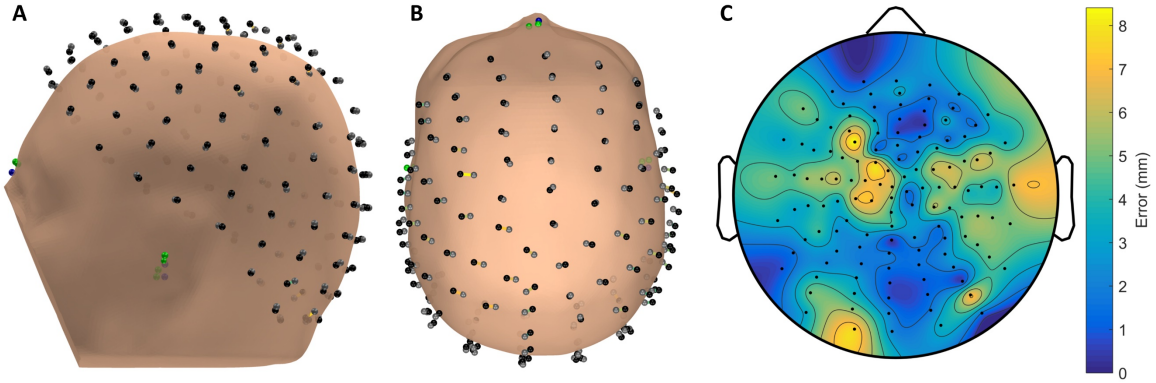

Figure 7.4: VRDigitizer localization results for a single subject (S06). *In (A) and (B), the green and gray circles indicate fiducials and electrodes measured for the VRDigitizer TwoTrackers condition, while the blue and black circles indicate fiducials and electrodes measured for the Brainsight reference condition; the colors of the lines connecting corresponding electrodes across the two datasets are indicative of the magnitude of localization error. Interpolated localization error is plotted with the same color scale on a projected 2D scalp topography in (C). Here, the two datasets were aligned by electrodes, and the subject's scalp surface was aligned by the reference dataset anatomical fiducials. Electrodes appear offset from the scalp surface due to the selected digitization point for each electrode being on the top surface of the 3-mm thick electrode mount.*

most neighboring electrodes in the BioSemi 128 radial montage used here had interelectrode distances of between 18-25 mm for this subject.

Figure 7.5 shows localization errors for multiple digitizations of the phantom head. Aggregating errors within each dataset by the root mean square error (RMSE), mean ± standard deviation RMSE values when aligning by electrodes were 1.12 ± 0.15 mm for Brainsight, 1.60 ± 0.15 mm for Brainstorm, and 2.30 ± 0.16 mm for VRDigitizer with two trackers. Brainsight demonstrated significantly lower errors than the other systems ($p_c < 5 \cdot 10^{-4}$). Brainstorm demonstrated significantly lower errors than both VRDigitizer conditions when aligning by electrodes but not when aligning by fiducials.

Similar trends were observed for localization errors with human subjects, with results shown in Figure 7.6. Aligning by electrodes, mean ± standard deviation RMSE values were 1.73 ± 0.37 mm for Brainsight, 2.98 ± 0.89 mm for Brainstorm, and 3.74 ± 0.71 mm for VRDigitizer with two trackers. The differences in mean RMSEs between Brainstorm and the VRDigitizer conditions were not significant except for a marginally significant difference with the no tracker aligned by electrodes condition ($p_c = 0.028$).

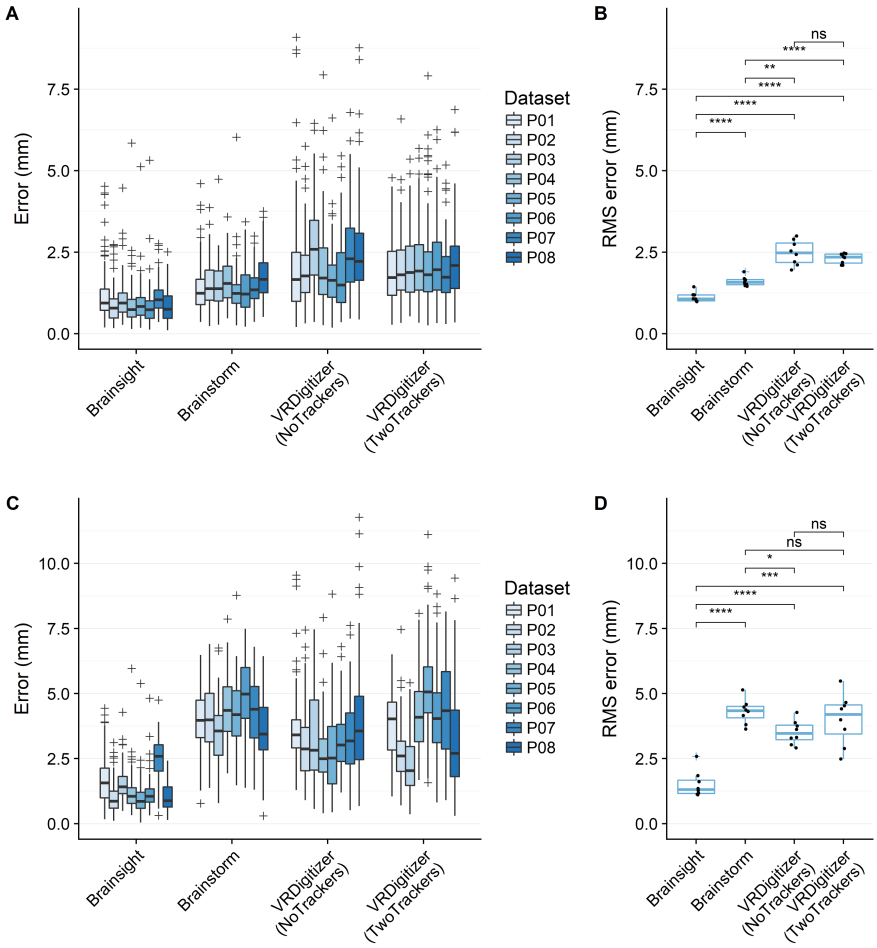

Figure 7.5: Localization errors for phantom measurements. *Aligned by electrodes (A,B) or by fiducials (C,D). (A) and (C) show individual results, with each box-and-whisker corresponding to a single dataset and each point corresponding to localization error for a single electrode. (B) and (D) show grouped results, with each point corresponding to a scalar RMSE error aggregated from a single dataset. Asterisks indicate statistically significant differences according to Student's t tests with correction for multiple comparisons (**** $p_c < 0.0001$, *** $p_c < 0.001$, ** $p_c < 0.01$, * $p_c < 0.05$, ns not significant).*

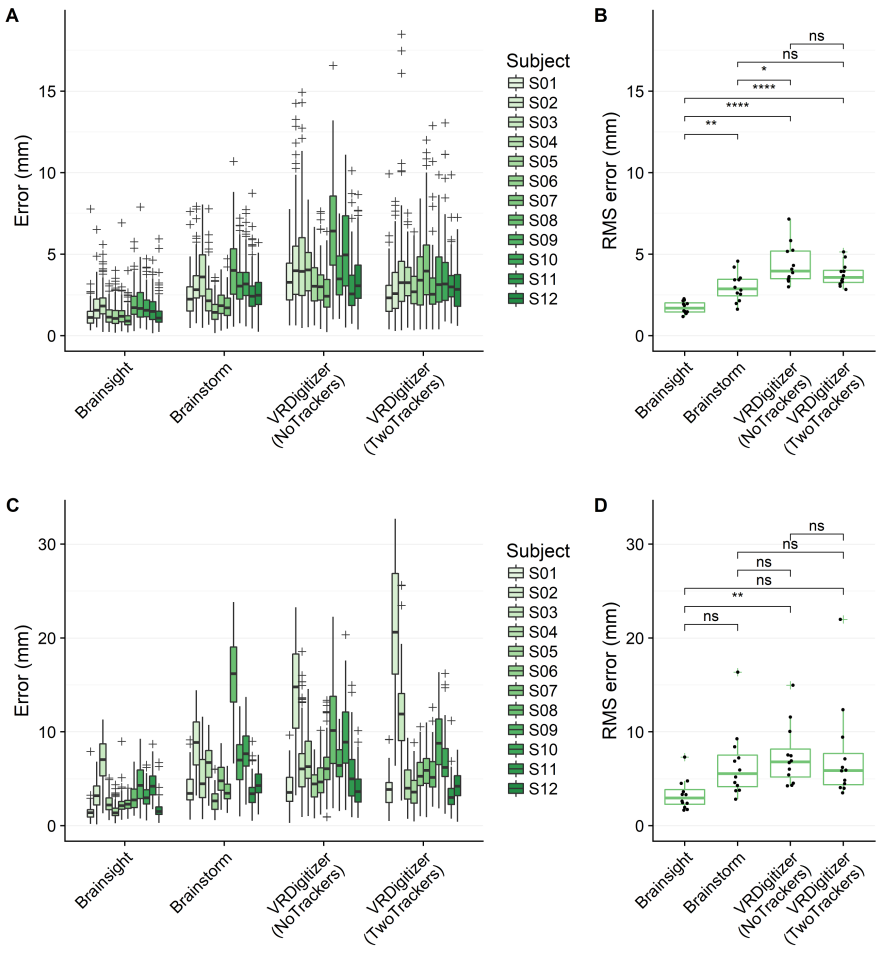

Figure 7.6: Localization errors for subject measurements. *Aligned by electrodes (A,B) or by fiducials (C,D). (A) and (C) show individual results, with each box-and-whisker corresponding to a single dataset and each point corresponding to localization error for a single electrode. (B) and (D) show grouped results, with each point corresponding to a scalar RMSE error aggregated from a single dataset. Asterisks indicate statistically significant differences according to Student's t tests with correction for multiple comparisons (**** $p_c < 0.0001$, *** $p_c < 0.001$, ** $p_c < 0.01$, * $p_c < 0.05$, ns not significant).*

7.4 Discussion

We have developed a new digitizer system, allowing digitization of EEG electrode positions in 3D space using widely-available consumer virtual reality hardware. The accuracy of VRDigitizer is comparable to existing digitization systems, with a typical RMS localization error of less than 5 mm.

Critically, the digitization system described here uses commercial virtual reality hardware available for $500-$800 at current prices; the software is free and open-source. Other systems for digitization of EEG electrodes can cost 10-20 times this amount, limiting the number of EEG research projects able to include digitization of electrode positions.

Despite cost benefits, the described VRDigitizer system did not match the accuracy of the Brainsight/Polaris and Brainstorm/Polhemus systems tested here. Each of the three systems use different tracking methods. Brainsight uses an infrared stereo camera with fixed geometry passive reflective trackers; this can be very precise but prone to problems with optical occlusion between the single mounted camera and the reflective trackers. Brainstorm uses an electromagnetic transmitter and receivers which do not require line of sight; however, this system can be subject to geometric distortion in the presence of nearby metal objects (see supplementary Figure 7.7). VRDigitizer with the Vive estimates tracked device pose by measuring the relative timing of signals emitted from the shared Lighthouse beacons, combined with IMU data; the Vive also can have issues with optical occlusion and reduced precision.

For the results presented here, the electrode positions measured by the Brainsight system were used as the “ground truth” or reference for comparing localization accuracies. The relatively low RMS errors observed between repeated Brainsight measurements support the assumption that

this system provides a suitable reference with which to compare the various digitization systems. However, it is possible that some consistent bias or geometric distortion was present in these repeated measurements; effects of such consistent error, if any, were minimized during phantom measurements by moving the head relative to the Brainsight/Polaris camera and repositioning the head tracking glasses between repeated sets of measurements. Nevertheless, more absolute measurements of digitization accuracy could be obtained in the future by using a phantom with precise, rigidly defined points (e.g. as used in (Russell et al., 2005)).

Each system tested here still requires the operator to "point" a stylus at each electrode during digitization; the amount of time required for this process can discourage the use of digitization in some cases. Other recently introduced systems using photogrammetry (Russell et al., 2005) or 3D scanners (Koessler et al., 2011) hold promise for faster and more automatic electrode digitization with comparable accuracy. These approaches, while promising, also require hardware that is currently more expensive than the VRDigitizer approach described here.

Another possible method for reducing time needed for digitization with stylus-based systems is to only digitize a representative subset of electrodes (He and Estepp, 2013). While not yet implemented here, the open-source VRDigitizer software can be freely modified, and such improvements can therefore be integrated into the software in the future.

Overall, the availability of cost-effective hardware and open source software for digitization of EEG electrode positions should benefit the EEG community, facilitating analysis of EEG signals in source space using inverse source imaging methods, with more relevant subject-specific head models and electrode positions. Such approaches are necessary to move beyond single channel analyses and scalp topographies for more robust individual and group-level EEG source imaging.

7.5 Supporting information

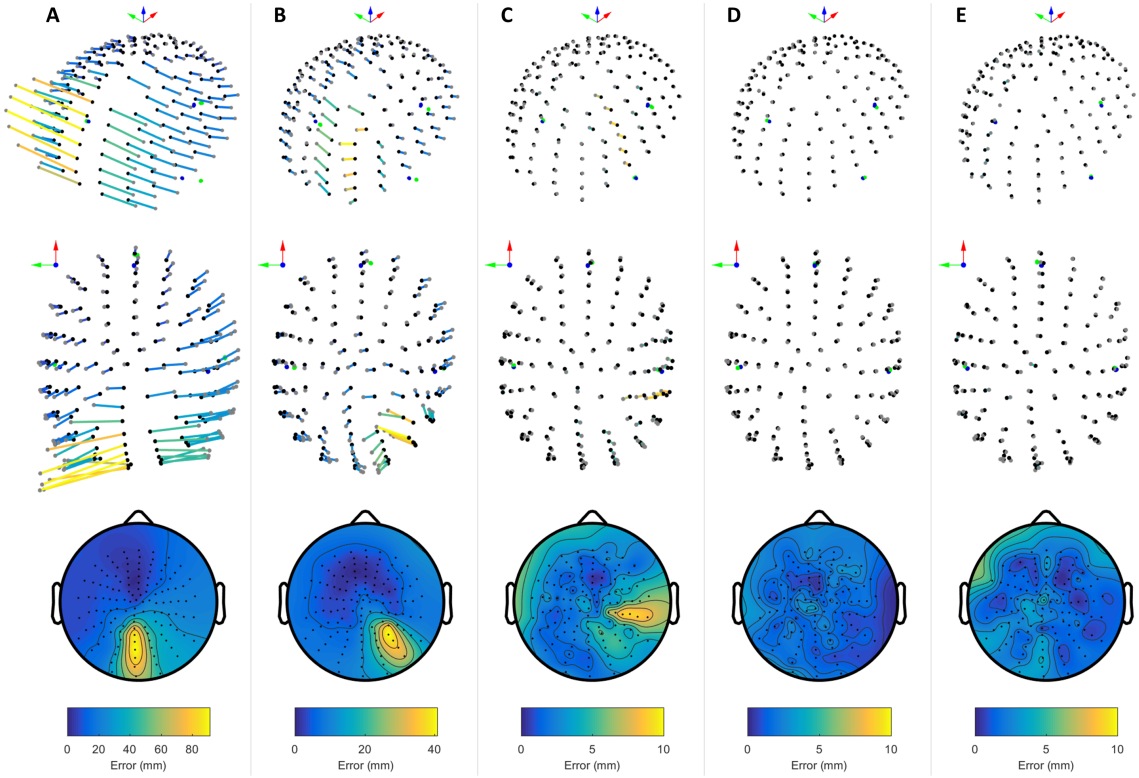

Figure 7.7: Example of distortion in Brainstorm/Polhemus measurements caused by nearby metal. *A 40 mm x 40 mm x 300 mm piece of extruded aluminum was placed oriented vertically near the phantom head to demonstrate the effects of the presence of metal on Polhemus digitizer measurements. The RF transmitter was approximately 22 cm from the center of the head along the horizontal plane, and approximately 10 cm below the lowest electrode. (A) shows the results of digitizing with the aluminum piece placed between the RF transmitter and the of the head, about 7 cm from the center of the head. (B) and (C) show the results of digitizing after moving the aluminum piece 10 cm and 20 cm to the right (perpendicular to the line between the RF transmitter and the center of the head), respectively. (D) shows the results of digitizing without any metal nearby with the Polhemus system. (E) shows example results of digitizing with the VRDigitizer two tracker setup. In the upper and middle plots, the green and gray circles indicate fiducials and electrodes measured by the Polhemus digitizer (A-D) or VRDigitizer (E), while the blue and black circles indicate fiducials and electrodes measured for the Brainsight reference condition; the colors of the lines connecting corresponding electrodes across the two datasets are indicative of the magnitude of localization error. Interpolated localization error is plotted with the same color scale on a projected 2D scalp topography in the lower plots.*